INL/EXT-17-40821

Assessment of Impact of Monoenergetic Photon Sources on Prioritized Nonproliferation Applications

Cameron Geddes, Bernhard Ludewigt,
John Valentine, Brian Quiter,
Marie-Anne Descalle, Glen Warren,
Matt Kinlaw, Scott Thompson,
David Chichester, Cameron Miller,
Sara Pozzi

January 2017

The INL is a U.S. Department of Energy National Laboratory
operated by Battelle Energy Alliance

INL/EXT-17-40821

Assessment of Impact of Monoenergetic Photon Sources on Prioritized Nonproliferation Applications

Cameron Geddes, Bernhard Ludewigt, John Valentine, Brian Quiter, Marie-Anne Descalle, Glen Warren, Matt Kinlaw, Scott Thompson, David Chichester, Cameron Miller, Sara Pozzi

January 2017

Idaho National Laboratory
Idaho Falls, Idaho 83415

http://www.inl.gov

Prepared for the
U.S. Department of Energy
Assistant Secretary for ____, OR Office of _____
Under DOE Idaho Operations Office
Contract DE-AC07-05ID14517

Assessment of Impact of Monoenergetic Photon Sources on Prioritized Nonproliferation Applications

Simulation Study Report

December 30, 2016

Project Team

Cameron Geddes (PI), Lawrence Berkeley National Laboratory
Bernhard Ludewigt (Co-PI), Lawrence Berkeley National Laboratory
John Valentine, Lawrence Berkeley National Laboratory
Brian Quiter, Lawrence Berkeley National Laboratory
Marie-Anne Descalle, Lawrence Livermore National Laboratory
Glen Warren, Pacific Northwest National Laboratory
Matt Kinlaw, Idaho National Laboratory
Scott Thompson, Idaho National Laboratory
David Chichester, Idaho National Laboratory
Cameron Miller, University of Michigan
Sara Pozzi, University of Michigan

Prepared by:
Lawrence Berkeley National Laboratory

Prepared for:
DOE NNSA, DNN R&D Enabling Capabilities
Program Manager: James Peltz

Project Number: LB15-V-LB-Monoenergetic Photons-PD3UE

INL/EXT-17-40821

Executive Summary

Near-monoenergetic photon sources (MPSs) have the potential to improve sensitivity at greatly reduced dose in existing applications and to enable new capabilities in other applications, particularly where passive signatures do not penetrate or are insufficiently accurate. MPS advantages include the ability to select energy, energy spread, flux, and pulse structures to deliver only the photons needed for the application, while suppressing extraneous dose and background. Some MPSs also offer narrow angular divergence photon beams which can target dose and/or mitigate scattering contributions to image contrast degradation. Current bremsstrahlung photon sources (e.g., linacs and betatrons) produce photons over a broad range of energies, thus delivering unnecessary dose that in some cases also interferes with the signature to be detected and/or restricts operations. Current sources must be collimated (reducing flux) to generate narrow divergence beams. While MPSs can in principle resolve these issues, they remain at relatively low TRL status. Candidate MPS technologies for nonproliferation applications are now being developed, each of which has different properties (e.g. broad angular divergence vs. narrow). Within each technology, source parameters trade off against one another (e.g. flux vs. energy spread), representing a large operation space. To guide development, requirements for each application of interest must be defined and simulations conducted to define MPS parameters that deliver benefit relative to current systems.

The present project conducted a broad assessment of potential nonproliferation applications where MPSs may provide new capabilities or significant performance enhancement (initial assessment report [1]), which led to prioritization of several applications for detailed analysis. The prioritized applications were: cargo screening and interdiction of Special Nuclear Materials (SNM), detection of hidden SNM, treaty/dismantlement verification, and spent fuel dry storage cask content verification. High resolution imaging for stockpile stewardship was considered as a sub-area of the treaty topic, as it is also of interest for future treaty use. This report presents higher-fidelity calculations and modeling results to quantitatively evaluate the prioritized applications, and to derive the key MPS properties that drive application benefit. Simulations focused on the conventional signatures of radiography, photofission, and Nuclear Resonance Fluorescence (NRF) to enable comparison to present methods and evaluation of benefit. A separate Final Report integrates all conducted assessments and photon source development needs.

Screening and Interdiction of Shielded SNM

Screening for and interdiction of SNM, typically in cargo containers, train cars and trucks, is a priority application for the Department of Homeland Security, as well as other agencies (e.g., the Department of Energy Nuclear Smuggling Detection and Deterrence program - formerly Second Line of Defense). Access to both sides of the object is typically available, which facilitates use of radiography as a primary screening method, including use of dual energy transmission ratios to resolve target Z. Photofission and Nuclear Resonance Fluorescence are considered as secondary screening methods to clear alarms (i.e. to resolve whether or not an object is SNM).

Significant potential benefit was indicated for the configurations analyzed for radiography applications using monoenergetic photon beams. Replacing bremsstrahlung with a monoenergetic source having similar emission angle and pulse structure enables reductions in radiography dose by factors of 3-4x. MPSs with narrow angular divergence (e.g. Thomson sources) can deliver small beam diameter at the target without severe collimation that would throw away almost all of the flux. Narrow divergence beams, at the few mrad level to deliver cm-size spots on target, nearly eliminate image contrast degradation due to scattering. Scattering is severe for many cargo cases, and mitigation can either increase image quality or provide a significant added reduction in dose. Dose reduction due to mitigation of scattering is in the range of 3-4x even compared to very narrowly

collimated fan bremsstrahlung systems (and a much greater advantage vs. broadly collimated sources). To achieve high image quality in the presence of scattering, narrow divergence was more important than control of energy spectrum. This indicates that MPSs with narrower angle emission than bremsstrahlung fans will provide strongest advantage (and correspondingly, that MPSs with broader emission angles than bremsstrahlung systems may not be advantageous in cases where scattering is significant). Narrow divergence also enables pencil beam scanning, with the advantages of spot by spot dose modulation. Since most of a cargo is typically low density, with isolated high-density areas (e.g. an engine or machine part), such dose adaptation strongly reduces dose to all but suspect regions. Narrow energy spread on the other hand is critical to using dual energy transmission ratios to identify regions containing different Zs. Contrast is drastically increased by using a monoenergetic source, by factors of a few to ten in the examples examined (depending on configuration). This could enable effective discrimination in cases that are not currently accessible. Overall reduction in dose to stowaway and in scatter dose to surroundings and exclusion zone could be an order of magnitude or greater, depending on cargo and system design. MPSs for radiography should produce photons at selected energies from 3-9 MeV, and with typical fluxes on target (after collimation, determined by scan rate and penetration needs) in the range of 10^{10} photons per second for initial capabilities to 10^{12} photons per second for high performance applications. Pulsed sources should have repetition rates in the kHz range to enable initial scanning capabilities, while repetition rates in the 10-50 kHz range would enable high performance.

A key advantage of MPSs for clearing an alarm or detecting SNM in cargo screening is the capability to induce a much stronger photofission signal for a given dose than other sources. For example, for a 9 MeV MPS the dose to cargo and surroundings per fission induced in 2 kg of HEU behind 20 cm steel is more than 50x lower than for a 9 MeV bremsstrahlung source due to a combination of reduced beam attenuation in the steel and higher photofission rates. Narrow divergence MPSs (e.g. Thomson sources) are particularly well suited for resolving an alarm caused by an object in an identified location because the low-divergence beam can deliver a high photon flux to that area. Identification of 2 kg HEU behind 30 cm of shielding in seconds is realistic using an MPS with ≤10 mrad divergence operating at 1 kHz and delivering 10^8 photons/shot on target (after collimation) at 9 MeV with 10% energy spread. NRF is enabled at energy spreads of 2% and repetition rates of 10 kHz, which are realistic goals for Thomson sources and would make it possible to detect 2 kg HEU inside 10 cm thick steel shielding in 10s of seconds. Future Thomson sources with an energy spread of a fraction of a percent may become available that would greatly increase capability. In general, NRF is more suitable where composition analysis is needed, either for contraband detection or isotopics on SNM.

Cargo screening is an application where MPSs could have high impact. Benefits for radiography combine the effects of monoenergetic transmission, up to ten-fold increased Z contrast, scattering mitigation, and dose adaptation. Such a source could enable superior resolution combined with typical dose reductions of one to two orders of magnitude depending on cargo configuration and MPS emission angle. Alarm resolution using photofission and NRF is enabled with up to orders of magnitude lower doses and with increased performance.

Detection of Hidden SNM

Detecting hidden SNM was considered separately from screening to address scenarios where access to the object/container of interest is limited to one side (at most, 180°). These scenarios are of interest to DNDO for parked vehicles, to emergency response, and potentially to the Defense Threat Reduction Agency. A constrained inspection volume is assumed to have been pre-defined (e.g., a vehicle of interest at distances of up to ~25 m). Larger distances or objects (i.e. standoff, broad area scans) were excluded based on preliminary calculations. Photofission is an appropriate

method for one-sided access. For clearing an object, sufficient information about the amount of shielding surrounding the nuclear material must be available to firmly conclude that a lack of observed fission signatures is not due to shielding but proves the absence of SNM.

MPSs can significantly reduce doses to the object for photofission by delivering all of the photons in the range of high fission cross section. The strongest photofission signal is obtained near the photofission resonance energy of ~15 MeV. The imparted doses are approximately a factor of 2-4 lower for MPSs operating near the resonance energy when compared to a bremsstrahlung source (19 MeV endpoint energy). Alternatively, energies <10 MeV avoid production of most photoneutrons, expediting use prompt neutron signature, which was the strongest fission signature for the cases studied. At such energies the MPS dose advantage can be more than a factor of 50. Simulations evaluated use of various photofission signatures to detect 18 kg HEU objects in a variety of shielding configurations including steel and composite B-poly/lead of varying thicknesses. Sources with narrow angular divergence (~mrad, so that the photon-beam spot size on target is comparable to or smaller than the SNM) along with intense beams (sufficient to generate detected photofission signals well above background), are important to reduce overall dose to the object and environment. Operating an MPS at 13.1 ± 25% MeV (8.5×10^8 photons per source pulse on target, after collimation) for delayed signatures and 6.7 ± 20.5% MeV (6.9×10^8 photons per source pulse) for prompt neutrons maximizes fission production without generating problematic levels of source-induced background or signature interferences. Positively identifying the presence of fissionable material was shown to be realistic for the configurations analyzed in minutes, at ranges of 20 m and through shielding thickness up to 30 cm using a source producing ~ 10^{12} photons/second within few mrad divergence emission angle.

The results inform the size of a shielded object within which absence could be determined, and indicate that such a measurement could be realistic in objects at the ~1 m^3 size range using a narrow-divergence MPS. Even with such a source, localization and coarse size determination of a shielded object of interest is crucial to allow determination of absence. An appropriate backscatter measurement may expedite measurements by identifying high-Z or high-density areas, consequently localizing a region of interest.

Treaty/Dismantlement Verification and Stockpile Stewardship

Verification of nuclear warheads and their dismantlement is a high priority for treaty verification. Both NRF scattering and transmission are promising techniques for measuring material characteristics in the context of treaty verification. MPS-based photon sources provide an order-of-magnitude or more performance improvement over bremsstrahlung-based sources. NRF scattering generally performs better than NRF transmission in this application. Using a photon source operating at 10 kHz with a 2% FWHM energy distribution, detection of quantities of interest of HEU, Pu, and HE are possible in times typically of a few minutes. The required photon intensity is relatively modest at less than $2 \cdot 10^6$ γ/shot on target (after collimation). The primary limitation to reducing the time-to-detection/confirmation is the total rate on the detector; if the total rate is too high, pileup will occur obscuring the signal. Evaluation of different filtering options in front of the detector may improve that situation. Alternatively, if one could develop a fast threshold counting detector, it may be possible to significantly reduce the times-to-detection/confirmation. Because of the limitation on photon intensity to limit detector rate, the time to detection will be approximately proportional to the width of the energy distribution and inversely proportional to the repetition rate. Treaty/dismantlement verification does not require a high photon flux per shot. Hence for this application, development of high repetition rate and low energy spread are priorities over peak flux per shot. The MPS must be able to target the energy of each NRF line, which for most technologies in practice requires continuous energy tuning. Photofission signatures were also evaluated using

energy dependence of the cross section and a variable energy MPS. While individual materials can be identified in this way, it is not clear effects of multiple materials of unknown order can be resolved, making NRF the more desirable signature.

High resolution imaging for stockpile stewardship may provide a valuable tool for treaty and dismantlement verification involving nuclear warheads. Discussions with stakeholders in these communities identified a strong interest to 'fingerprint' individual weapons by deriving an intrinsic unique identifier (I-UID). If an MPS-based system were already used in stockpile stewardship efforts, familiarity with the technique and experience using it on the stockpile would ease the transition for use in treaty verification. If the focus is on resolving smaller spatial features, an MPS-based system has the potential to reduce the size of observable features by a factor of 5 or more in equal exposure time, and potentially by a factor of ~200 (likely with longer exposure time), compared to CoLOSSIS. Furthermore, the MPS does not suffer from beam hardening due to its much narrower spectrum and scatter effects are considerably reduced because of the small beam angular divergence.

The potential impact of MPS-enabled techniques for treaty verification measurements could be very significant. An MPS may enable warhead confirmation, for which there is currently no known solution, as well as enabling a unique identifier for warheads and components through high-resolution radiography. In addition, a system suitable for warhead confirmation could likely be used for dismantlement confirmation, which would reduce the number of instruments required for treaty verification.

Nuclear Safeguards

In nuclear safeguards, verification of the content of spent fuel dry-storage casks to reestablish inventory after loss of continuity of knowledge (CoK) was identified as an important need that has not been met. The IAEA is actively pursuing a method that allows re-verification of LWR spent fuel stored in dry casks. The thick walls of dry storage casks and the additional attenuation and scatter in the stored assemblies make radiographic measurements for the verification of the canister content very challenging. High flux, narrow divergence MPS 'pencil' beams mitigate these challenges, and transmission could be measured along specific paths through the cask. The assembly basket occupancy, and in certain cases even missing pins, may be deduced from measured chord transmission. A photon source that produces an intense, low divergence photon beam in the 6 - 8 MeV energy range and high yield, at or above $1 \cdot 10^{12}$ ph/s on target (after collimation), is required to overcome the main challenge, which is low transmission through the massive cask. A pulsed source is needed so that the detector can be gated with the beam pulse so that only coincident photons are accepted. Such a source allows a scan for verifying assembly occupancy in a few hours in a transverse scan, where the beam propagates across the assemblies. A transverse scan is required for casks which are stored vertically and which cannot be repositioned. For casks stored horizontally, scans can be conducted along the long axis of the fuel bundles, which considerably reduces the complexity of determining occupancy. In this case, a MPS with mrad divergence provides sensitivity to individual fuel rods.

Summary

In summary, simulations show that MPSs can offer significant benefit to cargo screening, detection, warhead and dismantlement verification, and nuclear fuel cask scanning. They indicate that these benefits are also likely to impact emergency response and many other application areas both within and outside nonproliferation work. Full benefit is realized with an MPS having adjustable energy in the 1.5-15 MeV range, narrow (ideally mrad) emission angle, energy spreads from approximately 20% for radiography and photofission down to <2% for NRF, and with photon

fluxes delivered to the target ranging from 10^{10} photons/second for initial capabilities to 10^{12} photons/second for high performance. These parameters match with the development outlook for Thomson/Compton based photon sources, provided that such systems can be made sufficiently compact and can operate at the required repetition rates of kHz for initial capabilities up to tens of kHz for high performance. The parameters are further detailed in Section III. A separate final report integrates these simulations with initial assessments, survey of the literature, and an assessment of the development requirements for MPS technologies to meet application needs. New signatures enabled by such sources may offer additional benefit, but were not simulated in detail under this project.

Table of Contents

I. Introduction

Near-monoenergetic photon sources (MPSs) have the potential to improve sensitivity at greatly reduced dose in nonproliferation applications and related areas, particularly where passive signatures do not penetrate or are insufficiently precise. MPS advantages include the ability to select energy, energy spread, flux, and pulse structures to deliver only the photons needed for the application, while suppressing extraneous dose and background. Some MPSs also offer narrow divergence photon beams which can target dose and/or mitigate scattering contributions to image contrast degradation. Current broad-band, bremsstrahlung photon sources (e.g., linacs and betatrons) deliver unnecessary dose that in some cases also interferes with the signature to be detected and/or restricts operations, and must be collimated (reducing flux) to generate narrow divergence beams. While MPSs can in principle resolve these issues, source parameters differ for various candidate technologies being developed, and additionally trade off against one another (for example, tight constraints on beam energy spread will reduce available photon intensity for MPSs based on Thomson scattering). For many applications, the size and operability of an MPS and its support systems are also key restrictions. These tradeoffs, together with differences in detectors and backgrounds represent a large operation space which must be characterized in order to understand and define needs for each application, and hence to develop and deliver a system with improved performance.

A broad range of nonproliferation applications was assessed where monoenergetic photon sources (MPSs) may enable new capabilities or significant performance enhancements as described in a separate report [1]. Four nonproliferation applications were identified and prioritized for further study and detailed analysis: cargo screening and interdiction of Special Nuclear Materials (SNM), detection of hidden SNM, treaty/dismantlement verification, and spent fuel dry storage cask content verification. The evaluation of treaty applications includes high-resolution imaging with first application to stockpile stewardship (because techniques for treaty verification may be verified first through stockpile stewardship measurements) and subsequent application to weapon identification in a treaty context. Preliminary analysis indicated that there is significant potential benefit for each of these applications, and that the photon source requirements are likely within range of realistic MPS candidates. Initial results were presented at several conferences, including SORMA, IEEE Nuclear Science Symposium and Nuclear Photonics, and insights from follow up discussions with cargo applications experts were incorporated into the simulation study [2].

This report presents detailed simulations and evaluations of the selected applications. Results for each application are described in section II of this report. In the evaluation of the impact that monoenergetic sources would have on each prioritized application a range of system parameters were considered including natural and induced background radiation, beam propagation to a target, penetration, signature generation, detection sensitivity, and radiation dose to target and operators. Performance of potential monoenergetic photon sources was evaluated in the context of each application, including source tradeoffs and constraints (e.g., bandwidth, intensity, pulse structure, divergence, portability/shielding, and detector needs). Simulation results were used to provide high-level MPS requirements, presented in the conclusion of each subsection of section II, and summarized in section III, for the four selected applications. This report is incremental to the separate report on the survey of applications, and of past work [1]. For that reason it does not include comprehensive references or background. A final report combines this report with the broader initial assessment and also includes a high-level sequence for the potential MPS development path, including application performance verification measurements, outlining a coordinated program to deliver high-impact, next-generation systems with greatly reduced dose and increased detection and measurement capabilities. That report is the record of the project.

I.1 Monoenergetic Photon Sources and Applications for Nonproliferation

The simulation studies performed assessed the impact of MPSs on the prioritized applications including the consideration of tradeoffs and constraints of candidate source technologies. Important MPS characteristics for applications may include not only photon beam energy spread, but also selectable energy, beam angular spread (divergence), emission spot size, and temporal pulse structure. Each could provide advantages (and in some cases restrictions) to advance performance of the principal measurement techniques used in nonproliferation photon source applications:

- Improved radiography (R) with better contrast, Z discrimination, and spatial resolution,
- Higher photo-fission (PF) sensitivity due to increased fission rate per unit dose, and reduced background,
- Enabling Nuclear Resonance Fluorescence (NRF) techniques due to high spectral density and narrow energy spread.

Bremsstrahlung-based broad energy spread photon sources are presently used, especially for radiography and photofission, but are frequently restricted in penetration and/or resolution by dose and other constraints. By eliminating low-energy photons that do not contribute to the desired signal, narrow energy spread reduces radiation dose to the object and surroundings, and also improves signal-to-noise ratios and thus sensitivity. Signal-to-background ratios may be further increased by selecting the optimal photon energy for a specific application and measurement. Narrow beam divergence (the solid angle into which monoenergetic photons are emitted) may enable higher resolution imaging, improved contrast by reducing scatter contributions, variation of dose across an object to ensure sufficient penetration (i.e., higher dose for pixels with higher density), and delivery of a high photon flux into a small area. Small emission spot size (the area from which monoenergetic photons are emitted) can improve high-resolution radiography. The time structure of the beam could be pulsed to enable prompt signatures, or near-continuous/high repetition rate for counting measurements.

The principal MPS technologies are Thomson scattering, which covers a wide range of beam parameters and has narrow beam divergence but conventionally has required large accelerators, and nuclear reaction sources, which due to their nature are limited to selected energy spectra and photon emission into 4π. Other candidate source technologies were considered as part of the initial assessment but are not under active development and were not addressed by simulations. A full discussion of the state of the art, including references, is presented in [1], and is summarized here.

Thomson scattering (also referred to as Compton or inverse Compton scattering) of a laser from a counter-propagating electron beam is a well-established source of near-monoenergetic MeV photons. Photon beam energy, yield, energy spread and polarization are continuously tunable by adjusting the electron beam and scattering laser. Correspondingly, a high quality electron beam is required for narrow photon energy spread, and photon beam intensity and angular divergence are correlated with photon energy and energy spread. Here we consider Thomson sources at nonproliferation-relevant energies of 1-20 MeV, which require GeV-class electron accelerators that are historically large facilities. Several projects are under way to enable transportable systems by using either laser-plasma based accelerators and systems or advancement of conventional accelerators. Current Thomson sources have repetition rates at or below 100 Hz for conventional accelerators, and below 10 Hz for plasma based systems. However it is anticipated that future lasers will allow 1 kHz to potentially 200 kHz rates over time. The photon beams have narrow (mrad) divergence, which requires rastering of the beam across an object for many applications. Achievable intensity within this narrow divergence is high: kHz repetition rate corresponds to yields that could be in the range of 10^{10}-10^{11} photons/second on target. Present energy spreads are

at the few percent level for conventional accelerators, and above 10% for plasma based systems. For the longer term, sources down to 0.1 % energy spread via fine control of electron beam focusing have been proposed. Photon emission will be in short bursts (picoseconds to femtoseconds in duration), and repetition rate must be matched to the application.

Candidate nuclear reaction sources include $^{11}B(d,n\gamma)^{12}C$, which produces photons both at 15.1 MeV and in multiple lines around 2-5 MeV and neutrons. The emission of gamma rays at high and low energies could be exploited for Z-discrimination based on dual energy transmission. The gamma rays at 15.1 MeV as well as the neutrons produced in the reaction could be used to induce fission. Other candidate reactions include $^{11}B(p, \gamma)^{12}C$ with energy lines at 4.4 MeV (97%), 11.7 MeV (97%), and at 16 MeV (3%). Gamma rays at 15.1 MeV can also be produced by the inelastic scattering of protons on ^{12}C ($^{12}C(p,p'\gamma)^{12}C$). Emission is unpolarized and broad in angle, covering 4π. Designs have been proposed for systems capable of yields in the range of 10^8 to (at very high current) 10^{11}photons/second into 4π (i.e. 10^7 to 10^{10} photons/second/Steradian). The useful number depends on the collimation geometry used. Multiple narrow-collimated beams may be prepared relatively easily with appropriate collimator design, in which case a nuclear reaction source could be used to simultaneously probe multiple objects. Such sources also can be used to produce neutrons which can be used to discriminate among various isotopes. For example, 7Li(p,n) can produce tunable and directional neutron beams. Detailed assessment of neutron signatures was beyond the scope of this report. The beam can be continuous or pulsed depending on the ion accelerator used.

The assessed potential performance of both Thomson/Compton and nuclear reaction based MPS candidate technologies were used as constraints on the simulation inputs. This includes both potential yield, which may constrain sensitivity, and also source tradeoffs (such as energy spread vs. yield for Thomson sources) that impact use scenarios. MPS candidates were compared to bremsstrahlung-based systems, as used currently, that produce continuous energy spectra up to a cut-off energy given by the energy of the electron beam energy used to generate them. Typical energies include 3, 6, and 9 MeV. Variation of parameters was assessed to understand which parameter ranges deliver benefit for each application. Extrapolation of performance is discussed to assess performance in cases where yield beyond that of near-term MPS candidates would be desirable. This report focuses on radiography, photofission, and NRF measurements, and the photon beam characteristics important to each. New or extended measurement techniques, which could be enabled, are also in some cases identified, but are beyond the scope of this report to detail. These include backscatter radiography, polarized photofission and photoneutron spectroscopy.

I.2. Summary of Initial Assessment of Applications

A broad range of nonproliferation applications was initially assessed where monoenergetic photon sources (MPSs) may enable new capabilities or significant performance enhancement. This assessment is reported separately [1], including references, and is briefly summarized here. The initial calculations were used as basis for the detailed simulations, and to avoid simulation of unrealistic cases. Based on this assessment, applications were prioritized for detailed analysis during the second phase of the study. Selected were: cargo screening and interdiction of Special Nuclear Materials (SNM), detection of hidden SNM, treaty/dismantlement verification, and spent fuel dry storage cask content verification. Discussions with DNN R&D and their stakeholders, and assessment of prior studies, identified these areas as of strong interest to nonproliferation. Preliminary analysis indicates that there is significant potential benefit for each of these applications, and that the photon source requirements are likely within range of realistic MPS candidates.

Screening for and interdiction of SNM, typically in cargo containers, train cars and trucks, is a priority application for the Department of Homeland Security (with the Domestic Nuclear Detection Office, DNDO, as the development and procurement agency and Customs and Border Protection, CBP, as the user), as well as other agencies (e.g., the Department of Energy Nuclear Smuggling Detection and Deterrence program - formerly Second Line of Defense). Access to both sides of the object is typically available, which facilitates use of radiography, photofission, and nuclear resonance fluorescence. The primary photon source-based screening method for cargo containers is radiography with Z-discrimination (including low-Z materials due to the importance of dual use by CBP and others). Initial evaluation shows strong dose reduction benefit from MPSs with moderate energy spread at the 20% level. MPSs with narrowly collimated pencil beams (i.e., beams of narrow angular spread, or divergence) additionally mitigate scattering degradation of contrast suffered by current bremsstrahlung fan beam sources. Reduced dose could ease operational constraints, or could be used to penetrate thicker cargo within prescribed dose limits. Cargo thickness can vary significantly within a container and a pencil beam configuration enables dose adaptation on a pixel by pixel basis (i.e., delivering appropriate flux to penetrate pixels of variable radiographic thickness) further reducing dose to the bulk of the cargo. Photon fluxes of $\leq 10^8$ photons/shot or a few times less at repetition rates of 5-50 kHz appear suitable for scanning at 0.1-1 m/s using pencil-beam sizes of 1-4 cm^2 through thicknesses of ~40 cm of steel. Secondary screening for SNM typically uses photofission. MPSs could enable use of photon energies above the fission threshold but below 10 MeV, which is of interest for screening applications where photon energies may be restricted. The dose required to detect fissile material could be reduced by more than a factor of 50 due to the greater fission probability per photon compared to a bremsstrahlung source at ~10 MeV energies.

Detecting hidden SNM was considered separately from screening to address scenarios where access to the object/container of interest is limited to one side (at most, 180°). These scenarios are of interest to DNDO for inspection of parked vehicles, to emergency response, and potentially to the Defense Threat Reduction Agency. Photofission is an appropriate method for one-sided access in combination with techniques such as backscatter radiography to first localize high-Z areas to be probed with photofission. MPSs can significantly reduce doses to the object for photofission by delivering only on-resonance photons. The strongest photofission signal is obtained near the photofission resonance energy of ~15 MeV. The imparted doses are approximately a factor of 2-4 lower for MPSs (at 14 MeV) compared to a bremsstrahlung source (19 MeV endpoint energy), i.e., at energies optimized for stimulating delayed signatures. The MPS dose advantage for the prompt neutron signature is much higher, because in this case the source photon energy is limited to 10 MeV (to avoid interference from (γ,n) neutrons), as in the cargo screening application. Sources with narrow angular divergence (so that the photon-beam spot size on target is comparable to or smaller than the SNM) along with intense beams (sufficient to generate detected photofission signals well above background), can further reduce overall dose to the object and environment and would also improve detection of SNM at longer distances.

Verification of nuclear warheads and their dismantlement is a high priority for treaty verification. Photofission, NRF, and radiography were identified as techniques for which MPSs could provide significant performance improvements compared to bremsstrahlung photon sources. NRF measurements provide isotope-specific information, and could play a significant role in warhead confirmation and dismantlement confirmation. It is possible to identify and characterize individual isotopes, enabling the NRF techniques to be used for measurements related to both fissile materials and HE. The advantages of a MPS versus bremsstrahlung source are lower dose and faster measurements. NRF prioritizes high intensity beams (~10^{10} photons/s) with a narrow energy spread at the ≤2% level (ideally sub-percent) and repetition rate of 10 kHz or greater. A path to warhead and component "fingerprinting," providing unique identifiers of individual devices,

could be provided by use of high-resolution radiography / tomography, which could be combined with Z discrimination and NRF. This approach would provide very specific information needed for fingerprinting and would also be applicable to stockpile management. Photon emission spot size would be an important determinant of achievable resolution.

In nuclear safeguards, verification of the content of spent fuel dry-storage casks to reestablish inventory after loss of continuity of knowledge (CoK) was identified as an important need that has not been met. The primary challenge in this application is penetration of the thick cask walls or lids for determining assembly basket occupancy. Attenuation and scattering are severe, precluding traditional radiography, but MPS-based chord transmission measurements with high flux pencil beams could in principle provide a solution. Transmission measurements appear promising with a pencil beam divergence of ~2 milliradians, a beam intensity on the order of 10^{12} ph/s, and short beam pulses (<1 ns) for background suppression. The assembly basket occupancy, and in certain cases even missing pins, may be deduced from measured chord transmission.

Other safeguards applications where brief assessment indicates potential for significant benefit include spent fuel assay, "fingerprinting" of spent nuclear fuel (SNF) assemblies, enrichment, input accountancy for pyroprocessing, and materials assay in accident scenarios. These applications could benefit from future very high performance MPSs with energy spreads on the order of 0.1% and high beam intensities on the order of 10^{11}-10^{12} ph/s that could enable transmission NRF for the direct measurement of isotopic content. Detailed simulations were deferred due to limited resources available, the high required MPS performance and relatively low priority in safeguards.

Additional applications and possible new methods/signatures were identified and initial analysis was reported [1]. Detailed assessments of these additional topics were beyond the scope of the detailed simulations reported here. Section III of this report includes extrapolation of the results presented here to indicate strong potential benefit to emergency response applications. The emergency response analysis also indicates benefit for medical imaging, and industrial nondestructive analysis. Other applications include: photonuclear data, spent fuel assembly assay, materials characterization in accident scenarios, waste drum content, fuel quality control, and pyro processing monitoring. Possible new methods/signatures include: backscatter radiography to constrain detection volume, 'Few view radiography,' computer tomography or EZ3D-like systems for clutter resolution, polarized photofission, isotope-specific energy dependence of fission cross sections, photoneutron spectroscopy, and angularly resolved scattering. These applications and signatures are possible topics for extended or future work. No important capability enhancement was identified for UF_6 cylinder enrichment or nuclear forensics.

II. Assessment of Prioritized Applications

II.1. Cargo Screening and Interdiction of Shielded SNM

II.1.1 Introduction

This application section considers screening to prevent smuggling onto US soil of illicit radiological or special nuclear material (SNM) hidden in cargo containers, which remains a critical national security issue and a challenging technical problem. Similar challenges apply to other common cargo modes, including train cars and trucks. Screening techniques should clear vehicles accurately and must minimally affect the flow of commerce, which imposes severe constraints on scanning time and acceptable false positive rates: a positive event flags a container for inspection imposing added delays and costs. Cargo container screening, and by extension vehicle screening, for the detection of hidden SNM is generally viewed as a multiple stages process with the goal to quickly clear a vast majority of containers while a small percentage will be flagged as suspicious and will require additional screening. Radiography is the first method to identify dense regions of the cargo. Dual-energy radiography is being developed to differentiate low Z from high Z materials by taking advantage of the difference in relative importance of Compton scattering and pair production processes as a function of Z and energy. Where a radiograph shows a region of interest within the container or vehicle with a suspicious high Z material, it is envisioned that the container could then go though a final screening step to resolve the alarm, i.e., to unambiguously ascertain the absence of SNM. These active interrogation systems are still in the research and development stage and are not yet deployed. They rely on the characteristic signatures of fission, namely prompt neutron and delayed gamma and neutron emissions, or on nuclear resonance fluorescence (NRF).

The large available volume of a container and the relatively small SNM significant quantities make detection challenging. Photon scatter in cargos has proven to be a significant contribution to the signal detected in radiographic images and can lead to degraded contrast. Commonly, when cargos are sufficiently thick or dense to limit beam transmission, radiographs show very little to no information due to a lack of signal and a lack of contrast. The ability to penetrate 20 and 40 cm of steel is one of the tests used to gauge the performance of a screening system: the areal density of a 40 cm thick steel object at full density is twice the areal density of a homogeneously filled container (which would be 240 cm in thickness at 0.6 g/cm^3), and could represent a conservative approximation of some of the denser objects found in cargos. Z discrimination tests include the ability to resolve a small high-Z object hidden behind thick steel shielding. Final screening for alarm resolution using photofission or NRF must also be evaluated in similar shielding scenarios. Additional important performance metrics include spatial resolution sufficient for the significant object of interest, scanning speed, and radiation dose.

Several MPS characteristics could lead to important capability improvements in cargo applications. An earlier report identified techniques for which MPSs could provide significant performance improvements compared to bremsstrahlung photon sources [1]. A full discussion of the state of the art, including references, is presented in [1], and is summarized here. Initial results were presented at several conferences, including SORMA, IEEE Nuclear Science Symposium and Nuclear Photonics, and follow up discussions with cargo applications experts were incorporated into the definition of the simulations [2]. This section presents higher-fidelity calculations and modeling results to evaluate radiography, as well as photofission and NRF. The first subsection presents description of the photon beams used in subsequent simulations. For radiography, the ability to select the optimal beam energy which can maximize transmission and minimize dose is

next evaluated without scattering, indicating MPS advantages of three to four-fold due to energy spectrum alone. Simulations are then described which evaluate the effects of scattering on image quality, showing that the greatest benefit is obtained by photon sources with narrow divergence pencil beams which are scanned across the target. Improved Z-discrimination is next assessed by evaluating use of ratios of discrete MPS energies versus continuous bremsstrahlung distributions. Scattering contributions to Z discrimination resolution are included. Use of small beam divergence MPSs to allow pencil beam scanning is found to allow a reduction of the scatter contribution to image degradation, and for 2D dose adaptation as a function of cargo spatial distribution. Lastly, secondary screening is evaluated where MPSs can also generate stronger photofission signatures and enable more sensitive NRF measurements.

II.1.2 Simulation Study Setup: Bremsstrahlung Beams

The energy distribution of the photon source in a radiographic system defines transmission through cargo, which is one important determinant of the dose required to form an image. Some commercial bremsstrahlung systems at 6 and 9 MeV are built with beam hardening filters and report beam average energies around 2 and 3 MeV respectively, which improve transmission. To allow comparison with MPS candidates, bremsstrahlung beams were modeled for use in the simulation study.

Energy spectra were first calculated for unhardened 6 and 9 MeV bremsstrahlung beams as a function of angle in 1 degree increments and then transmitted through representative hardening filters of 0.5 cm of Cu and 1.0 cm of W, respectively using the NIST XCOM data [3]. The resulting spectra are shown in Figure 1. The average energy of the attenuated on-axis beams and overall transmission compared to the unhardened beams are summarized in Table 1. While the W filter reduces the contribution from the low energy photons as shown by the increase in average energy of the beam, the intensity is also significantly reduced to 30% of the unhardened beam. The W hardened spectrum is used in the simulations presented here because of its improved transmission due to the higher mean energy. This represents a 'best-case' bremsstrahlung source. This beam was compared to MPS beams of various energy spreads to assess potential MPS benefits to applications.

Table 1. 6 and 9 MeV simulated Bremsstrahlung beams on-axis.

Energy endpoint	6 MeV			9 MeV		
Filter	Unhardened	0.5 cm Cu	1 cm W	Unhardened	0.5 cm Cu	1 cm W
Average Energy [MeV]	1.29	1.41	1.83	1.73	1.89	2.37
Transmission through filter compared to unflattened beam	-	76.4%	28%	-	78%	31%

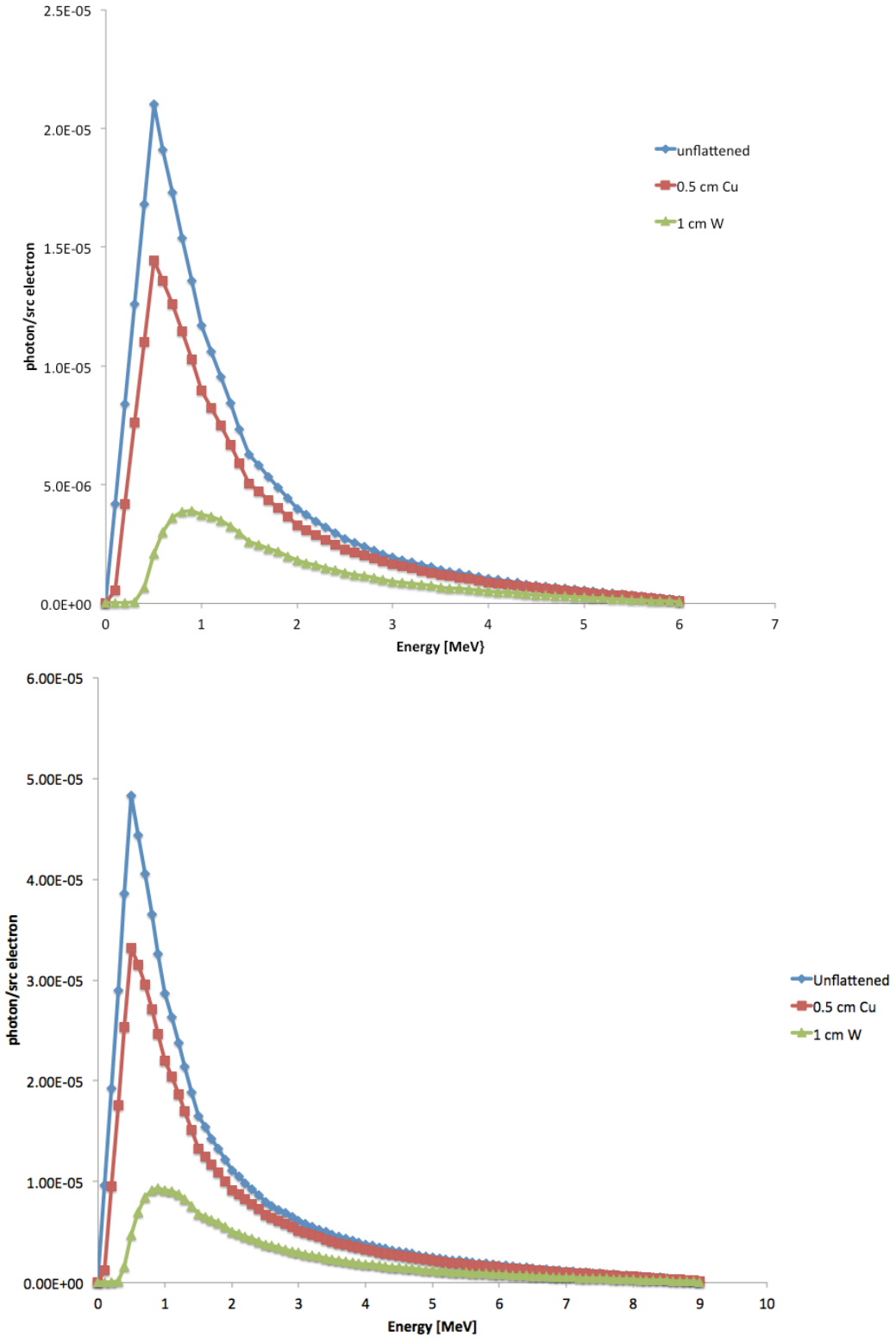

Figure 1. 6 MeV (left) and 9 MeV (right) simulated Bremsstrahlung spectra unhardened (blue), with 0.5 cm Copper hardening filter (red) and 1 cm W hardening filter (green).

II.1.3 Simulation Results: Radiography

Potential radiography capability improvements for cargo screening from use of MPSs were evaluated in comparison to bremsstrahlung beams. Simulations were performed to estimate benefits in transmission, dose reduction and Z-discrimination due to the advantageous energy spectrum of an MPS. Simulations included the impact of the scatter contribution to the image and potential mitigation via control of both the photon beam energy spectrum and angular spread. The later is important to evaluate the difference between the fan beams produced by most bremsstrahlung sources and MPSs, which may produce fan, cone or narrow-divergence pencil beams. The latter would be scanned across a target to form an image.

Transmission and Dose Advantages Due To Energy Spectrum

Using a MPS can result in a significant gain in transmission compared to a Bremsstrahlung source, which could result in shorter irradiation times, lower doses or improved statistics. MCNP simulations were performed to calculate transmission for MPS and bremsstrahlung beams at several energies through 20 cm and 40 cm of steel and to evaluate doses to the cargo and to a potential stowaway per source photon. The transmission results indicate the dose impact due to energy spectrum alone. For a full evaluation of the MPS impact on dose these results must be convolved with results of simulations determining the impact of source angular spread (i.e. narrow angular spread sources can reduce scattering impact, reducing the number of photons required to form an image, and hence dose), as discussed in following sections, and benefits of dose modulation across the cargo enabled by scanning with a narrow divergence MPS beam must be considered.

A two-step approach was taken to compare different beam types in terms of dose to a stowaway. A first set of simulations calculated the transmission as the dose per source photon deposited in a 1 cm x 1cm $CdWO_4$ detector either 3 cm or 10 cm long by a pencil beam penetrating 20 cm and 40 cm thick steel centered in a cargo container. The dimensions of the container are 1.2 m x 2.4 m x 2.4 m. The detector face is located 80 cm from the exit wall of the container, or 200 cm from the center of the container. The detector is sandwiched between tungsten collimator leaves extending 30 cm from the face of the detector. This configuration shields the detector from lateral secondary scatter contribution. The simulated doses-to-detector/source-photon values for the beams considered are listed in Table 3.

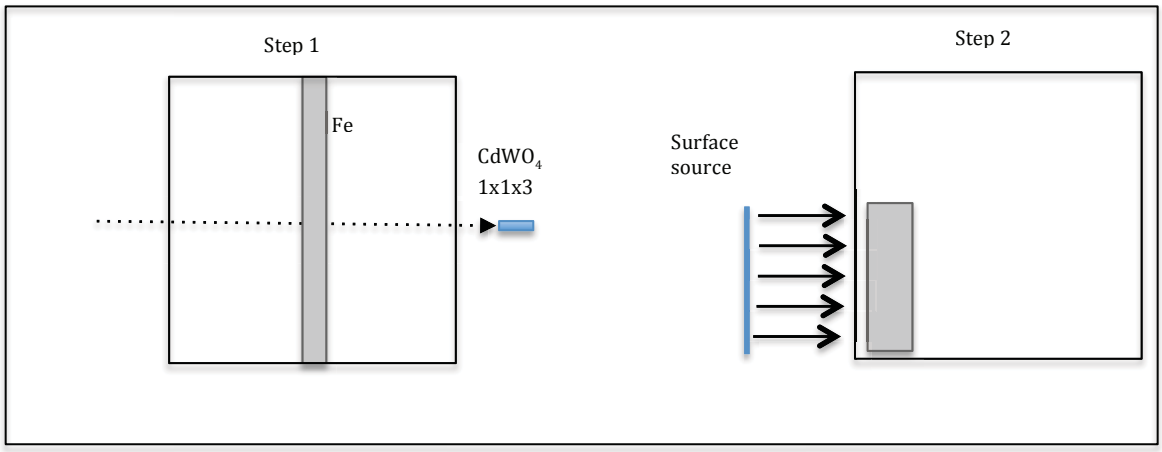

Figure 2. Models for the detector dose simulations (left) and body dose (right).

In a second step the body dose is simulated with a model that includes a vertical water cylinder 180 cm high and 40 cm in diameter inside a cargo container to emulate a human body, next to the

wall facing the source (Figure 2). The photon source is a surface source with a cross section identical to the body dimensions, i.e., 40 cm wide by 180 cm high and photons are emitted normal to the source plane and perpendicular to the cylinder axis. Bremsstrahlung beams were hardened with 0.5 cm of Cu or 1 cm of W as described above. Results are summarized in Table 2. As expected, the dose per source photon is higher for an MPS at a given energy than for a Bremsstrahlung source with that endpoint energy. This is because the MPS delivers all of its photons at the target energy, while most of the bremsstrahlung photons are at lower energies. Understanding the dose required to form a radiograph requires convolving this effect with the transmission data obtained in the first set of simulations.

Table 2. Simulated doses per source photon in the water cylinder for hardened bremsstrahlung beams and MPS beams.

Energy [MeV]	Bremsstrahlung [Gy/source photon]		MPS [Gy/source photon]	Dose Ratio MPS/Brems	Dose Ratio MPS/Brems
Brems. filter	1 cm W	0.5cm Cu		1 cm W	0.5cm Cu
3 MeV	-	-	1.01e-15		
6 MeV	6.33e-16	4.90e-16	1.75e-15	2.76	3.57
9 MeV	7.83e-16	6.27e-16	2.42e-15	3.09	3.86

For each beam type and energy, the body dose was normalized to the corresponding detector dose to obtain the dose comparison for a radiograph. In this comparison the beams differ only in their energy spectrum. The results are given in Table 3. Note that simulations for a 10-cm long detector resulted in detector doses smaller by a factor of ~2 for all cases, thus the final dose ratios were essentially unchanged by the detector type. This is as expected since the detector length essentially sets efficiency. For this reason, only one set of dose ratios is reported. Column six (far right) reports the ratio of dose imparted by a Bremsstrahlung source to that imparted by a MPS, under conditions where both deliver equal dose to the detector (transmission). This measures the part of the dose advantage of an MPS over a bremsstrahlung beam that is due to difference in energy spectrum alone.

Table 3: Ratios of expected water phantom doses for MPS and bremsstrahlung spectra, for same detector signal after penetrating 20 cm and 40 cm thick steel.

Steel thickness [cm]	Energy [MeV]	Beam type	Detector dose/src-photon [Gy]	Water phantom dose/src-photon [Gy]	Dose ratio Brems/MPS
20	3	MPS	2.6e-14	1.0e-15	1.3
	6	Brems	1.3e-14	6.3e-16	
	9	MPS	2.7e-13	2.4e-15	3
	9	Brems	2.9e-14	7.8e-16	
40	3	MPS	9.5e-17	1.0e-15	0.84
	6	Brems	7.1e-17	6.3e-16	
	9	MPS	2.6e-15	2.4e-15	4
	9	Brems	2.1e-16	7.8e-16	

The photon energy deposited in the detector per source photon, given in column 4 in Table 3, is ~10x higher for the 9 MeV MPS beam compared to the 9 MeV bremsstrahlung beam with 1 cm W filter which could mean ~10 times fewer MPS photons are needed to generate an image. However, this does not translate into a reduction of the dose to the container by the same factor since the

dose per incident photon for 9 MeV MPS is ~3 times that of a 9 MeV bremsstrahlung beam. To penetrate a 20 cm thick steel cargo, the dose for a 9 MeV MPS is lower by a factor of ~3. This dose ratio increases to a factor of ~4 for 40 cm thickness. When the 9 MeV MPS is compared to a softer Bremsstrahlung beam filtered with 0.5 cm of Cu, the 9 MeV MPS doses are similarly lower by a factor of 3.06 and 4.14 respectively. Note that the transmission of a 3 MeV MPS beam is only moderately higher than that of a 6 MeV bremsstrahlung beam resulting in similar doses to cargo. Practically, applications for a 3 MeV beam are likely limited to small cargos or as part of a dual energy radiography system with few views. The simulation results evaluate transmission for realistic cases relevant to screening, and indicate that in the absence of scattering contributions, the dose reduction due to MPS energy spectrum alone is in the range of 3x-4x. Estimation of the total dose reduction requires convolving this result with simulations including scattering using the beam emission angle geometry of a particular MPS.

Scatter Reduction, Contrast Enhancement, and Resulting Dose Reduction

Scattering is a significant contributor to image quality degradation in existing cargo radiography systems, and simulations were conducted to evaluate the impact of MPSs in reducing these contributions. Scattering contributions can be affected by energy distribution, detector configuration, and by source emission angle (e.g. fan, pencil or cone). Simulations evaluated each of these effects. First, propagation of a bremsstrahlung and a monoenergetic pencil beam through a steel plate was modeled to investigate scatter contribution and beam intensity profile as function of distance from the plate.

To visualize the effect of scattering on the photon beam and the effect of detector stand-off distance, propagation of a 9 MeV pencil beam (i.e., a monodirectional beam with no spatial extent) was simulated using the MCNPX code through 1 m^2 steel plates, 20 and 40 cm thick. Both a 9 MeV monoenergetic beam and a bremsstrahlung spectrum with 9 MeV endpoint energy were simulated in this configuration. The flux is calculated with a mesh tally in MCNPX, using voxels 1 cm on a side in the plane of the beam. Figure 3 shows the photon flux map for the 9 MeV MPS propagating through 40 cm of steel. The beam is heavily attenuated by the steel, and photons are scattered out of the beam into the steel. Lineouts are shown in Figure 4 for the 20 cm case and in Figure 5 for the 40 cm case. In each figure, the plot corresponding to the downstream edge of the steel (located at d=0 cm in the fluence map) shows a significant portion of the photons in the beam are scattered out of the beamline. At modest distances after the steel, indicated by the dashed line at 100 cm, the unscattered beam is still very tightly focused while the scattered flux is low since the scattered photons have a wide angular distribution. At 100 cm from the surface of the steel, the scattered intensity is typically three orders of magnitude below the transmitted beam intensity. This indicates that for a narrow divergence beam, scattering contributions to image contrast degradation will be very small. The sum of the scattered photons observed on a linear detector array covering ±50 cm from the central beam location is about 6% of the transmitted beam flux for the 40cm steel plate, and near 2.5% for the 20 cm steel plate. Similar simulations were conducted for bremsstrahlung sources with 9 MeV endpoint energy. These showed modestly larger scattering, with total scattered photons observed on a linear detector array covering ±50 cm from the central beam location being about 7% of the transmitted beam flux for the 40cm steel plate, and near 3% for the 20 cm steel case.

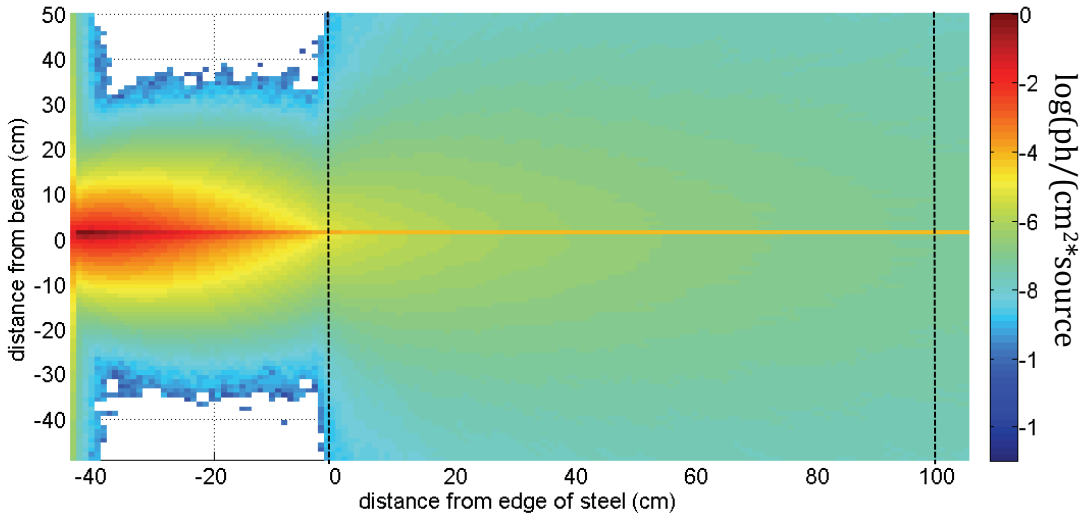

Figure 3. 2D Flux map in a plane through the beam axis for a 9 MeV photon beam penetrating 40 cm of Steel, dashed lines at locations of voxel rows used for flux measurements in figs. 4 and 5.

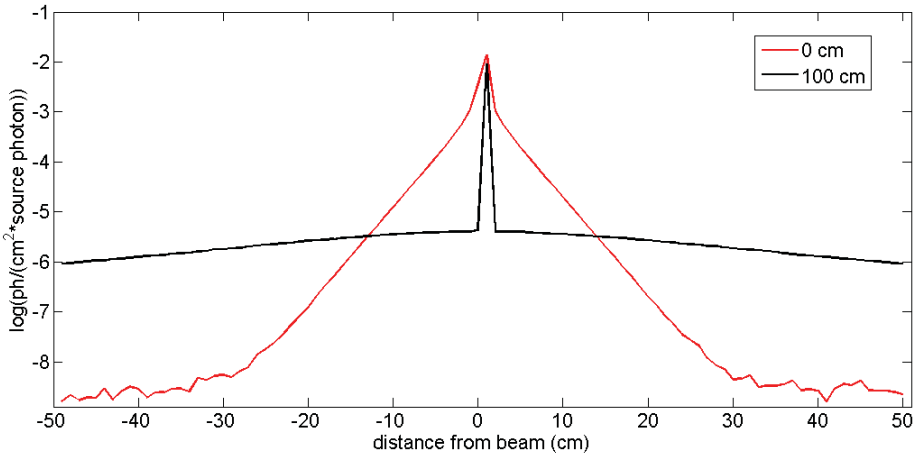

Figure 4. Flux measured in row of voxels for a 9 MeV photon beam penetrating 20 cm thick steel, measured at the exit of the steel slab (0cm) and 100 cm downstream.

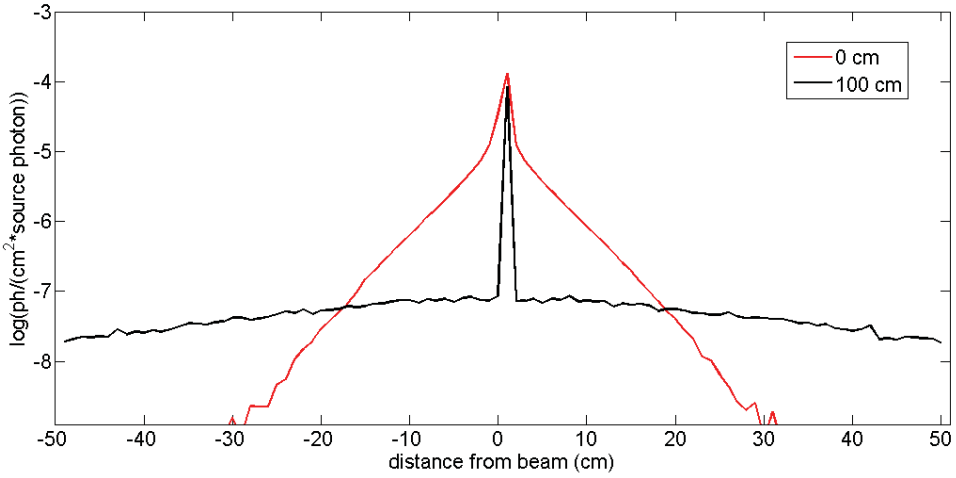

Figure 5. Flux measured in row of voxels for a 9 MeV photon beam penetrating 40 cm thick steel, measured at the exit of the steel slab (0cm) and 100 cm downstream.

The fraction of the photons observed in detector pixels outside the transmitted beam location can be used to give a qualitative first indication of the effects of the observed scatter on fan or cone collimated beams. For narrow fan beams (1 cm wide in the out-of-plane direction) this estimate would be at the 3-10% level. For broader fan beams or cone beams the contrast degrades rapidly – a fan 10 to 20 cm wide would have scattering approaching the transmitted signal for example. This qualitative picture serves as a guide to interpreting detailed simulations of scattering. Note that the bremsstrahlung spectrum is severely hardened by the thick steel, such that low-energy photons are suppressed. The differences, and scatter contributions, will be larger for lighter objects as demonstrated below.

Simulations of Radiographic Imaging Including Scattering

Scatter contributions were assessed using Monte Carlo simulations in imaging a 5 cm thick lead object obscured by a 20 cm x 20 cm x 20 cm thick steel plate at the center of a container. Two types of narrow-divergence-angle ('pencil') beams used in raster scan mode were evaluated: 3, 6 and 9 MeV MPS beams as well as 6 and 9 MeV Bremsstrahlung beams. These were compared to fan and cone collimated beams to assess the contributions of energy spectrum and collimation to imaging performance. Incoherent scattering is the main photon interaction in the energy range considered here for most materials found in cargos, essentially increasing background in each pixel and lowering contrast. To first order, the cargo scatter contribution reaching the image plane depends on the energy and size of the beam at the object and is generally controlled by collimation. To gauge the effect of scatter on image quality, the contrast between two pixels located behind the steel plate and behind the Pb block respectively was calculated and the contrast C is defined by:

$$C= \phi_2-\phi_1/(\phi_2+\phi_1)$$

where ϕ_1 is the total fluence in a pixel obscured by the steel plate and the lead object, and ϕ_2 is the total fluence in a pixel behind the steel plate.

Preliminary results reported previously [1] showed that under identical narrow divergence beam conditions the contrasts obtained with an MPS and a bremsstrahlung beam of the same energy were comparable, close to 0.9 when penetrating a 20 x 20 x 20 cm^3 steel plate, thus indicating that scatter control through collimation of the beam is key. This is consistent with the beam propagation simulations shown in the previous section. Indeed, narrow-divergence

bremsstrahlung beams are currently known to provide strong benefit in applications where contrast is important and low throughput (due to discarding almost all the photons) is not a concern [4]. An intrinsically narrow angle MPS (e.g. Thomson) could hence provide similar benefit without sacrificing scan rate. Conversely, for a 9 MeV bremsstrahlung cone beam with a relatively small 2.53 degree half-angle in combination with an uncollimated detector, the contrast was found to drop significantly to ~6%. The opening angle was chosen to fully cover the 20 x 20 x 20 cm^3 steel plate. Note that this angle is about $1/10^{th}$ of the angle required to subtend the whole container. This indicates that even modest emission angles can significantly degrade contrast (regardless of source spectrum).

Several factors that might contribute to the dramatic change in contrast depending on beam shape were investigated. First, the 9 MeV bremsstrahlung cone beam described above (2.53 degree half-angle) was simulated in detail, using a spectrum hardened by 1 cm of W. The initial setup had a source 200 cm from the container wall. A vertical linear array made of 220 $CdWO_4$ detectors was located 80 cm from the container exit wall and each element was 1 cm x 1cm x 3 cm. The array was not collimated. Then, parameters were modified in succession including elements of the geometry of the problem, source characteristics and simulation parameters such as the lead cube dimensions, the beam hardness or the photon transport energy cut-off. This allowed systematic evaluation of the factors contributing to image contrast. Results are reported in Figure 6. The thin and thick lines in Figure 6 represent the unscattered and total photon intensities incident on the face of the linear array. The plot exhibits three distinct regions centered around the origin and related to the pixel position with respect to the steel plate and the lead cube. Pixels in the central region are behind the steel and lead. Hence, fewer photons are transmitted and intensities are the lowest. Pixels directly on each side of the central region are behind the steel plate. The contrast between these two regions is the desired performance metric, representing the acuity with which the lead cube can be discerned behind the steel plate. Successive regions further from the axis include pixels in the direct line of sight of the cone beam, which have the highest intensities. Finally, the outer pixels tally scattered photons.

Figure 6 reports the results of successive simulations varying parameters to assess contributions to image quality. The first simulation (black curve) includes a lead cube 5x5x5 cm^3, 2 mm thick container walls and has a photon transport energy cut-off of 200 keV. The second simulation shows the effect of lowering the energy cut off to 10 keV. For this case (blue curve) and the other cases in figure 6 (red and green curves) the geometry of the lead block is similar, at 4x4x5.81 cm^3. Next, the bremsstrahlung spectrum was changed to a non-hardened spectrum lowering the average energy (red curve). None of these parameters affects contrast between the central region (lead) and adjacent pixels greatly. Then, the detector was moved closer, to 30 cm from the container, and the container wall thickness was increased to 5 mm, which increases scattering (green curve). This noticeably degrades performance, as expected. Finally, a vertical fan beam collimation was applied to limit the beam horizontal width to 1.27 cm at the center of the container (0.2 degrees, narrow for a fan beam collimated system). This is plotted in the right panel (yellow line). While overall the unscattered component remains fairly unchanged the total fluence shows a strong dependence on the parameters described here leading to contrast of 0.2 for the initial simulation to 0.06 for the worst-case scenario (green curve, which includes the thicker wall). This indicates that detector position and energy cuts contribute modestly to contrast in this case. The latter is similar to the results presented previously. Container wall thickness is important as it contributes to scattering. Contrast is increased to 0.5 for the fan beam configuration, indicating that source collimation is the dominant control.

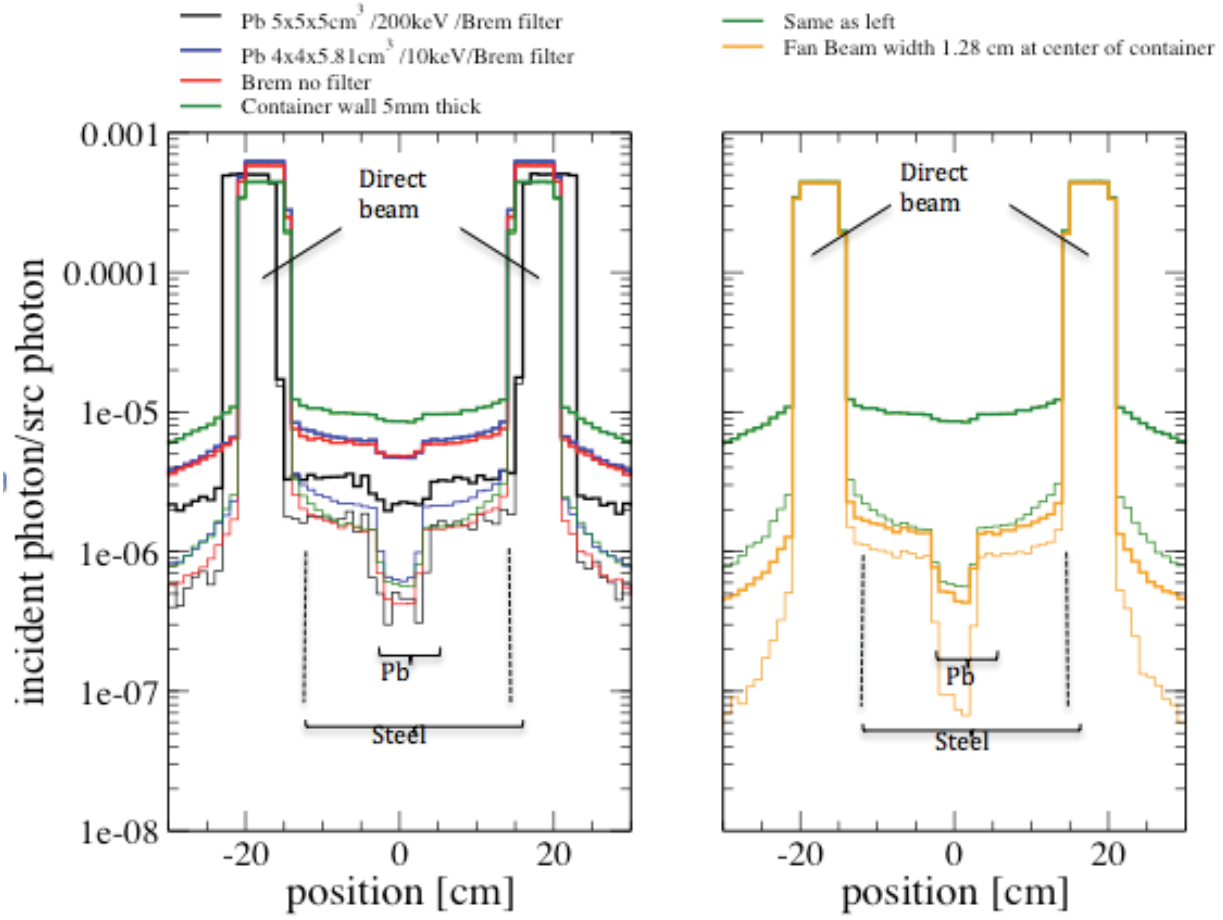

Figure 6. Fluence at the linear detector array for a 9 MeV, 2.5 degree cone beam on a 20x20x20 cm^3 steel plate concealing an approximately 5x5x5 cm^3 Pb cube for no collimation (left) and comparing no collimation to fan beam collimation (right). Thin lines represent unscattered fluence and thick lines total fluence. Non-zero contributions to the unscattered component outside of the beam are due to unscattered secondary particles.

A further set of simulations was conducted to emulate state of the art systems that use a fan bremsstrahlung beam narrowly collimated in the horizontal axis, combined with collimated detectors, to reduce scattering contributions. These were compared to narrow-angle MPS beams. The geometry is shown in figure 7. Simulations for a small 20 cm x 20 cm x 20 cm plate were compared to those for a large steel plate 300 cm wide x 238 cm high x 20 cm thick, each located at the center of a cargo container. The linear array of 220 detectors, 1cm x 1cm x 3cm long, is collimated in the horizontal direction by two tungsten (W) plates extending 30 cm from the front face of the detectors. This detector geometry was chosen to limit any contribution from secondary scatter coming from the sides of the cargo and container. Two configurations were modeled, each for 6 and 9 MeV bremsstrahlung end-points. In the first the source was at a distance of 3.8 m from the container. It had a fan beam vertical opening of 17 degree half-angle to cover the container, and a horizontal opening angle set to achieve a 2 cm width at the center of the container and 4 cm at the detector. The detector was 3.8 m from the container, and container walls were 5 mm. The long separation distance mitigates scatter, but is not representative of many systems in use. The second configuration had the source, whether MPS or Bremsstrahlung, closer to the container at 2 m. The vertical fan angle was increased to 30 degree half-angle to cover the container, and the horizontal beam collimation was reduced to deliver a 1.0 cm beam width at the detector. The detector was 0.8

m from the container and the container walls were 2 mm thick. These source and detector distances are closer to systems in use, although source collimation may be narrower then used in developed systems. [5] In addition to bremsstrahlung beams, 3 and 9 MeV monoenergetic photon sources (energies were chosen for best Z discrimination based on mass attenuation coefficient) were modeled, each having a 2 mrad full divergence or 0.6 cm width at the container center (derived from realistic parameters for a Thomson source). Simulations were run for the MPS and fan beam at the same location. While the MPS location is fixed, the direction of its narrow-divergence beam was scanned to aim at a specific pixel as shown in Figure 7.

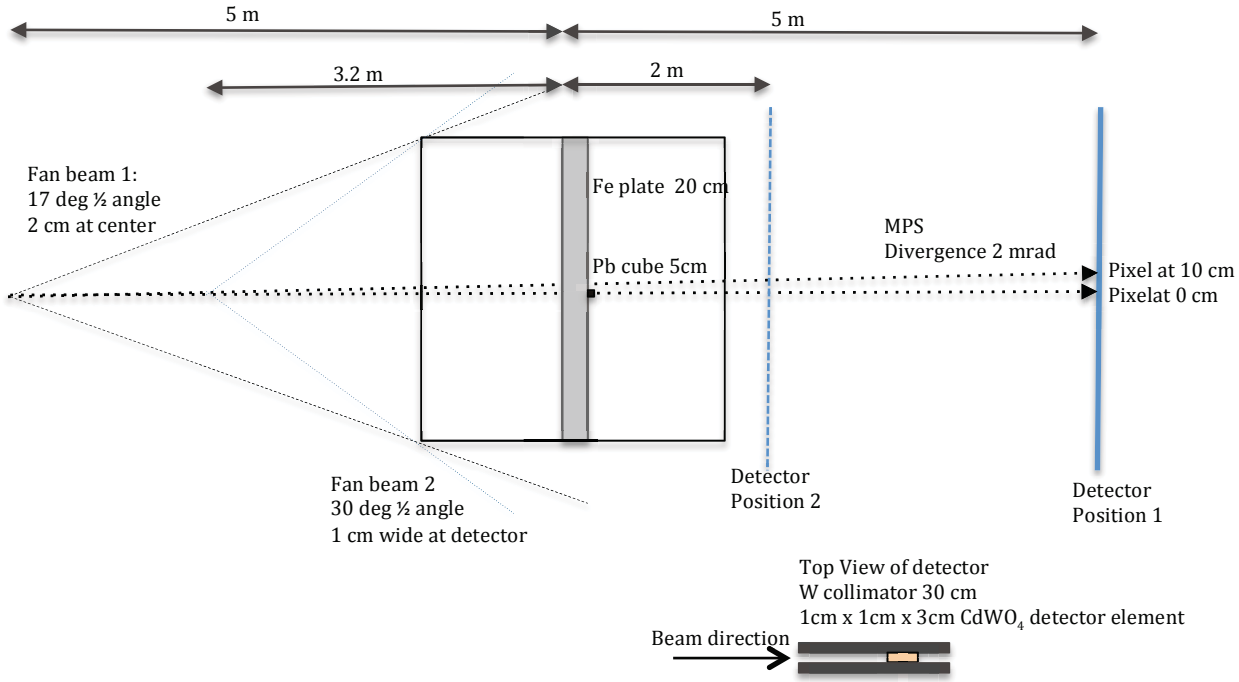

Figure 7. Geometry of the problem: the cargo container. Overall size is 6 m x 2.4 m x 2.4 m. The source is 10 m from the detector in configuration 1, and 5.2 m in configuration 2. A top view of a detector element inside the collimator is shown in the bottom right corner.

Photon fluences incident on the detectors are larger for the small steel plate than for the large one as shown in figure 8. The large steel plate acts as a beam absorber while in the case of the small steel plate a large fraction of the fan beam illuminates the 5 mm steel walls and scatters in the detectors. For the small plate case, the contrast is 0.76. However, when container walls are removed the contrast increases to 0.82, essentially equal to the value of 0.83 obtained for large plate case reported in Table 4. The container walls can be considered as stand-in for other scattering sources in a container. The strong dependence on the container walls indicates that for the fan beam collimated source (MPS or bremsstrahlung), contrast can be sensitively dependent on surrounding material. This effect becomes more severe the wider the collimator angle, as indicated by the 2.5° cone results above. This is not the case for a pencil-beam collimated source, where contrast contributions due to scattering are readily isolated (see figures 3, 4, 5). Finally, in the large plate configuration, the contrast achieved with the MPS and bremsstrahlung beams going through 20 cm steel is high as seen in figure 9. The pencil-beam collimated MPS in this case shows only a small improvement, from 0.83 to 0.88. Bremsstrahlung simulations through 40 cm of steel were prohibitive. However the MPS simulations yielded contrast similar to those observed for the thinner plate albeit with a signal smaller by at least two orders of magnitude.

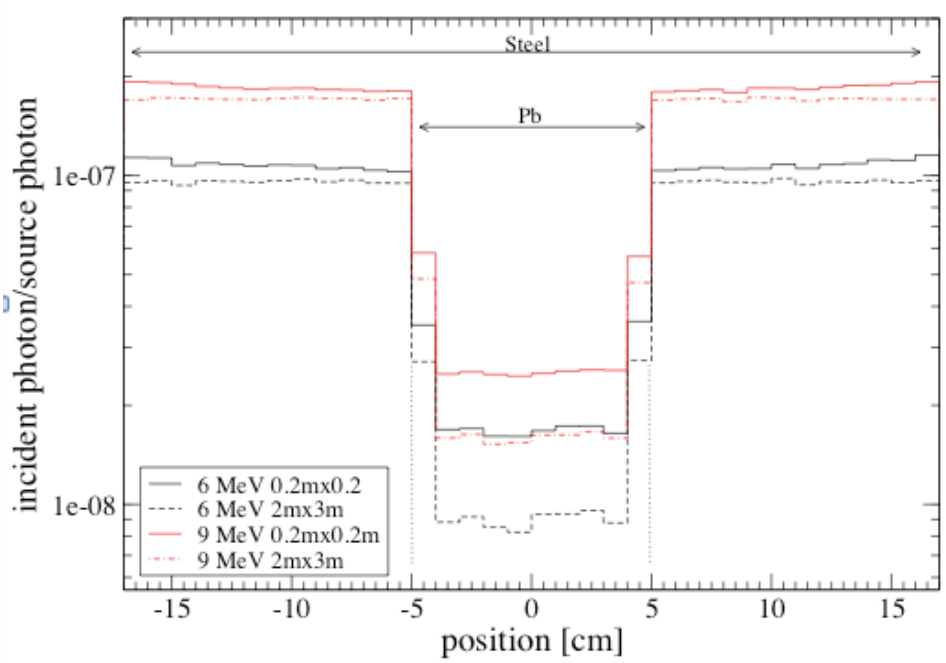

Figure 8. Total photon intensity on the linear array of detectors for 6 MeV (black) and 9 (red) MeV bremsstrahlung beams. The steel plates are 20 cm thick by 20x20 cm^2 (full lines) or 300x238 cm^2 (dotted lines). The cargo central axis is at the origin hence pixels in the center part of the plot are behind 20 cm of steel and 5 cm of lead. The detector is located 5 m from the center of the container and the system has a magnification of 2.

Table 4. Estimated contrast for a source-to-detector distance of 10 m (configuration 1) and 5.2 m (configuration 2). MPS vs. bremsstrahlung beams filtered by 1cm W, incident on a large steel plate and a 5x5x5 cm^3 Pb cube.

	Contrast: 20 cm Fe			
Distance	3 MeV MPS	9 MeV MPS	6 MeV Brems	9 MeV Brems
10m	0.83	0.88	0.83	0.83
5.2m	0.79	0.84	0.81	0.81

	Contrast: 40 cm Fe			
Distance	3 MeV MPS	9 MeV MPS	6 MeV Brems	9 MeV Brems
10m	0.82	0.88	-	-
5.2m	0.80	0.84		

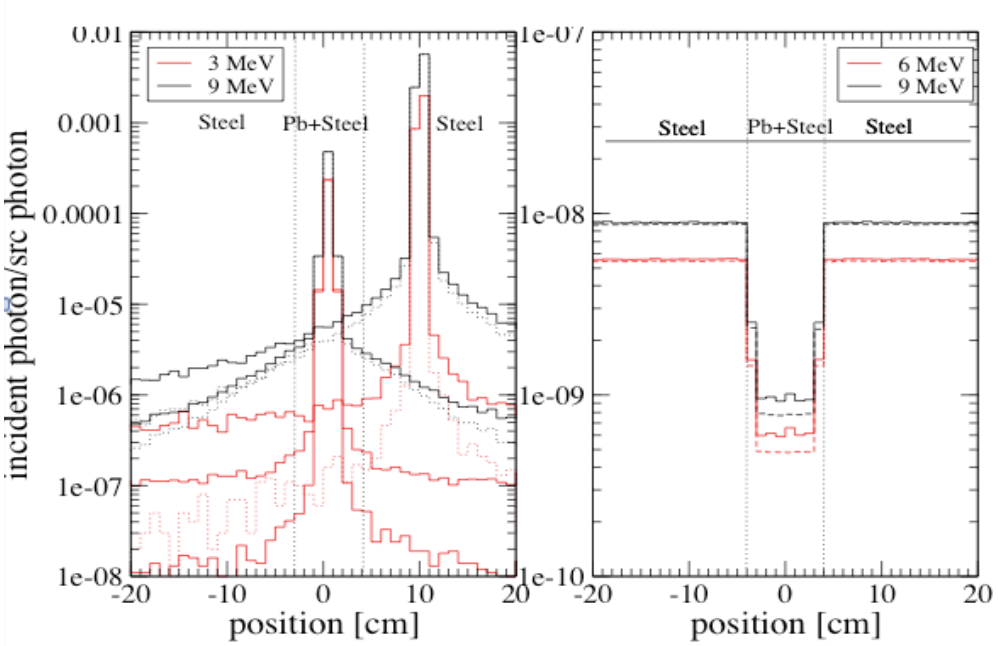

Figure 9. Photon fluence incident on linear array of detectors for 3 and 9 MeV MPS (left) and 6 and 9 MeV bremsstrahlung (right). The beam penetrates through 20 cm of steel at position x=10 cm and 20 cm of steel and 5 cm of lead at position x=20cm. Unscattered (dotted line) and total fluences (thick line) are shown.

In order to further investigate the effect of scattering material surrounding a highly attenuating region, we simulated the imaging of a 5x5x5 cm^3 Pb cube behind a small 20x20x20 cm^3 steel plate with a narrow 9 MeV bremsstrahlung fan beam for the same configuration as described above, only having the container filled with water at a density of 0.2 g/cm^3 [6]. The result is shown in figure 10. The unscattered photon intensity is a factor of ~10 greater behind the steel plate than behind the steel and Pb and the contrast is ~0.83. The total photon intensity on the other hand, and in contrast to the case without water, differs by only a factor of 2 due to scatter in the water surrounding the steel and Pb and the contrast is reduced to ~0.3. Scanning with an MPS pencil beam would eliminate the contribution from scatter in the water and preserve the high contrast. A factor of a few less dose would be required for the same image quality.

These cases underscore the fact that contrast variations for a fan beam are strongly dependent on the configuration of the cargo load as well as the structures and components of the radiographic system surrounding the container that will be in the path of the fan beam, rendering the identification of a high-Z material region difficult if it is embedded behind thick material with a Z similar to steel or surrounded by scattering sources. Both contributions can be greatly reduced by using a narrow divergence MPS since first scatter from the cargo, container and radiographic system does not contribute to the image and second order scatter is not significant. Schematic simulations with a single 20-40 cm thick steel plate indicate that for the configurations without the extra low-Z (water) scatterer, the use of 3 and 9 MeV narrow-angle MPSs only yields a small contrast improvement compared to 6 and 9 MeV narrowly collimated Bremsstrahlung fan beams. However, based on the documented variety of goods being shipped and of cargo loading configurations, during actual cargo imaging at ports of entry, it is expected that the scatter component for a fan beam system can be much larger depending on cargo and support structure configurations thus reducing contrast similar to the scattering effect demonstrated in Figure 10. The simulations show that, as long as transmission is sufficient, a narrow angle MPS (e.g. a Thomson source) is insensitive to this effect, offering a significant advantage for cargo applications.

In cases where scattering is severe, such a source may significantly reduce the dose required to form an image. Other MPS candidates, such as nuclear reaction sources, can be considered to be nearly isotropic in emission. Scenarios with a source illuminating two containers, one on each side of the source, have been proposed. Unlike the narrow angle MPS and fan beam, cargo scatter cannot be reduced by controlling the spatial resolution of the beam in this case. Use of multiple collimators and/or tight collimation of the detectors combined with energy threshold need to be evaluated to help extract information from such an imaging system. Such a technique is being actively investigated and evaluated against existing systems [7].

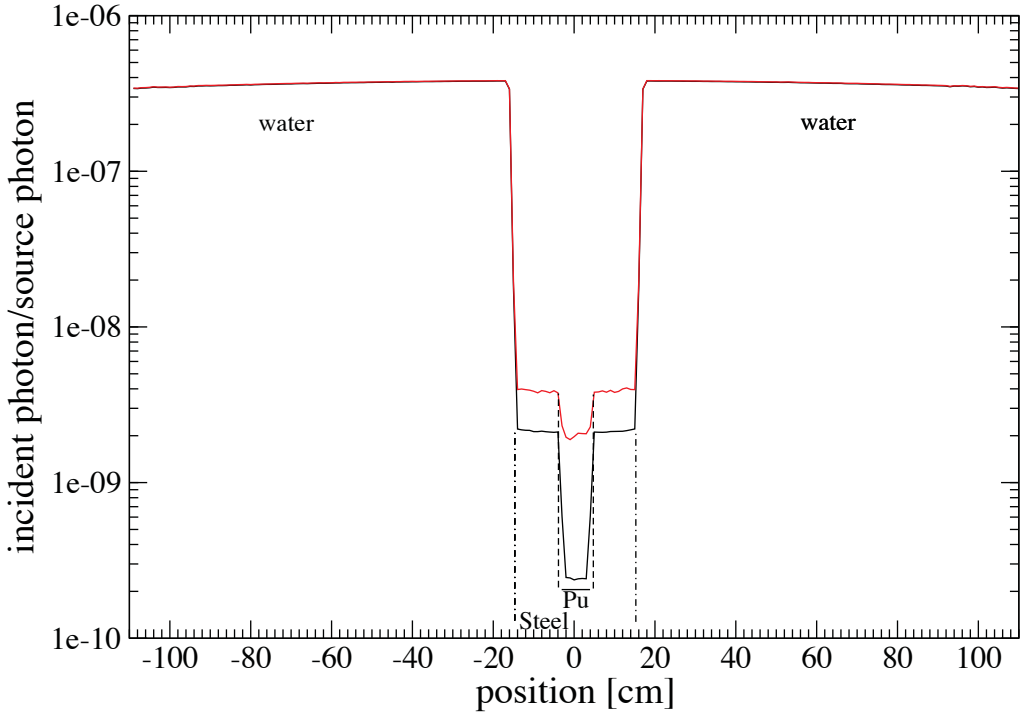

Figure 10. Photon fluence incident on linear array of detectors for a 9 MeV bremsstrahlung source penetrating through a 20 cm x 20 cm x 20 cm steel plate and 5 cm x 5 cm x 5 cm lead cube surrounded by water. The unscattered (black line) and total fluences (red line) are shown. A pencil beam would eliminate the scattering effect, essentially reproducing the black line.

Enhancement of Z Discrimination Using Dual Energies

The ability to isolate high-Z objects - where high Z is often defined as Z>72 - in radiographs of cargos is a key need. This has remained a challenging problem so far. Current systems have to contend with convolution of two broad bremsstrahlung spectra and with scattering due to the fan beam collimation. The CAARS ATD program defined a set of challenging objects for tests of Z discrimination. Tested systems, which did not include MPSs, had high false alarm rates and/or inconsistent automatic detection of high-Z objects possibly caused by scatter in some cases [8]. To investigate the potential benefits for Z discrimination of an MPS dual energy system, and the appropriate energies to use, simulations were conducted using the CAARS objects. Simulations first evaluated effects of photon energy spectrum (neglecting scattering) on Z resolution, and then considered the effects of scattering on Z resolution. Z discrimination was also analyzed in targets consisting of Pb cubes hidden behind steel plates, a geometry that has been commonly used.

The production version of the HADES radiography simulation code [9], which is based solely on photon transmission and does not account for scatter, was used to evaluate Z-discrimination

differences due to photon source spectrum. Images of several CAARS test objects were simulated for two types of parallel beams, MPS beams ranging from 1 to 10 MeV and for 6 and 9 MeV bremsstrahlung beams. Attenuation ratio maps were calculated for energy pairs. Additionally, since HADES does not account for scatter in the object, Monte Carlo simulations were run for one of the objects. The combined simulations illustrate the advantages of dual-energy MPSs for Z discrimination, and the robustness of that advantage to scattering effects.

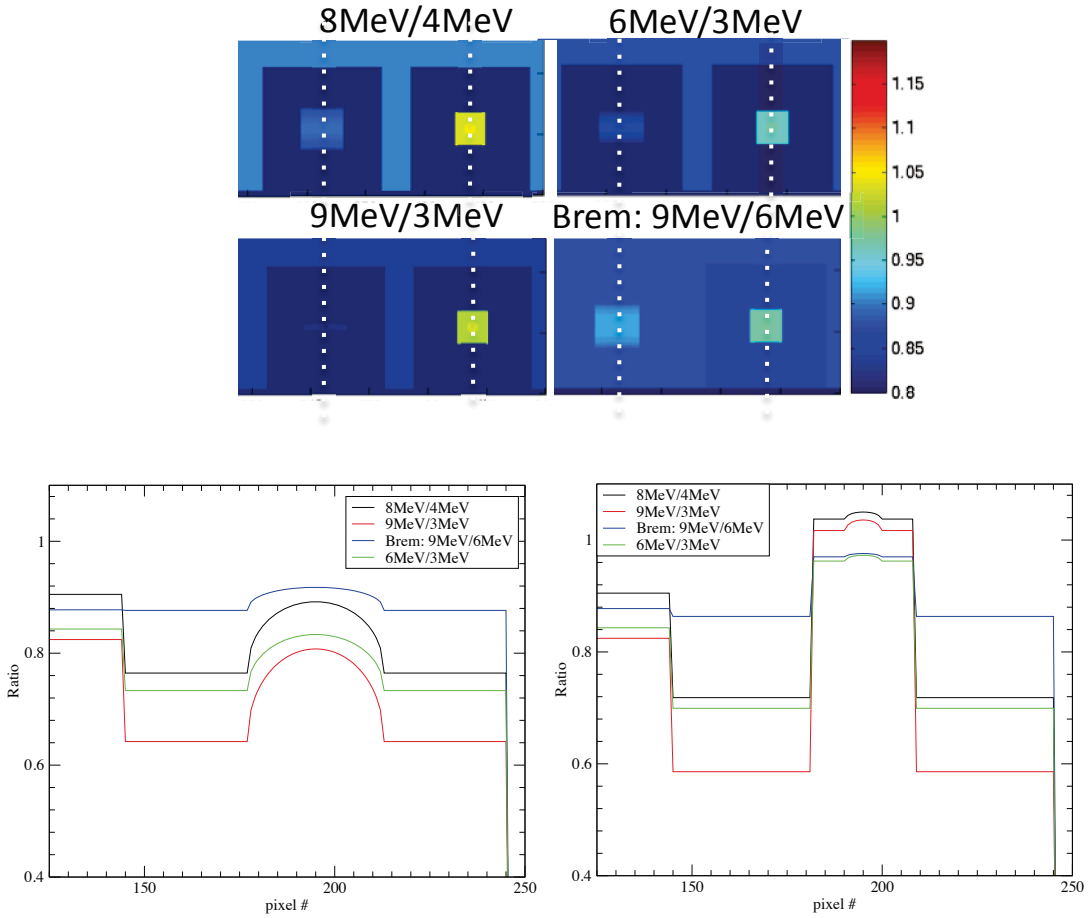

Figure 11. Images of attenuation ratios of MPS and Bremsstrahlung beams through CAARS objects #3 and #4 (top). Images were simulated at each energy with the HADES code. Vertical lineouts through the center of the objects are plotted for object 3 (bottom left) and 4 (bottom right).

Figure 11 shows attenuation ratio maps and vertical lineouts for CAARS objects 3 and 4. Object 3 is made of a yellowcake cylinder inside concrete. Object 4 consists of a 5 cm radius sphere of DU embedded in the center of a cube of lead cube and centered in cube of Lexan placed at the center of a cargo container. The lead and Lexan cubes are 26 cm and 100 cm on the side respectively. The smallest differences were observed for the 9/6 MeV bremsstrahlung ratio. The best overall MPS energy combination for Z discrimination of the CAARS objects was found to be 3 and 9 MeV or 4 and 8 MeV respectively. Notably, the 9/3 MPS lineout of the attenuation ratios shows a ~2% enhancement at the location of the DU sphere whereas there is no appreciable change in signal for the 9/6 bremsstrahlung beams. This demonstrates the greater sensitivity of MPS dual energy imaging. For CAARS Object #3, the relative difference in ratio between the yellow cake and concrete regions for the 9/3MeV MPS is a factor of 5 greater than that for the 9/6MeV Bremsstrahlung. What sensitivity can be achieved in an actual measurement will depend on measurement errors,

systematic errors introduced by the radiographic scanning system and photon counting statistics but it is clear that use of monoenergetic photon beams provides a several-fold increase in contrast to offset such potential issues.

To evaluate the effects of scattering on Z discrimination, Monte Carlo simulations were run for Object 4 in a geometry corresponding to configuration 1 in Figure 7, i.e. the distance between the source and the detector is 10 m resulting in a magnification of 2. This case was chosen to determine if the DU and lead region could be differentiated using either a bremsstrahlung fan beam source or a narrow divergence MPS when scatter was included. The narrow divergence MPS was the case evaluated here (Figure 12) because the scattering simulations above showed that such a source has the best capability to mitigate scatter and hence to potentially address this challenging case.

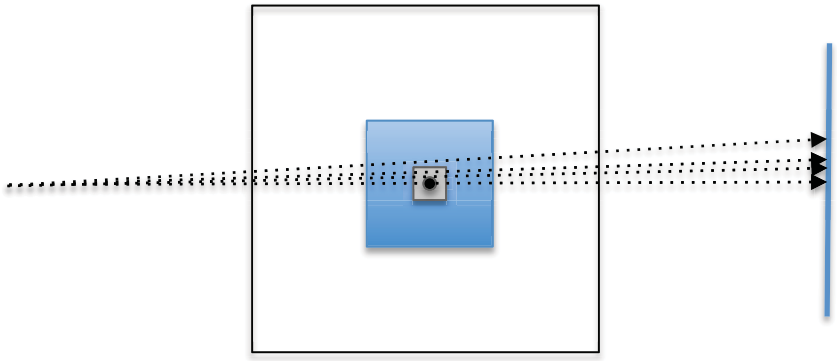

Figure 12. Simulation geometry: the narrow divergence beams are emitted from the same location; each beam is angled to go through a different region of object 4 (blue square).

Both the 6 and 9 MeV bremsstrahlung fan beam simulations show no differentiation between the U+Pb and Pb regions in the center. This is not surprising given that the contrast without scatter was already very small in this region. Scattering in the thick target is significant, causing loss of any signal. The signal does increase by two orders of magnitude in the region behind the Lexan, due to the much higher transmission in this area. The transmitted flux lineouts are plotted in Figure 13.

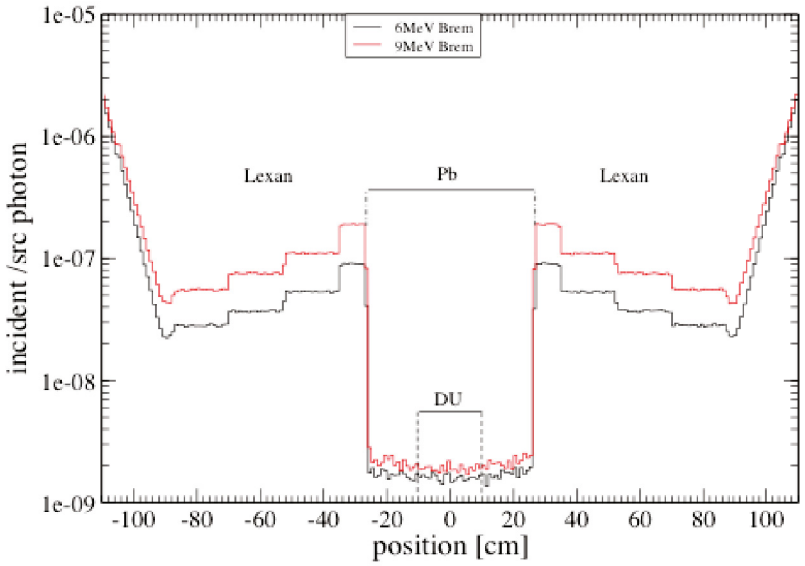

Figure 13. Simulated transmitted intensity including scattering for CAARS Object 4 using 6 and 9 Bremsstrahlung fan beams, as detected on a linear array of 1x1 cm^2 detectors.

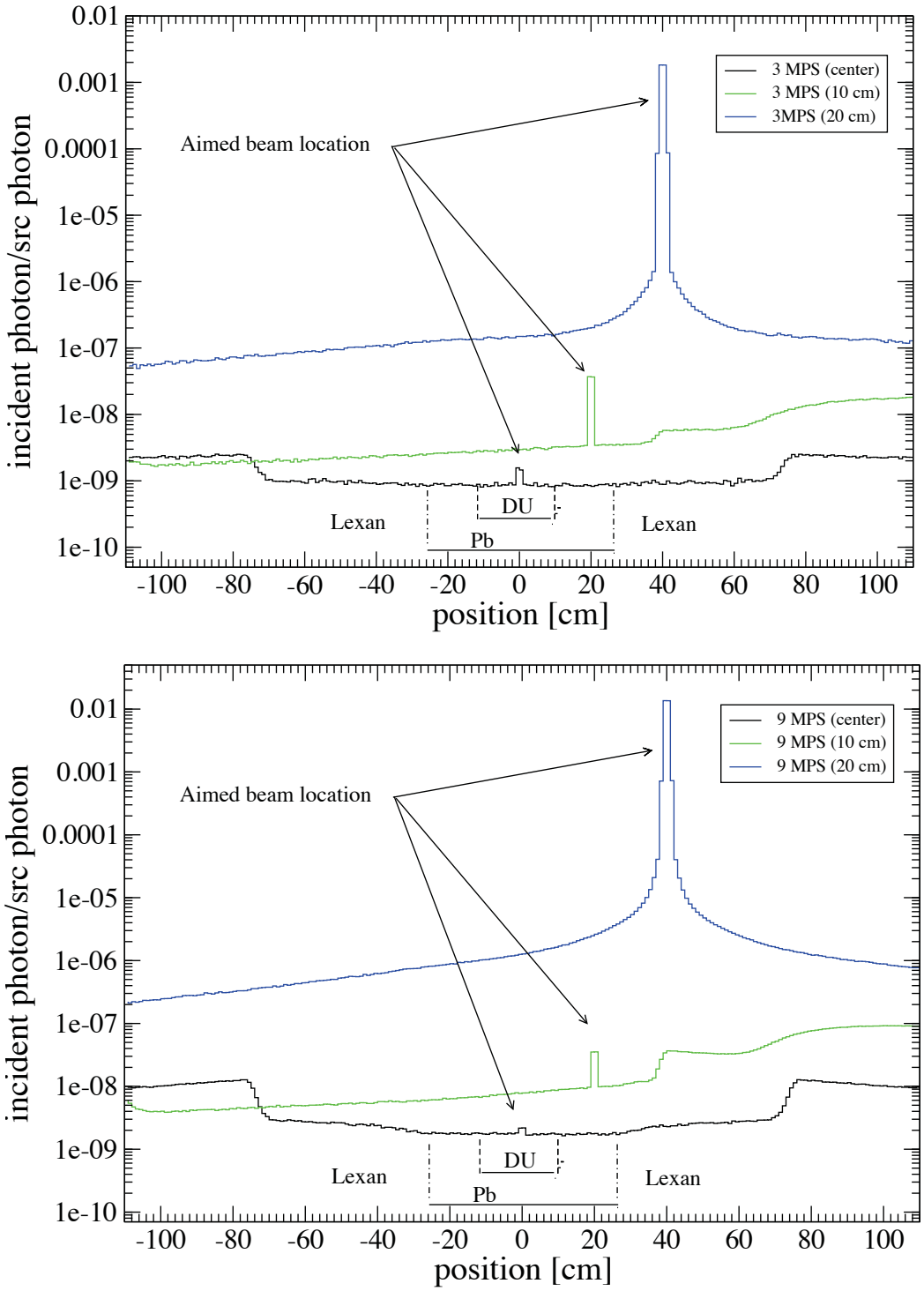

Figure 14. Simulated transmitted intensity including scattering for CAARS Object 4 using 3 MeV MPS (top) and 9 MeV MPS (bottom) beams, as detected on a linear array of 1x1 cm^2 detectors. The MPS is directed at the center of the object (black), at the Pb region (green) and at the low-Z Lexan region (blue).

Simulations were next conducted for 3 and 9 MeV MPSs with narrow divergence pencil beams, as shown in Figure 12. Each line in Figure 14 shows the detected signal for a particular aiming of the pencil beam. The MPS is directed at the center of the object (black), at the Pb region (green) and at the low-Z Lexan region (blue). There is little signal when the beam aims at a pixel located behind the center of the DU sphere since photons are attenuated by 10 cm of DU and 16 cm of Pb (black curve). The green curves correspond to beams going through the edge of the sphere and through the Pb respectively. The blue curve corresponds to the MPS beam aimed at the low Z region made of Lexan. While scattering is severe, a transmitted peak is still visible in all cases. The intensity in the illuminated pixel behind the lead is low, of order of a few $1 \cdot 10^{-8}$ photons/source photon. Assuming the maximum beam intensity of $1 \cdot 10^{8}$ photons per pulse, a signal of a few counts per shot could be generated during each shot. Multiple high intensity shots could be aimed at the same pixel with a kHz repetition rate source to obtain reasonable signal-to-noise ratio. The intensity behind the DU is even lower: at the order of 10^{-9}, and scattering is severe. Many shots would be required to obtain statistics, and further detector collimation is likely important to extract a usable signal. Nonetheless, a difference is clearly visible in this simulation between the lead and DU regions, which was not the case for the fan beam (Figure 13). This indicates the power of a MPS pencil beam to access very challenging targets. The intensity per source photon in a pixel behind the low-Z Lexan is 5 orders of magnitude larger than for the high Z regions. The ability to modulate MPS intensity on a per shot basis would therefore be important allow to limit dose by optimizing the beam intensity on the next pixel based on knowledge of intensities in the neighboring pixels.

A separate study based on absorption cross-sections ratios at low and high energies was conducted based on work by Martz et al., which compared material discrimination contrast obtained with two dual-energy systems. A 3.5 and 9 MeV MPS was compared against a 6 and 9 MeV Bremsstrahlung system, for plates made of low Z or high Z materials hidden behind a 20 cm Fe plate. [4] In that study the plate thicknesses were chosen to provide the same low energy transmission as a plate of 5 mm of uranium. When compared to U cross-section ratios, low-Z contrast for MPS was found to be greater by at least a factor of three compared to Bremsstrahlung beams while W was indistinguishable from U. This is a lower scatter configuration and provides a comparison of Z discrimination in a configuration also used in previous cargo radiography evaluations as discussed in the previous section.

The ability to estimate Z from total transmitted intensities was compared for 3 and 9 MeV MPS pencil beams and for 6 and 9 MeV bremsstrahlung narrow fan beams using the configuration of a Pb cube behind a 20 cm thick steel plate as seen in Figure 7 with the detector in position 2. Transmitted intensities were obtained for two beam paths, either through steel or through steel and lead, and the ratios of the total transmitted intensities were taken for the two beam energies. The resulting ratios are listed in Table 5. Quite strikingly, the ratios for the bremsstrahlung beams are indistinguishable within the statistical uncertainties (~3%) of the simulation whereas the MPS ratios differ by about 30%, indicating an improvement of approximately ten-fold. These results clearly indicate that at least for the case studied the sensitivity to Z is rather weak for a 9/6MeV bremsstrahlung system and that even in a low scatter case Z discrimination is unlikely to be achievable given statistical and systematic uncertainties. Dual energy MPS ratios on the other hand are sensitive to Z. In addition, scatter degradation is not significant when using pencil beams.

Table 5. Ratio of total counts for MPS and bremsstrahlung beams hardened with 1 cm of W through 20 cm of steel and 5 cm of lead. Statistical uncertainties for the bremsstrahlung results are ~3%.

Beam & Energy ratio	Steel	Steel+Pb
Brems 9MeV/6MeV	1.57	1.61
MPS 9MeV/3MeV	2.87	2.04

As discussed in our previous report [1] for monoenergetic beams and relatively simple geometries such as the one used in the simulations described here, a Pb cube behind a thick steel plate, the mass attenuation coefficients μ at the two energies, which are used for Z-determination, can be calculated from measured transmission (I/I_0) ratios in a straightforward manner. No a priori knowledge of the Z, density or thickness of the materials is needed. While this may be helpful in threat detection in some situations, it may require additional information to exploit in cases of irregular shapes and more cluttered cargo.

An alternative Z-discrimination and 3D imaging method, called EZ-3D, has been developed by Passport systems. [10] This secondary bremsstrahlung-based imaging method is based on scanning with a narrow beam and gaining spatial information by measuring photons at 130° to the beam axis with an array of collimated NaI detectors. Compared to transmission imaging using the dual energy method that relies on a 2D projection of a 3D object, EZ-3D has two advantages. First, it is a 3D measurement where voxelization of the cargo is set by the beam collimation and by the orientation and field of view of the detector array with respect to the beam. Second, it has a much stronger Z-dependence of $\sim Z^{3.5}$ than the dual energy method. Replacing the rhodotron generated bremsstrahlung beam with a narrower, higher average photon energy MPS pencil beam could potentially significantly increase the EZ-3D performance. EZ-3D requires photon energy discrimination to determine the ratio of total photon flux to the flux of photons with energies above 511 keV. However, a detection system with energy resolving detectors such as Passport's would not be suitable for a Thomson source (which is the known MPS capable of generating the required narrow divergence photon beam) because the photons are delivered in a short pulse. A Cherenkov detector with a threshold just above 511 keV could be a possible solution. If such detector with good detection efficiency could be developed, EZ-3D would be an even more powerful approach than dual energy for Z-discrimination using an MPS.

The simulations conducted confirm the expectation that significantly better Z-discrimination can be achieved with a narrow energy spread beam, measuring transmission at several well defined energies, than with a bremsstrahlung beam that integrates transmission over the full energy range and may experience spectral change (beam hardening) when traversing the cargo. Narrow energy distribution, narrow beam divergence MPSs with the ability to select and rapidly switch energy over the full range of 1–10 MeV could potentially enable the development of improved systems. This capability is a characteristic of MPSs based on Thomson scattering. Energy switching could be important for Z-determination using the dual energy method. Resolving object overlap in highly cluttered cargos may further require at least two views or and EZ3D-type method, which is not addressed in detail here.

Raster Scanning and Dose Adaptation

Existing broad energy-spread sources have cone beam emission geometry and require collimation to generate a fan beam used for one-dimensional scanning along the length of a container. The same methodology would be appropriate for nuclear reaction based MPSs. The small

beam size and narrow divergence of Thomson sources preclude the fan beam approach but these sources are ideal for raster scanning, assuming scan times below acceptable limits can be achieved.

Raster scanning provides two important advantages: it can improve image quality as discussed above by reducing scattering contributions, and it enables 2D dose adaptation for each resolution element if the number of photons per shot can be controlled on a shot by shot basis. A simple scheme for dose adaptation across a cargo container may be to deliver one initial low-dose shot and then to follow it up with one or two shots at higher intensities. A faster technique may be to control the dose to the next pixel based on the knowledge of the transmitted signal for the previous pixel. As the raster scan proceeds to build up the image more spatial information may become available for better estimating the numbers of photons needed for the next pixel. Sharp changes in intensity value from low Z to high Z pixels may require more than one shot.

For raster scanning with a narrow divergence photon beam, the dimensions of the container combined with the required scanning speed and achievable beam sizes define the repetition rate. The goal of scanning a container in 30 s is certainly ambitious but could be done in principle, with a ~1 cm^2 beam and 1 shot/location at 10 kHz. For dose modulation and dual energy measurement 2 or 3 shots per location may be required. Assuming a 1 cm beam diameter and a 20 kHz repetition rate, a 40 ft container could be scanned in one minute. By taking advantage of spot by spot dose modulation, an additional several-fold dose reduction could result from scanning the container with a pencil beam. Shorter scanning times or operation at lower repetition rates would be possible with larger beam diameters or adaptive beam diameters, using larger beams where highest spatial resolution or scatter rejection is not needed.

II.1.4 Impact on Screening Radiography and MPS Requirements

Significant potential benefit was indicated for radiography applications using monoenergetic photon beams at energies ranging from 3-9 MeV, and with typical fluxes in the range of 10^{10} photons per second for initial capabilities to 10^{12} photons per second for high performance applications. Pulsed sources should have repetition rates in the kHz range to enable initial capabilities (corresponding to 10^7 to 10^8 photons per shot), while repetition rates in the 10-50 kHz range would enable high performance.

Several MPS capabilities are important, each of which delivers benefits, which compound. For the configurations evaluated, replacing bremsstrahlung with a monoenergetic source having similar emission angle and pulse structure enables reductions in radiography dose by factors of 3-4x due to the narrow energy spectrum alone. All comparisons reported here assume that the MPS or bremsstrahlung source itself is well-shielded and does not contribute to the dose. Contrast in Z is also increased by several-fold for the assessed configurations by use of dual-energy MPS ratios. This can enable effective discrimination in cases that are not currently accessible, and/or reduce the dose required to achieve discrimination in cases that are currently accessible by several-fold. Sources that produce beams with small divergence in particular could be of great value to cargo imaging applications by producing a small diameter beam at the target, (i.e., a pencil beam of ~cm diameter, corresponding to few mrad source divergence). This configuration mitigates contrast degradation due to scatter and hence reduces the required dose. The additional reduction in dose, both to stowaway and in scatter dose from cargo to surroundings could be a factor of a few on top of the reduction due to the monoenergetic energy spectrum depending on cargo and system design. Small divergence is more effective in mitigating scattering than control of the photon energy spread. Hence MPSs with narrower angle emission than bremsstrahlung fans will provide strongest advantage. Correspondingly MPS systems with broader emission angles than bremsstrahlung fans may not improve dose or image quality in cases where scattering is strong. By taking advantage of

spot by spot dose modulation, an additional several-fold dose reduction could result from scanning the container with a pencil beam. In contrast to scanning with a fan beam, the dose to empty or weakly attenuating regions above and below highly attenuating material could in many cases be reduced by at least an order of magnitude. In pencil beam scanning the spatial resolution can be defined by the beam diameter and not by the size of the detector element. Hence the pencil beam also removes effects of scattering within the detector, which is often significant [5], further compounding the contrast advantage and dose reduction to be obtained. This also raises the possibility that the imaging detector could be much simpler with larger, higher detection efficiency elements, which could further reduce dose. In-detector scatter would not be an issue as signals from neighboring elements could be added. Evaluation of this effect was beyond the scope of the current study. The divergence requirement for use of a pencil beam is set by the desired scanning resolution, since the beam divergence and the source-to-cargo distance define beam size at the container wall. For container radiography applications, a beam size of 1 cm at the container wall can be achieved at a distance of 5 m with a beam divergence of 2 mrad, or at 2.5 m using 4 mrad. Using bremsstrahlung or nuclear reaction sources, such collimator angles would discard almost all of the available photons. Thomson sources, on the other hand, intrinsically generate beams with ~mrad divergence at energies of a few MeV and energy spreads of 10-30%. Combining the effects of monoenergetic transmission, increased Z contrast, scattering mitigation, and dose adaptation, such a source could enable superior resolution combined with typical dose reductions of one to two orders of magnitude (target and configuration dependent). Conversely, the importance of scattering in determining dose indicates that the utility of sources producing collimated divergence greater than current fan-beam collimated bremsstrahlung sources may be limited even if the source is monoenergetic.

II.1.5 Alarm Resolution and SNM Identification

If a dense high-Z object has been found and localized in a radiographic scan and determined to be suspicious, the object or location may need to be inspected in a secondary scan to either determine with high confidence that SNM is not present and to clear the alarm or to confirm the presence of nuclear materials. Active interrogation methods have been developed for this purpose including photofission and NRF. Secondary screening for SNM typically uses photofission, and use of energies below 10 MeV is a priority. Initial calculations indicated that dose required to detect fissile material could be reduced by more than a factor of 10 because the entire MPS beam overlaps the photofission resonance yielding much more efficient excitation compared to bremsstrahlung sources at ~10 MeV energies (where only a small fraction of photons are useful). Beyond photofission highly specific NRF measurements are enabled at MPS energy spreads ≤2%. NRF measurement times and doses could be lower by orders of magnitude compared to a bremsstrahlung source. In this report, photofission simulations are discussed in detail in section II.2, 'Detection of Hidden SNM', and NRF simulations are discussed in detail in section II.3, 'Treaty/Dismantlement Verification'. Here, we apply the detailed results of those sections to assess their potential for alarm resolution and SNM identification (i.e. secondary or final screening) in cargo applications.

Photofission Simulation Results

Active interrogation to induce detectable photofission signatures has been extensively studied as discussed in the initial report [1]. Specifically, Passport Systems Inc. has recently demonstrated using a bremsstrahlung source that in cargo screening prompt photofission neutrons are a strong indicator of fissionable material [10]. Passport's cargo screening system uses prompt neutron monitoring during the primary scan. In the analysis presented here we compare MPS use to

conventional bremsstrahlung sources, assuming that in cargo screening the maximum photon energy is limited to less than 10 MeV to comply with regulations for cargo radiation exposures. A monoenergetic photon source is attractive in this scenario because in contrast to a bremsstrahlung source all MPS photons have an energy well above the fission threshold resulting in much higher photofission efficiency.

To quantify MPS benefits for photofission screening, a test configuration was analyzed consisting of an HEU cube with a side length of 4.6 cm (i.e. close to 100 cm^3 in volume and 2 kg in weight) positioned in the center of a cube with either 10, 20 cm or 30 cm thick steel walls which in turn was centered inside a cargo container. The photon source (i.e., the beam starting location) was 1.25 m from the outer wall of the container. Fission rates were calculated with MCNP for a 9 MeV MPS and for a bremsstrahlung source with a 9 MeV endpoint energy and a 1 cm W beam-hardening filter. For this comparison both beams were collimated to an angular divergence of 3.5 mrad so that all photons would hit the HEU target. The fission rates per source photon are listed in Table 6 for steel wall thicknesses of 20 cm and 30 cm. The number of fissions per source photon is ~160x higher for the MPS than the bremsstrahlung source due to a combination of less attenuation in the steel and higher photofission cross sections.

Table 6. Fission rates in 2 kg HEU in steel boxes for MPS and bremsstrahlung beams.

Wall thickness of steel box	20 cm	30 cm
MPS 9 MeV	$5.18\ 10^{-5}$	$5.05\ 10^{-6}$
Bremsstrahlung 9 MeV, 1 cm W filter	$3.19\ 10^{-7}$	$3.07\ 10^{-8}$
Fission-rate ratio MPS/bremsstrahlung	162	165

For comparing the dose per fission imparted by the beams to an object in its path, one must take into account the different dose per photon for both beams. As seen in Table 3 the dose per photon to a water cylinder is 3.09x higher for the MPS than for the bremsstrahlung source, reflecting the higher average energy of the MPS photons. Thus, for the simulated cases, the MPS delivers a factor of 53 lower dose per fission than the bremsstrahlung beam. Such dose reduction would significantly benefit the use of photofission in the field.

Detailed simulations of photofission signal rates are described in section II.2 'Detection of Hidden SNM'. For energies below 10 MeV, the prompt neutron signature is strongest. The results can be extrapolated to the case considered here as the configuration is similar, i.e., the same shielding thicknesses of 20 cm and 30 cm of steel. Although the HEU masses considered are very different, in both cases (the 2 kg HEU cube and the larger cylinder used as configuration 'A' in section II.2), the full photon beam intersects with the HEU object. For use of the prompt neutron signal the maximum allowed photon energy was set at 10 MeV to avoid potential signature interference for single sided inspection (see section II.2), and the same limit applies to cargo container screening. A 9 MeV MPS beam with a 10% energy spread would be suitable. For the geometry and beam parameters given in II.2, the prompt neutron count rate was calculated to be ~0.033 counts per beam pulse ($6.9x10^8$ photons/pulse) for the 20 cm steel wall case. This result can be extrapolated to the cargo inspection case considered here. The case considered here has a 10x shorter HEU to detector distance (2 m) and a 4x reduced detector area (1 m^2 instead of 4 m^2), and hence the prompt neutron rate is increased 25x. Correcting the fission rate for the differences in the beam energy spectrum (9 MeV with 10% energy spread vs. 6.7 MeV with 40% energy spread) and assuming $1x10^8$ ph/pulse decreases the number of prompt neutrons by a factor of 1.7. Applying these factors yields a prompt neutron rate of 0.5 cnts/pulse in the cargo screening case for 2 kg of HEU inside a steel cube with 20 cm thick walls. In a primary cargo scan with the parameters

derived in the radiography section above, a 1 cm diameter beam and a single pulse per spot (~1 cm^2), the HEU cube would be hit by ~20 pulses and 10 neutrons would be detected on average. While this is close to the statistical limit of detectability, even a few neutrons would likely cause an alarm because the neutron background from cosmic radiation is negligible during the short prompt neutron collection time, on the order of 1 us after each pulse. Increasing the detector area to a few m^2 would increase statistics. This indicates that even during radiography scans with a MPS, SNM could be detected via photofission. Material presence or absence could then be easily confirmed by dwelling on the spot for, say, 1000 beam pulses. For a steel wall thickness of 10 cm, the prompt neutron rate would be ~80 cnts/pulse or 1600 for a scan and the HEU easily detected. For a steel wall thickness of 30 cm the prompt neutron rate would be ~0.02 cnts/pulse and several thousand pulses, i.e., a measurement time of several seconds at a 1 kHz repetition rate would be needed for detection. As indicated in section II.2, composite shielding (e.g. B-poly and lead) of similar thickness can be penetrated using similar beam parameters.

The delayed gamma or neutron signals are generally weaker than the prompt neutron signal. The delayed gamma signature can be detected by pulsing the source on a macro scale, e.g., 0.5 s on and 0.5 s off, as described in section II.2. The detected net delayed gamma yields of section II.2 can be extrapolated to the cargo screening case (2 kg HEU inside steel box with 20 cm thick walls) considered here. Assuming a 9 MeV MPS beam, $1x10^8$ ph/pulse, 1 kHz repetition rate, and a total detector size of 1 m^2 at 2 m distance, it would take ~1 minute to exceed the critical decision level, which is much longer than for the prompt neutron signature. However, for very thick hydrogenous cargo with high neutron attenuation the delayed gamma signal may exceed the prompt neutron counts and be the preferred signature.

A Thomson scattering source is particularly well suited for resolving an alarm caused by an object in an identified location because the low-divergence beam produces a high photon flux over a small area. In the analyzed example, a Thomson source operating at 9 MeV and delivering $1 \cdot 10^8$ photons/shot at a 1 kHz repetition rate would generate, when interrogating 2 kg of HEU behind 20 cm of steel, 500 prompt neutrons and 20 gamma-rays per 1 m^2 detector area per second. This would enable detection with a high probability within a short interrogation time. Using higher repetition rate and/or longer inspection times, 2 kg of HEU could be detectable behind more than 30 cm of steel. Fissionable materials could be distinguished from fissile materials in several ways after an alarm has been triggered: passive gamma/neutron spectroscopy, differences in the time dependence of the delayed gamma emission, and possibly polarized photofission. Detection of the HEU via photofission could also be done with gammas from a nuclear reaction based source. Because such source emit into 4π, a high source intensity is required for inducing a sufficient number of fissions. An order of magnitude estimate for the case described above indicates that $>10^{12}$ γ/s would be required for a ~10 min detection time.

Nuclear Resonance Fluorescence Simulation Results

NRF has been extensively studied and long been advocated for use in cargo screening because of its unique capability to identify specific isotopes and measure isotopic content. This specificity can potentially be utilized to detect and identify SNM, explosives and other contraband (see [1] and references therein). In the context of cargo screening, NRF is now seen as especially attractive for measuring the concentrations of light elements such as carbon and oxygen to provide cargo-screening systems with additional capabilities for detecting and identifying contraband. An advantage of NRF over fission based approaches for SNM detection is the method's ability to distinguish fissile material from fissionable material, and for isotopic assay. In the assessment of NRF for cargo screening we considered NRF only for SNM detection because contraband detection is outside the scope of the study. However, the scaling between bremsstrahlung and MPS performance is likely to be similar in both cases.

The main challenges of NRF are generally low NRF count rates, due to small integrated resonance cross sections, and often a high background from scattered photons. Measurements with a bremsstrahlung source suffer from its broad energy spectrum. Only a small fraction of the photons are at resonance energy and contribute to the signal while all others contribute to the background in the spectra and increase the radiation dose to the cargo. MPSs offer dramatic advantages for NRF measurements (see [1] and references therein). A key beam parameter for NRF is the spectral density, i.e., the number of photons per unit energy and time, at the resonance energy. For example, a Thomson scattering source generating $2 \cdot 10^7$ ph/pulse with a 2% energy spread and operating at a 10 kHz repetition rate could provide a spectral density of $5 \cdot 10^6$ ph/eV/second, which is roughly a factor of 100 higher than that of Passport's bremsstrahlung source, operating with an end point energy of 3 MeV, and a 2.5 mA beam current. The higher NRF count rate in combination with a dramatically reduced scatter background can be expected to result in a greatly enhanced detection sensitivity together with orders of magnitude reduction in dose to the cargo [11].

For an initial estimate of the detection capability of an MPS-based NRF system, a simple test case was modeled using the MCNP radiation transport code. A small, 2 cm radius, 650 g HEU sphere is located in the center of a cargo container (2.4 m x 2.4 m cross section, 4 mm thick steel walls) that is filled with water at an average density of 0.6 g/cm^3. The MPS is assumed to deliver $3 \cdot 10^7$ ph/pulse with a beam divergence of 0.2 mrad onto the HEU sphere. Two different energy spread values, 2% and 0.2%, were considered. Calculated were the measurement times needed to achieve a 6-sigma confidence for the detection of the HEU sphere for various configurations and beam parameters. The values in Table 7 assume the use of 24 HPGe detectors or a calorimetric detector around the witness foil, and operation at 1 kHz repetition rate.

When using HPGe detectors the measurement times scale as expected with the spectral density of the beam which accounts for the ~10-fold increase with $\Delta E/E$ increasing from 0.2% to 2%. Identification of this small test object is possible in 5 minutes at 2% energy spread and in 30 seconds at 0.2% energy spread. The time needed for the transmission measurement with the calorimetric detector increases with the square of the energy spread because the signal to noise ratio decreases in addition to the NRF count rate with reduction in spectral density, thus a calorimetric detector requires a small energy spread on the order of 0.2% or less. The NRF count rate scales with the MPS repetition rate so that for a 10 kHz rate the measurement times are one tenth of those given in Table 7.

Table 7: Measurement times for reaching 6-sigma confidence for detecting a 650 g HEU sphere when operating at 1 kHz repetition rate.

Measurement Method	Energy spread ($\Delta E/E$) FWHM (%)	Measurement Time
Backscatter 24 HPGe detectors	0.2%	100 sec
	2%	17 min
Transmission 24 HPGe detectors	0.2%	30 sec
	2%	5 min
Transmission Calorimetric detector	0.2%	30 sec
	2%	55 min

A second set of simulations was performed to assess NRF for the 2 kg HEU (93% U-235) object (cube with side length of 4.6 cm, density of 18.6 g/cm3) used in the assessments of cargo radiography and photofission. As shown Figure 15, the HEU is centered inside a steel box with 20 cm inside wall length and 10 cm thick walls. The steel box itself is centered within a cargo container modeled as a box with 5 mm thick Fe walls and 240 cm side length. Simulated were both

backscatter and transmission measurements. The backscatter detector is located 145 cm from the center of the cargo at an angle of 164 degrees relative to the beam centroid direction. For the transmission measurement the U-235 Witness Foil, or WF (also known as scatter target) is 1 cm thick and 2 cm in diameter and positioned 330 cm down-beam from the backend of the cargo container. This distance is unimportant as long as the WF diameter is larger than the beam diameter. The transmission detector is positioned 100 cm from the WF at an angle of 135 degrees relative to the beam centroid direction.

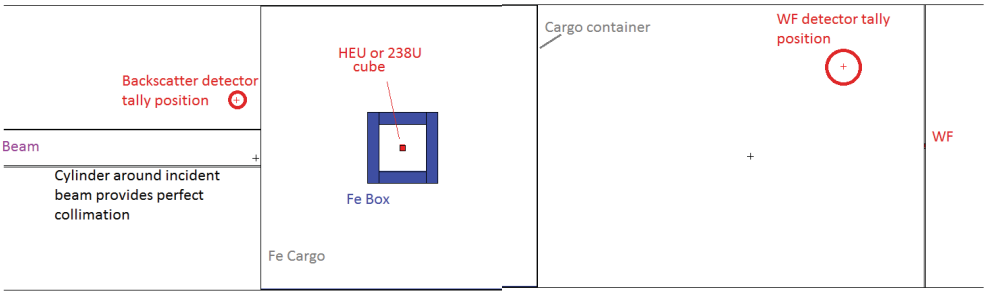

Figure 15. Simulated setup for determining NRF signal rates and measurement times. The backscatter detector is located 145 cm from the center of the cargo at an angle of 164 degrees with respect to the beam axis and perfectly shielded from scatter from the container wall. For the transmission measurement the scatter target is positioned 330 cm down-beam from the back end of the Cargo container. The transmission detector is positioned 100 cm from the scatter target at an angle of 135° relative to the beam axis.

Simulations were conducted for Resonant (Res) and Non-Resonant (NR) photons separately for determining signal and background rates using a beam with an 8 eV energy spread, the width of the Doppler-broadened resonance, centered on the U-235 resonance at 1.7336 MeV. In the resonant simulation, NRF and other forms of scattered photons were tallied at the transmission detector and the backscatter detector positions. In the non-resonant simulations, photonuclear physics were turned off to provide the elastic scatter background for the NRF signal-to-noise ratio calculation and the flux due to the non-resonant component of source photon scattering. In the third simulation the HEU target in the cargo container was replaced with pure U-238, which has identical attenuation properties for non-resonant photons but the simulation allows the scatter target in the transmission setup to undergo NRF. An integrated cross section of 36 eV·b [12] was used in the simulations for the U-235 NRF resonance; it should be noted that in a second experiment Wang et al. measured 22 eV ·b [13]. The results presented here would need to be scaled to apply the lower value.

Detector response simulations were performed separately. It is assumed that the photon flux is spatially uniform over the front surface of the detector (area 60 cm^2). Simulations of energy deposition probabilities were conducted for an unshielded HPGe detector, and for the same detector positioned behind low energy photon filters of 0.5, 0.75 and 1.0 inches of Pb to reduce undesired low-energy photons. Detector full energy deposition probabilities are used to convert MCNP flux tallies to full-energy counting probabilities. Energy-dependent incident detector flux tally spectra are convolved with the detector response to ascertain total count rate expectations.

The resonant and non-resonant simulation results are combined to determine expected system performances for beams with 1.5 and 15 keV rms wide energy spreads corresponding to 0.2% and 2% ΔE/E FWHM. [14]. The method assumes that the photon physics does not change over this energy range and is the same as that of the non-resonant 8 eV wide beam, so that the proportions of non-resonance and resonance photons can be scaled by the relative fraction of each within the beam distribution and convolved with detector responses. This directly gives a total-spectrum count rate. The NRF-signal strength relative to background is established by comparing the scaled

NRF strength to the elastic (coherent) scatter strength produced in the non-resonant simulations across the energy resolution of the detector system (assumed here to be 3 keV for HPGe detectors). Calculated flux distributions to which detector response functions were applied are indicated in Figure 16 for the resonant simulation (blue), the non-resonant simulation (red), and two modifications of the non-resonant simulation. In the case of a 0.2% ΔE/E beam, the non-resonant flux (red) was just scaled by the fraction of a Gaussian distribution that is within ±4 eV of the centroid, which is shown as cyan. Lastly, to represent the non-resonant flux due to a 2% ΔE/E beam, the down-scattered portion of the simulated flux was scaled, while the simulated elastic scatter flux was additionally distributed across a profile representative of the beam, as shown in black. These simulations were conducted with 5 keV energy spacing, which somewhat under-predicts the intensity of the NRF peak, relative to HPGe detector resolution. It can be seen that the resonant signal is visible above the nonresonant signal in both cases.

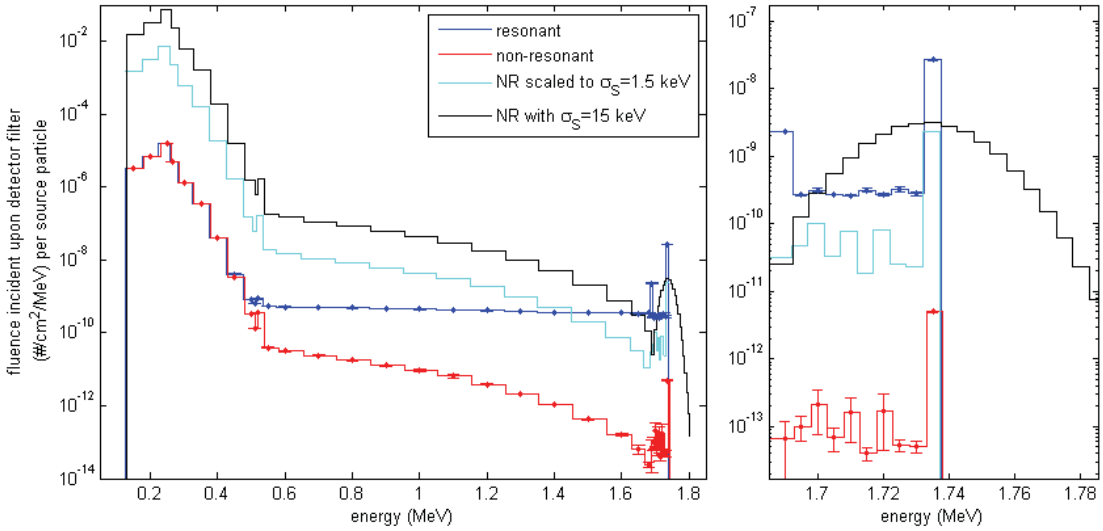

Figure 16. (on left) Simulated spectra incident upon the backscatter detector for the configuration indicated in Figure 15. The resonant (blue) and non-resonant (red) spectra are directly obtained from MCNP simulations of photon sources with widths of 8 eV incident upon a HEU target inside shielding and a cargo container with and without NRF physics, respectively. The simulation's statistical errors are indicated, although often smaller than the widths of the lines. The non-resonant scatter produces background for the NRF peak, and these effects are approximated for the 0.2% and 2.0% beams as cyan and black, respectively. (on right) Same data, zoomed in on the beam-energy region.

The backscatter geometry NRF count probability, total count probability and the signal-to-noise ratio are listed in Table 8 for 1.5 and 15 keV rms width beams and for HPGe detectors behind 0.5, 0.75 and 1 inch of Pb. For the 0.5" Pb filter, the count rate was high enough that it is the limiting factor so that the beam intensity per shot (source photons per shot) was reduced from the nominal maximum of $3x10^7$. The estimated time to make a measurement to confirm presence or absence of U-235 at a level of 6 sigma is based on the number of needed NRF counts for a given signal-to-background ratio ξ, which is calculated as 36/sqrt(1+2/ξ), i.e., for large ξ, 36 NRF counts correspond to a 6-sigma measurement. The shortest measurement times in Table 8 were obtained for the 0.75" filter cases. For the cases considered the measurement times scale with the energy spread of the beam. The times given Table 8 are for a single HPGe detector and a 1 kHz source repetition rate. Assuming the use of 24 detectors as in Table 7 and a source repetition rate of 10 kHz the measurement times reduce to 4 s and 40 s for photon beam energy spreads of 0.2% and

2 %, respectively. Measurement times scale with the attenuation of the beam in cargo and shielding and the attenuation of the resonant photons from the HEU into the detector.

Table 8. Simulation results for backscatter NRF measurements on a 2kG HEU object in a 10cm thick steel box, centered in a container. Calculated measurement times are for one detector and for a MPS with ≤ $3x10^7$ photons per shot at a 1 kHz repetition rate.

Pb filter thickness (inches)	Detector Full Energy Efficiency (%)	σ source (keV)	#NRF counts/sp	tot counts/sp	Signal/noise within 3 keV resolution.	Source Photons per shot	counts/shot	NRF/shot	NRF Count Rate (1/s)	Time (hr)
0.5	12.5	1.5	2.1E-12	3.65E-8	8.3	5.5E+06	**0.2**	1.15E-5	0.0115	0.97
0.5	12.5	15.0	2.1E-13	3.64E-8	1.5	5.5E+06	**0.2**	1.15E-6	0.0012	9.8
0.75	8.7	1.5	1.47E-12	3.36E-9	8.3	**3.0E+07**	0.10	4.41E-5	0.0441	**0.25**
0.75	8.7	15.0	1.47E-13	3.33E-9	1.5	**3.0E+07**	0.10	4.41E-6	0.0044	**2.6**
1	6.2	1.5	1.05E-12	5.26E-10	8.3	**3.0E+07**	0.02	3.15E-5	0.0315	0.35
1	6.2	15.0	1.05E-13	5.03E-10	1.5	**3.0E+07**	0.02	3.15E-6	0.0031	3.6

For the simulation of transmission measurements the resonant and non-resonant simulation results were combined to determine expected system performances for beams with 1.5 and 15 keV rms energy spreads in a similar way as in the backscatter simulations. The simulated spectra are shown in Figure 17. In the case under consideration here, 2 kg of HEU inside a box with 10 cm thick walls, the attenuation of resonant photons is too strong to measure the quantity of U-235 within the target area in a reasonable time. However, the objective in cargo screening is simply the detection of HEU if present. Thus the measurement time of interest is the time it takes to collect the number of NRF counts that are needed to determine with the required statistical probability the absence of resonant absorption [15]. Assuming one HPGe detector (as in the backscatter simulations), $3x10^7$ photons/pulse, and 1 kHz source repetition rate, the 6-sigma measurement times for 0.2% and 2% ΔE/E FWHM beams are 5.3 hrs and 155 hrs, respectively. Scaling this to 24 detectors and a 10 kHz repetition rate as for the backscatter measurement, the measurement times are 80 s and 2300 s, much larger than for the backscatter method. For a 1 cm thick HEU plate (instead of 4.6 cm) the corresponding estimated measurement times drop to 3 s and 80 s showing that the transmission method becomes competitive with the backscatter technique for thin HEU objects. The transmission method also benefits more rapidly as MPS energy spread reduces, and may also be particularly attractive if MPS energy spreads below 0.2% become realistic. In such cases, it has been proposed that calorimetric detectors could be used, simplifying measurement [11]

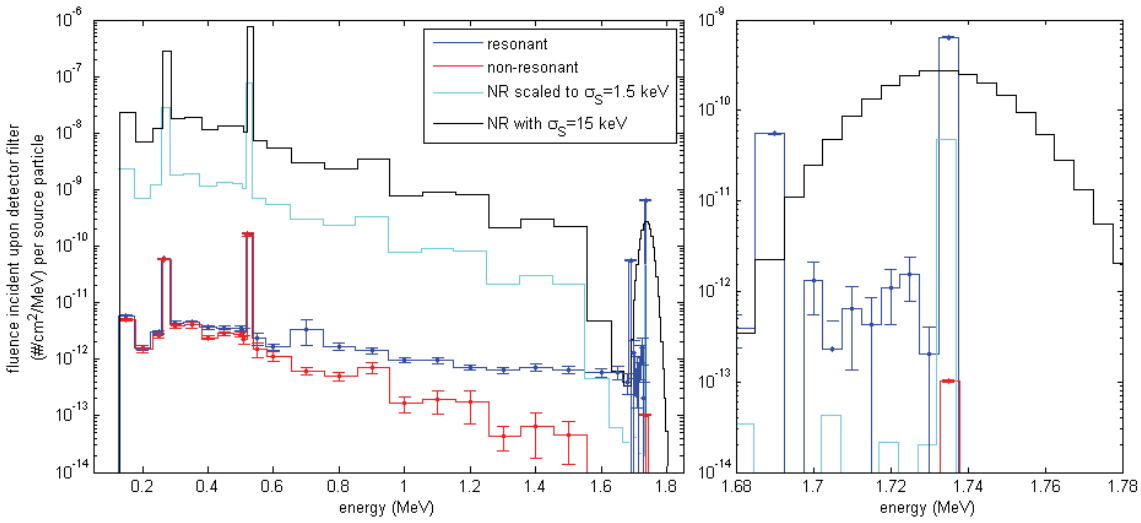

Figure 17. On left: Simulated spectra incident upon the transmission detector for the transmission configuration indicated in figure 15. The resonant (blue) and non-resonant (red) spectra are directly obtained from MCNP simulations of photon sources with widths of 8 eV incident upon a U-238 target inside shielding and a cargo container with and without NRF physics, respectively. The simulation's statistical errors are indicated, although often smaller than the widths of the lines. The non-resonant scatter produces background for the NRF peak, and these effects are approximated for the 0.2% and 2.0% beams as cyan and black, respectively. On right: Same data, zoomed in on the beam-energy region.

Energy spreads of 2% and repetition rates of 10 kHz are realistic goals for Thomson sources and would make it possible to detect 2 kg HEU inside 10 cm thick steel shielding, or within containers filled with water, in 10's of seconds in a backscatter measurement with HPGe detectors. Further in the future, Thomson sources with an energy spread of a fraction of a percent may become available that would greatly increase capability.

II.1.6 Impact on Screening Alarm Resolution and MPS Requirements

Monoenergetic photon sources strongly benefit secondary screening and alarm resolution by increasing the fraction of the source photons that overlap the cross-section of interest. Photofission excitation is less efficient in cargo applications than in single sided applications because of the limitation in a cargo context to photon energies less than 10 MeV. Nonetheless, photofission signatures are stronger than NRF for realistic MPS parameters, and for photons below 10 MeV the prompt neutron signature is strongest. Additionally, photofission places less stringent demands on the MPS, with energy spreads of 10% being desirable and, as described in section II.2 Detection, energy spreads up to 40% being usable. A source capable of generating such a beam near 9 MeV is important, prioritizing energy adjustability. For both photofission and NRF, narrow source angular spread is needed to overlap the beam with the object of interest. For the ~2 kg objects considered here, a beam divergence of < 10 mrad is ideal. With a source at 9 MeV producing ~10^8 photons/shot into 3 mrad opening angle, detection of 2 kg HEU mass behind 10 cm steel shielding could be accomplished during a radiography scan with no change in rate. A few thousand pulses (seconds at 1 kHz) could identify the same quantity behind 30cm of steel. NRF is more suitable where composition analysis is needed, either isotopic composition of SNM or contraband detection. It places more stringent demands on the MPS. At energy spreads of 2% and repetition rates of 10 kHz 2 kg HEU could be detected inside 10 cm thick steel shielding, or within containers filled with water, in 10's of seconds. Sources with an energy spread of a fraction of a percent would greatly increase NRF capability.

II.2. Detection of Hidden SNM

II.2.1 Introduction

This application section considers a constrained detection scenario; *i.e.*, it assumes that a general search location has been pre-determined and the volume to be probed is constrained to a few cubic meters. Inspection scenario examples include a car, small truck, small shed, or a location inside a house. While potentially similar in several aspects, the current application is considered categorically separate from fixed-site, commercial cargo screening since, in the present case, physical access limitations and other characteristics of a particular scenario may exclude the use of traditional radiography or transmission NRF (*e.g.,* access may be available only from one side). The objective in this single-sided inspection application is to confirm either the presence or absence of nuclear material. For clearing an object, sufficient information about the amount of shielding surrounding the nuclear material must be available to firmly conclude that a lack of observed fission signatures is not due to shielding but proves the absence of SNM. Allowable inspection times may be longer than those defined for cargo screening, since interruption of commerce may be less of a concern, and source and detector distances relative to the target may be extended and varied; measurement times in the range of minutes, and distances from a few meters to tens of meters, are reasonable to expect. Larger distances or objects (i.e. standoff, broad area scans) were excluded based on preliminary calculations.

Photofission was identified in an earlier report as the technique using MPSs that could enable a capability for detection of hidden SNM. A full discussion of the state of the art, including references, is presented in [1], and is summarized here. The most compelling advantage of an MPS-based system, when compared with bremsstrahlung-based systems, is the potential for a marked increase in the induced fission rate per unit dose on target. The continuous energy distribution of a bremsstrahlung beam results in a large fraction of the beam's photons having energies that lie outside the giant dipole resonance. In contrast, a selectable-energy, narrow bandwidth photon source can produce an inspecting beam in which essentially all incident photons have energies that can readily induce fission. Similarly, the spatial profile of some MPSs is more narrowly divergent than that of a traditional bremsstrahlung source. This permits significantly higher photon density incident on the target SNM and hence higher signal. The beam from a bremsstrahlung source can be heavily collimated to produce a small angular divergence comparable with a MPS. However, by clipping away most of the beam such an effort would severely reduce the number of fission-inducing photons on target per original source photon, resulting in lower photofission rate.

This section presents higher-fidelity calculations and modeling results to evaluate photofission techniques. This section begins with a high-level summary of the decision criteria and observable signals. The subsequent subsections present detailed simulations quantifying capability for various target and shielding scenarios. It is worth noting that, depending on the concept of operations, it may be possible to perform Compton backscattering, or similar techniques, in single-sided cases to narrow the inspection area. For example, a dense object identified inside a vehicle would then be scanned. A pulsed Thomson source may enable such backscatter imaging that, possibly in combination with other methods, can be used to determine or put a limit on the extent of shielding.

II.2.2 Signatures and Criteria

In the context of a general search application, the criterion for detection was chosen to be the observation of photofission signals, above natural and/or induced backgrounds, from which the presence (or absence) of nuclear material could be verified. More specifically, a decision of "Detected" or "Not Detected" is made here based on whether the net detected yield surpassed a

critical decision level as defined by L. A. Currie for a false positive probability of 1% [16]. For this work, we assumed, as explained below, that source beam parameters can be chosen such that any source-induced background is negligible. Currie's critical decision level then simplifies to include a lone term, which accounts for the presence of passive background. Values for passive gamma ray and neutron backgrounds were taken from Ref. [17].

The signatures of interest for this application are based on the neutron and gamma-ray emissions inherent to fission reactions:

- Delayed Neutrons. Ideally, a fission signature based on delayed neutrons would include all neutrons that are emitted following β-decay of excited fission fragments. However, source-induced prompt radiation may interact in the environment and continue to impinge on the detectors for some time following the source pulse. Previous research has shown that a careful selection of a "delayed region" essentially eliminates any source-induced neutron backgrounds from contributing to the delayed neutron signal [17]. For the current effort, total delayed neutron detection rates were adjusted by assuming the delayed region excluded the time period of 0-13.8 ms following an inspection pulse. Depending on the inspection system and environment for a given scenario, the specific delayed region will likely vary; however, the above value was selected for the current calculations to be consistent with recent research presented in the literature [17].
- Delayed Gamma Rays. Gamma rays emitted following β-decay of excited fission fragments can also provide a unique signature for the presence of nuclear material [18,19]. As with delayed neutrons, techniques relying on delayed gamma rays must account for source-induced prompt signals that interact in the environment and contribute to the detected signals at times following the source pulse. Again, a "delayed region" is defined to minimize contributions of prompt signals to the delayed gamma-ray signature. In the current work, gamma-ray emission rates were adjusted by excluding the time period of 0-30.3 ms following an inspection pulse. A delay of 30.3 ms was chosen for consistency and qualitative comparisons with recent research [17]. In practice, the specific value would be based on the employed inspection system and surrounding environment. In contrast to delayed neutrons, low-energy gamma-rays emitted on timescales characteristic of fission-produced delayed gamma-rays are probable from many different reactions, even when relatively low inspection source energies are used. To mitigate this contribution, the delayed gamma-ray signature is typically defined as high-energy (> ~3 MeV) gamma rays detected within the delayed time region. Previous work has shown that, by keeping inspection photon energies below ~20 MeV, almost all of the source-induced, delayed gamma-ray background can be mitigated [17].
- Prompt Neutrons. The prompt neutron signature relies on neutrons emitted from fission fragments shortly after scission has occurred (10^{-15} s) [20]. The large amount of energy released during fission allows for prompt neutron energies to exceed ~10 MeV, regardless of the energy of the neutron or photon that induced fission. Prompt neutrons are also significantly more abundant during fission than are delayed neutrons, although potential interferences to this signature occur at much lower inspection beam energies. To compensate for such interferences, photon energies are typically limited to 10-12 MeV, allowing for an energy threshold to be set on the detected signal. The threshold value depends on both the inspection source energy and the neutron separation energies for isotopes comprising natural and/or commonly encountered materials. Neglecting beryllium, ^{207}Pb has one of the lowest (,n) thresholds of commonly encountered isotopes at 6.7 MeV. Hence, assuming the maximum incident photon energy is 10 MeV, setting a threshold value of 3.3 MeV minimizes contributions of non-fissionable materials to the prompt neutron signature. At photon energies above 8.84 MeV neutrons from the breakup of deuterium

have energies above the 3.3 MeV threshold but they usually are not a significant interference because of the low natural abundance of deuterium.

II.2.3 Simulation Study Problem Definition and Setup

The simulation study for this application area focused on the ability of an MPS-based system to confirm the presence of nuclear material and the information this data can give for determination of absence. Based on initial calculations, the material is housed inside a reasonably-sized container (size based on initial calculations) and is shielded with varying thicknesses of water, steel, or composite material (lead and borated polyethylene). Assessing the thickness of shielding through which signals would be observed were material present gives information on the size of object within which a determination of absence could be made. A representative geometric layout of the simulations is shown in Figure 18. The inspection objects were placed in the center of a 7.7 m^3 box (2 mm stainless steel walls), with a source-to-target distance of 20 m. The detectors were assumed to be collocated with the source and had a total surface area of 4 m^2. Since the focus of the study was potential advantages and capabilities afforded by an MPS-based system, rather than on the performance or development of detector technologies, subsequent calculations assumed that the intrinsic efficiency of the detectors was 30% for prompt neutrons and high-energy delayed gamma-rays, and 4% for delayed neutrons.

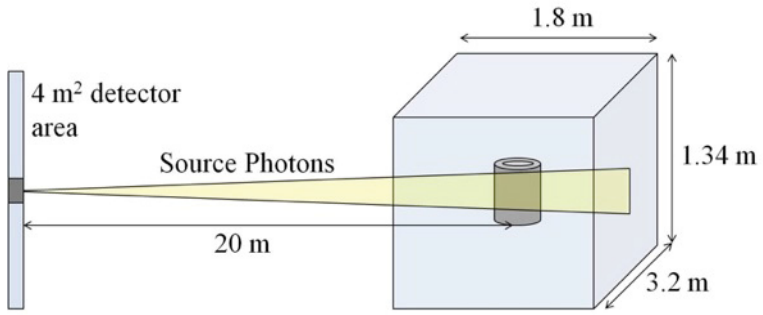

Figure 18. Representative setup used for the simulations.

The inspection object was based on HEU storage castings used at Y-12 that have been presented in the literature [21]. These HEU annuli comprise ~18 kg of 93.2% enriched uranium, with an outer diameter of 5 inches. For the simulations, the inner diameter was set to 3 inches; the height was set at 11.3 cm to match the reported mass of the annuli. Three inspection object configurations were considered:

- Configuration A: single cylinder, axis orthogonal to the beam (Figure 19A)
- Configuration B: single cylinder, axis centered with the beam (Figure 19B)
- Configuration C: two cylinders, axes parallel to the beam (Figure 19C)

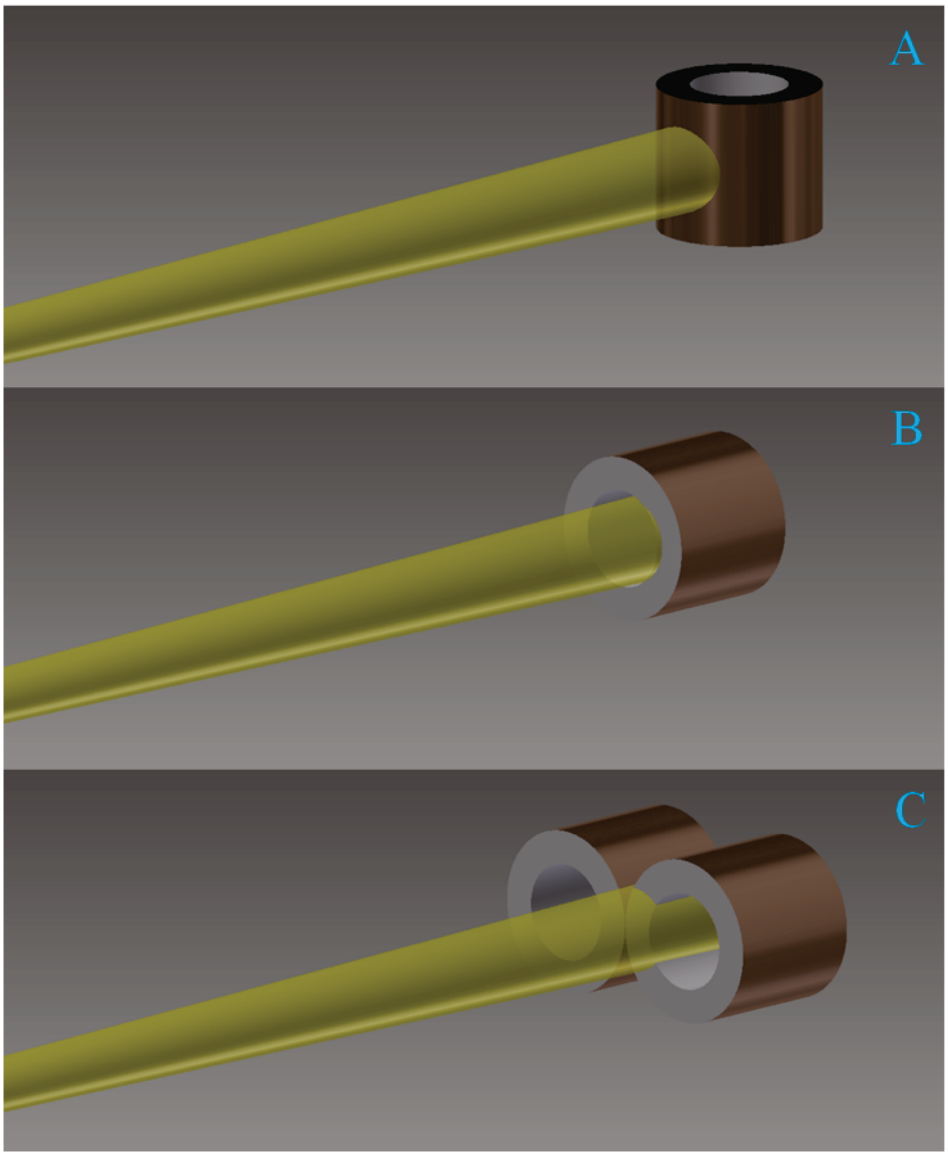

Figure 19. Inspection object configurations considered for the simulations. Each cylinder is 11.3 cm in height, with inner and outer diameters of 3 and 5 inches, respectively. Each consists of ~18 kg of 93.2% enriched uranium, and is based on the HEU storage castings presented in [21].

The ability to detect the presence of fissionable material was then assessed using these inspection object configurations and the following shielding conditions:

- No shielding present
- Stainless steel
    - 5, 10, 20 or 30 cm of steel shielding
- Water
    - 5, 10, 20 or 30 cm of water shielding
- Composite
    - 5 cm of Pb + 25 cm borated polyethylene shielding
    - 10 cm of Pb + 20cm borated polyethylene shielding
    - 20 cm of Pb + 10 cm borated polyethylene shielding

MPS Parameter Optimization to Maximize Fission Signatures

In order to fully assess an MPS-based system's potential capability, the optimal beam parameters were first investigated. Because this application depends on concentration of flux on a relatively small object (the whole box subtends only 10 mSR), a narrow-divergence source, such as a Thomson source, is a priority. For such a source, the number of source photons emitted per shot was assumed to increase linearly with increasing width of the energy distribution as is realistic [22]. This substantially affects optimization. Narrow energy spread results in having few photons available. On the other hand, broad energy spread may mean that photons in the high-energy tail of the distribution have energies high enough to be problematic. The appropriate energy spread and energy are a compromise between these limits. The energy distribution was approximated by a Gaussian distribution down to the ~2% level, at which point the photon flux was assumed to be zero, which emulates the physical cutoff due to the maximum electron energy:

$$\Phi(E) = 0 \;\; if \;\; \frac{(E-b)^2}{2c^2} \geq 4$$

$$\Phi(E) = \frac{1}{c\sqrt{2\pi}} e^{\frac{-(E-b)^2}{2c^2}} \;\; otherwise.$$

In these equations, b is the beam's centroid energy, and c = FWHM/2.3548. The values used here are based on an extrapolation from a linear fit to anticipated photon numbers. Then, with these considerations, the expected fission production in an arbitrary target can be calculated for a range of beam centroid energies and energy widths. The total fission production rate, per source pulse, is calculated from:

$$P = \int_{E_i}^{E_f} N(c) \frac{d\Phi(E)}{dE} \sigma(E) dE,$$

where N(c) is the number of photons per pulse, $d\Phi(E)/dE$ is the photon flux in the target, and $\sigma(E)$ is the photofission cross section.

Previous research available in the literature (*e.g.*, [17]) has shown that, for incident photon energies below ~20 MeV, the measured yield of high-energy delayed gamma rays or delayed neutrons from non-fissionable targets is consistent with passive background levels. An exception for high-energy gamma rays was observed from a beryllium target; however, beryllium is potentially a material of interest and, therefore, would not necessarily constitute a false positive. Hence, when optimizing the beam's centroid and percent energy spread, the calculations considered only those energy distributions that were below 20 MeV. Figure 20 presents the induced photofission yield versus beam centroid energy and percent energy spread. These results suggest an incident beam energy of 13.1 ± 25% MeV (8.5×10^8 photons per source pulse) as optimal for producing fission and generating the high-energy delayed gamma-ray and delayed neutron signatures in an arbitrary ^{235}U target, without generating problematic source-induced background.

For generating the prompt neutron signature described above, the beam parameters that were found to be optimal for maximizing the delayed signatures would produce excessive prompt neutrons above threshold from non-fissionable materials having low neutron separation energies. For example, as part of the selected scenarios that were simulated for this application, composite shielding comprised of varying thicknesses of lead and borated polyethylene was considered. For these cases, the relatively low (,n) thresholds of the naturally occurring lead isotopes allow for a significant yield of neutrons above 3.3 MeV. Hence, when optimizing the beam parameters for the prompt neutron signature, the maximum allowed incident photon energy was set at 10 MeV. Figure

21 shows the induced photofission yield versus beam centroid energy and percent energy spread. In this case, the calculations suggest an incident beam energy of 6.7 ± 20.5% MeV ($6.9x10^8$ photons per source pulse) is optimal for producing the prompt neutron signature, while also minimizing potential signature interferences.

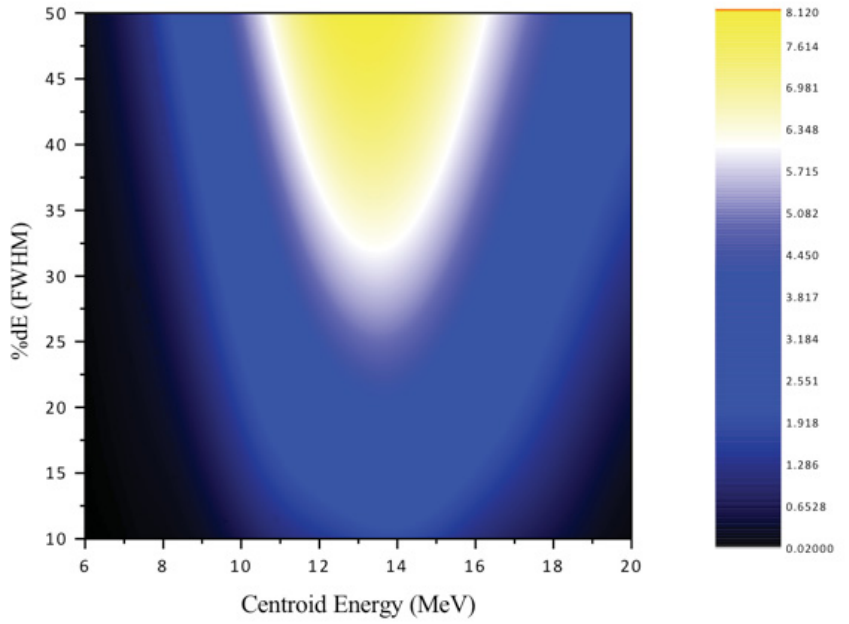

Figure 20. Relative induced photofission yield versus beam centroid energy and energy spread up to 20 MeV maximum photon energy.

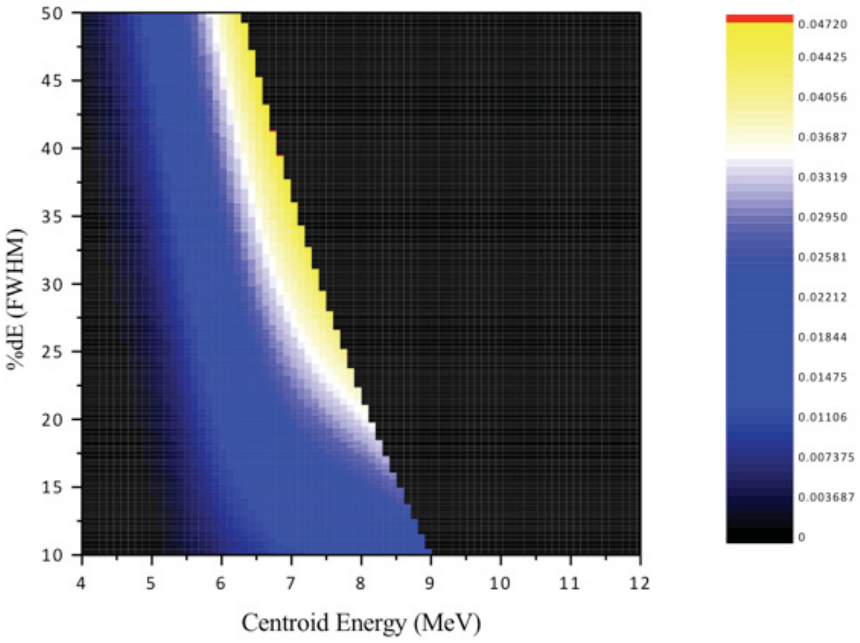

Figure 21. Relative induced photofission yield versus beam centroid energy and energy spread up to 12 MeV maximum photon energy.

The final aspect of source parameter optimization was an assessment of the beam pulsing structure. For the target-to-detector distances considered here (20 m), pulsing the source with a repetition rate of 1 kHz provides sufficient time (1 ms) for prompt neutrons produced during a given source pulse to impinge upon the detectors prior to the next successive source pulse. However, the need to exclude prompt regions when relying on delayed gamma-ray or neutron signatures requires modifications to the beam pulsing structure. In other words, the delayed signatures would not be reliable with a source operated continuously at 1 kHz. For these signatures, an interlaced pulsing mode (*i.e.*, pulse at 1 kHz during an "On" period, then completely shut off during an "Off" period) is needed. An example of an interlaced pulsing structure is shown in Figure 22. The Off period occurs during the second phase of each macropulse, and represents the time during which gamma rays or delayed neutrons would be detected (excluding a short prompt region).

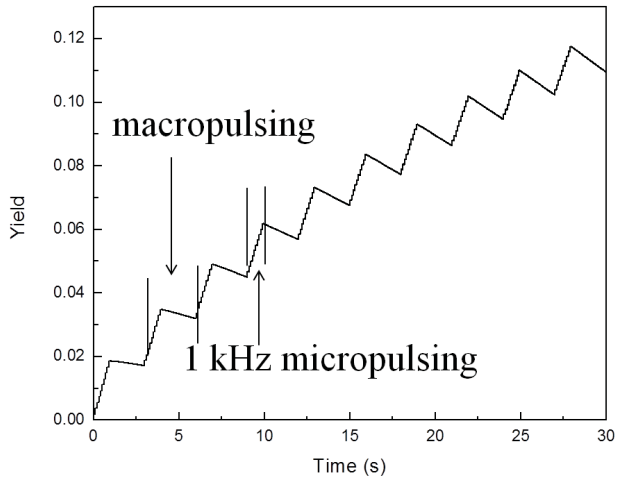

Figure 22. Example of an interlaced pulsing structure. The micropulsing occurs during the On period; the source would be shut off during the second phase of each macropulse.

Previous research, including initial study conducted for the current project, has shown that the delayed gamma-ray signature is generally stronger than the delayed neutron signature in terms of indicating the presence of fissionable material. As a result, we focused on the gamma-ray emission from fission fragments in order to optimize the pulsing structure. To initiate the optimization process, a simple MCNP6 model was developed, wherein a single, instantaneous pulse from the inspection source is assumed, and the delayed gamma-rays resulting from ^{235}U induced-fission are tallied as a function of time. Rather than relying on the simulation software's gamma-ray emission capabilities, a custom software package was developed to produce the discrete gamma-rays generated from the fission fragments, and to also convolve the time-dependent emissions from a single source pulse with an interlaced pulsing structure. This same software package was also relied upon to produce similar time- and energy-dependent delayed neutron distributions; however, only the gamma-ray aspect was utilized while optimizing the pulsing structure. Hence, details specific to the process of generating the gamma-ray distributions are discussed here; the delayed neutron distributions are discussed later.

With the developed software package, an independent fission fragment mass distribution is imported, and a total number of time bins, as well as the total decay time to consider, are selected. The software then generates a corresponding Origen-S file, which is subsequently used to produce a time-dependent distribution of isotopic abundances. From the Origen-S output, the total number of decays for each isotope during each time step is approximated by multiplying the isotopes' activities by the width of the time step. It should be noted that this method assumes that the

duration of each time bin is small compared with the half-lives of the respective isotopes, as the chosen Origen-S output has units of Curies. With the total number of decays, the software searches the Evaluated Nuclear Structure Data Files and extracts the discrete gamma-ray emissions for each isotope at each time step. As an example, consider the isotope ^{84}As, which is produced with an abundance of 0.0023 atoms per fission (^{235}U, ENDF/B-VII). After two 333.3 ms time steps, Origen-S gives the activity of ^{84}As as 9.19×10^{-15} Ci. The software pulls each of the gamma rays associated with ^{84}As decay and adds them, in the correct abundance based on the activity, to an MCNP6-formatted source file. An excerpt from a source file is shown in Figure 23, with the ^{84}As gamma rays highlighted.

```
      3.0247      1.2365807E-06
      3.071      1.73520195E-06
#     SI4         SP4
      L           D
      3.6688       2.09507566666667E-07
      3.03946       2.51598298E-06
      3.1694       6.94890537333333E-07
      3.4746       8.26680122E-07
      3.748       6.46967052E-07
      4.1279       8.14699250666667E-07
      4.2809       7.1885228E-07
      4.9457       1.61741763E-06
      5.0868       8.26680122E-07
      5.1499       1.06629754866667E-06
      3.0454       2.6262045E-11
      3.2353       2.1009636E-11
      3.3658       3.04639722E-11
      3.9275       7.14327624E-11
```

Figure 23. MCNP6 source file excerpt showing the ^{84}As gamma rays and their abundances, per fission, 667 ms after fission.

This process is completed for every fission fragment (and their subsequent daughters), at each time step. Once completed, the source file is included in a final simulation, which tracks the gross gamma-ray flux incident on the modeled detectors at each time step. The result (see Figure 24) is a time-dependent, gross gamma-ray yield distribution, from which all gamma rays with energies below 3 MeV have been excluded.

As a final step, the software package takes the yield distribution and convolves it with an interlaced pulsing structure for various combinations of On and Off times. A representative result is shown in Figure 25, which gives the gross gamma-ray yield from fission fragments versus On time (Macro pulse width) and Off time (Count time between macro pulses). From these calculations, the optimal ratio, regardless of the On time, appears to generally follow a 1:1 On to Off ratio. We also note that these calculations assume a 30.3 ms prompt region. Depending on the environment for a given scenario, the prompt region may have to be extended much further in time, ultimately resulting in optimal On and Off times that deviate from a 1:1 ratio. Nevertheless, such a deviation would likely be location and environment specific. Thus, the 1:1 ratio shown to be optimal for the prompt regions considered was used here.

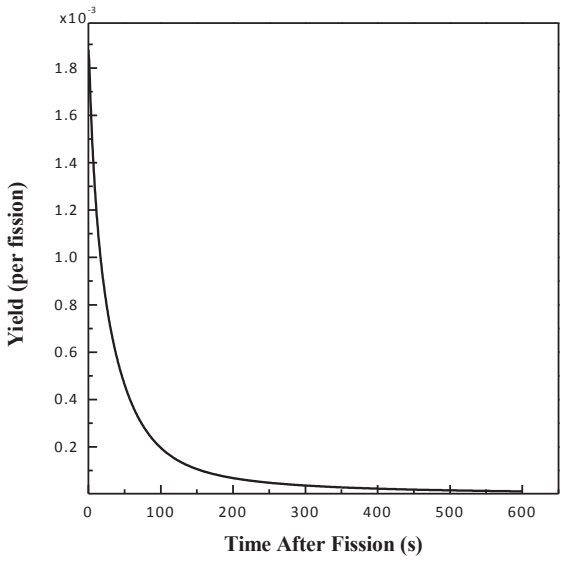

Figure 24. Time-dependent, gross gamma-ray yield ($E_\gamma \geq 3$ MeV) per fission incident on an arbitrary detector surface.

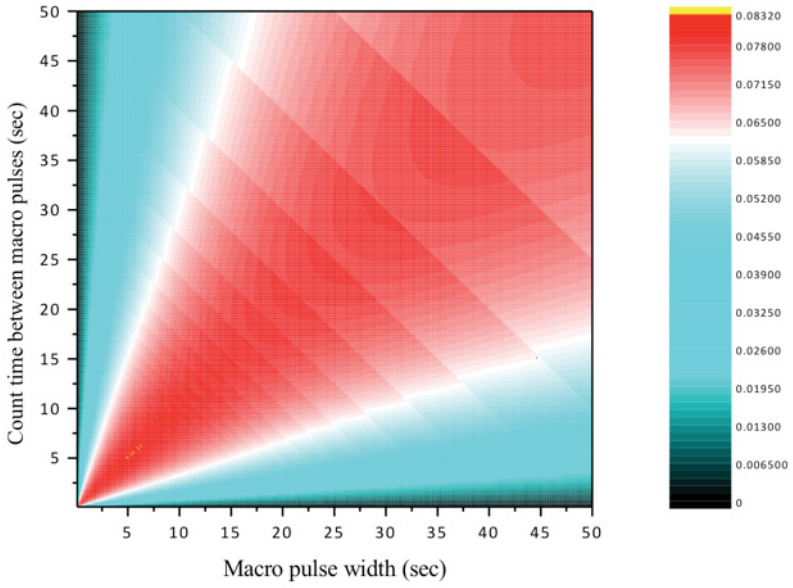

Figure 25. Relative gross delayed gamma-ray yield from fission fragments as function of macro pulse width (On time) and count time between pulses (Off time). These calculations assumed a 1 kHz micropulsing rate and a 300 s total measurement time.

For the delayed neutron yields, convolving the time-dependent gross yields incident on the detector was completed analogously with the delayed gamma rays. The time- and energy-dependent distributions for delayed neutron emission were not taken from the fragment distributions and ENSDF database. Rather, a six group delayed neutron scheme was assumed, with the corresponding data from ENDF/B-VII. The six group scheme is based on an average of ~270

known delayed neutron precursors, which are combined into one of six groups based on their half-lives. Each of the six groups then has a corresponding decay constant, group abundance, and associated energy distribution. The energy distribution of each group is shown below in Figure 26. The data shown in the Figure are normalized such that the total yield for each individual group is set to unity.

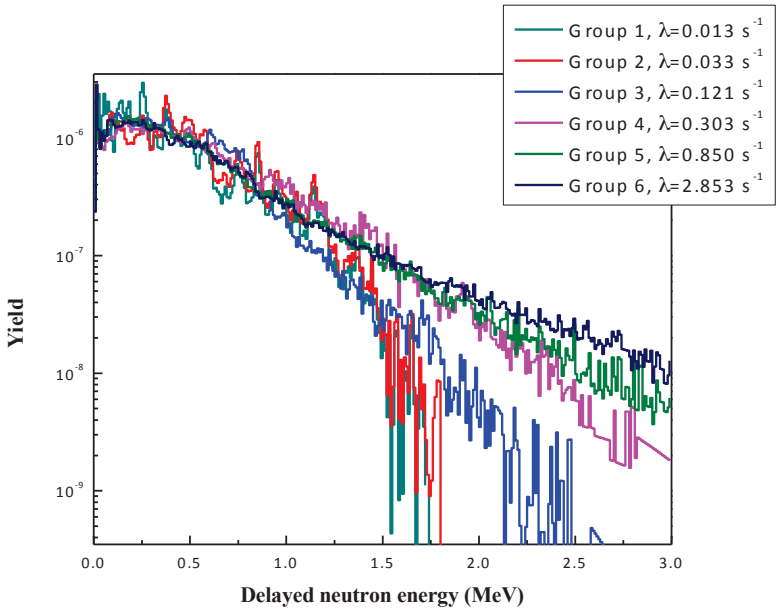

Figure 26. Energy distributions for each of the six delayed neutron groups. The distributions are normalized so that the sum of yields for each group equal 1.

In contrast to the delayed gamma-rays and delayed neutrons, an interlaced pulsing structure would not be required for prompt neutrons, assuming maximum source repetition rates of ~1 kHz and distances similar to those considered here (tens of meters). Hence, for assessing the prompt neutron signature, it was assumed that the source would be pulsed continuously for the entire inspection period. Prompt neutron emission rates, per fission, and their respective energy distributions relied on the LLNL fission model [23].

The MPS parameter simulations established appropriate beam settings to be used for each signature to maximize potential signal.

II.2.4 Simulation Results: Detection of Hidden SNM

The simulations assessed each inspection object configuration and set of shielding conditions, using the optimized MPS beam parameters described above. Initial simulations were completed, during which the inspection beam was modeled and transported to calculate the total number of fission reactions that were induced (photofission and secondary, neutron-induced fission), as well as to track the location of fission sites within each inspection object. An example is given in Figure 27, which shows a cross section of an inspection object and the induced fission sites for an unshielded object in Configuration A. As can be seen in the figure, the majority of the fission reactions occur in the first few centimeters of the object, on the side facing the inspection source. In an effort to more precisely mimic any self-shielding effects, the locations of the fission sites were then used as the source locations in subsequent simulations, for which the prompt neutrons, delayed gamma rays, and delayed neutrons were transported to the detectors as a function of time

after the inspection beam pulse. These simulations were conducted for each object and shielding configuration to evaluate detection.

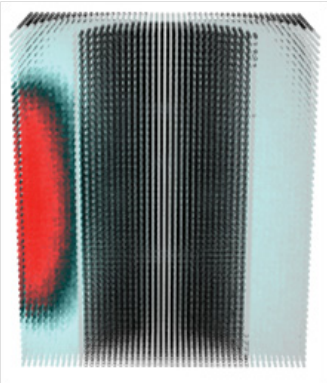

Figure 27. Cross-section of inspection object showing induced-fission sites with Configuration A.

The first set of simulations established the appropriate macro-pulse repetition rate. Figure 28 shows the simulation results for Configuration A shielded with varying thicknesses of steel; the detected net yield for delayed gamma rays is plotted as a function of macropulse repetition rate. For these simulations, the On and Off times were set to a 1:1 ratio as determined above, micropulse repetition rates were 1 kHz, and the total measurement time was assumed to be limited to 300 s. Due to the characteristic decay of fission fragments, the maximum net yields decrease as the macropulse repetition rate increases. As an example, the detected net yield for 1 Hz macropulsing is well above the critical decision level; however, as the macropulse rate increases the net yield steadily decreases and falls below the decision level for repetition rates greater than ~ 13 Hz.

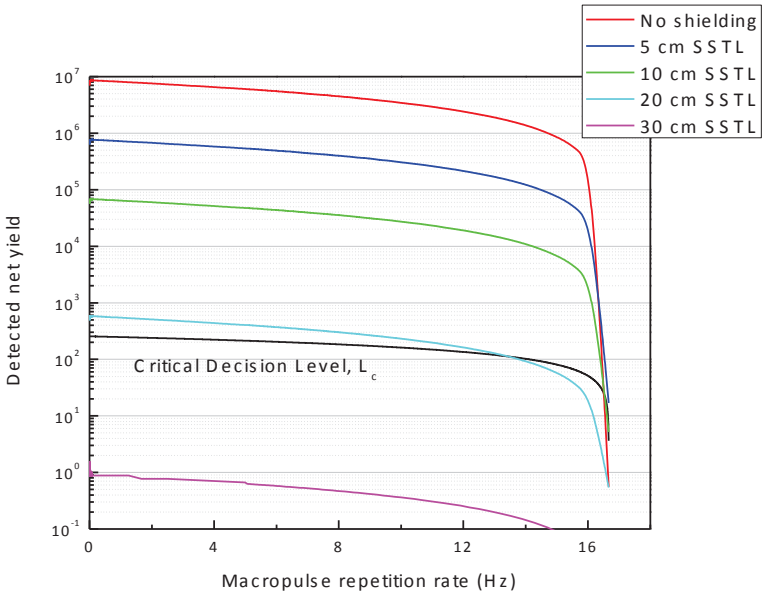

Figure 28. Detected net yield for the delayed gamma-ray signal, with target configuration A and steel shielding, as a function of macropulse repetition rate. On and Off periods were set to a 1:1 ratio. The total time allowed for a measurement was assumed to be 300 seconds.

Although the specific macropulse repetition rate for which an individual case falls below the critical decision levels varies, the general trend of decreasing net yield as a function of increasing

macropulse repetition rate was generally consistent. The final results were then calculated by setting the macropulse repetition rate to 1 Hz (0.5 s On, 0.5 s Off). While Figure 28 indicates that the net yield are moderately higher at lower macropulse repetition rates, a 1 Hz rate allows for short minimum measurement times. Conversely, the signals increase with micropulse repetition rate and with photon yield per shot, which governs total photon flux on target. Simulations presented here are for a 1kHz rate, and for 8.5×10^9 and 6.9×10^9 photons/pulse for delayed and prompt signatures respectively (as derived above). The results may be scaled to higher (or lower) rates that may be possible.

The detected net yields for the delayed gamma-ray, delayed neutron, and prompt neutron signals are given for target configuration A, as a function of shielding thickness for steel (Figure 29), water (Figure 30), and composite (Figure 31).

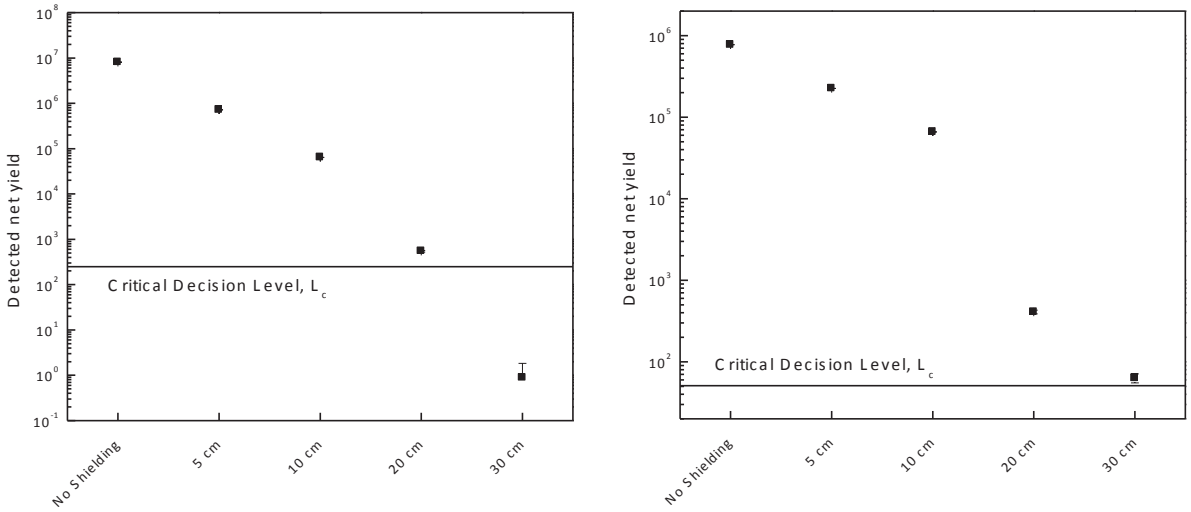

Figure 29a. Detected net yield for the delayed gamma-ray signal (left), and delayed neutron signal (right) with target configuration A, as a function of steel shielding thickness.

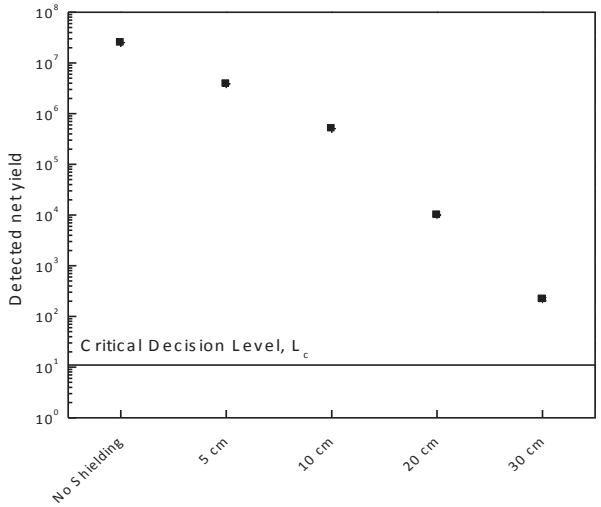

Figure 29b. Detected net yield for the prompt neutron signal with target configuration A, as a function of steel shielding thickness.

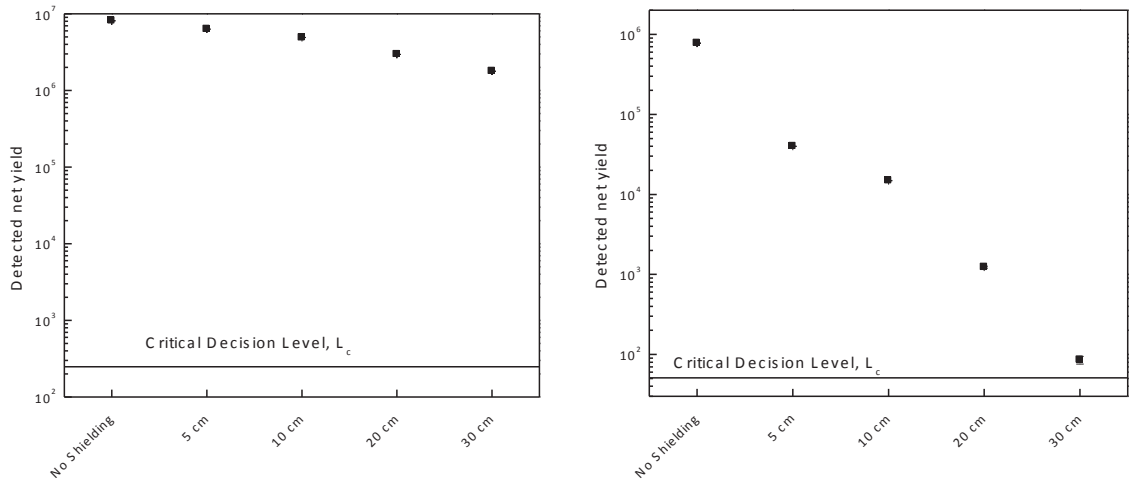

Figure 30a. Detected net yield for the delayed gamma-ray signal (left), and delayed neutron signal (right) with target configuration A, as a function of water shielding thickness.

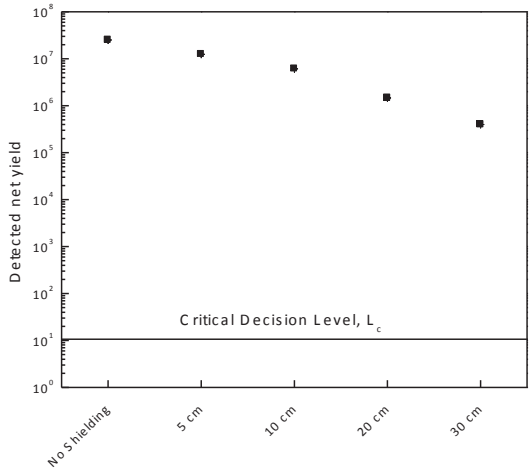

Figure 30b. Detected net yield for the prompt neutron signal with target configuration A, as a function of water shielding thickness.

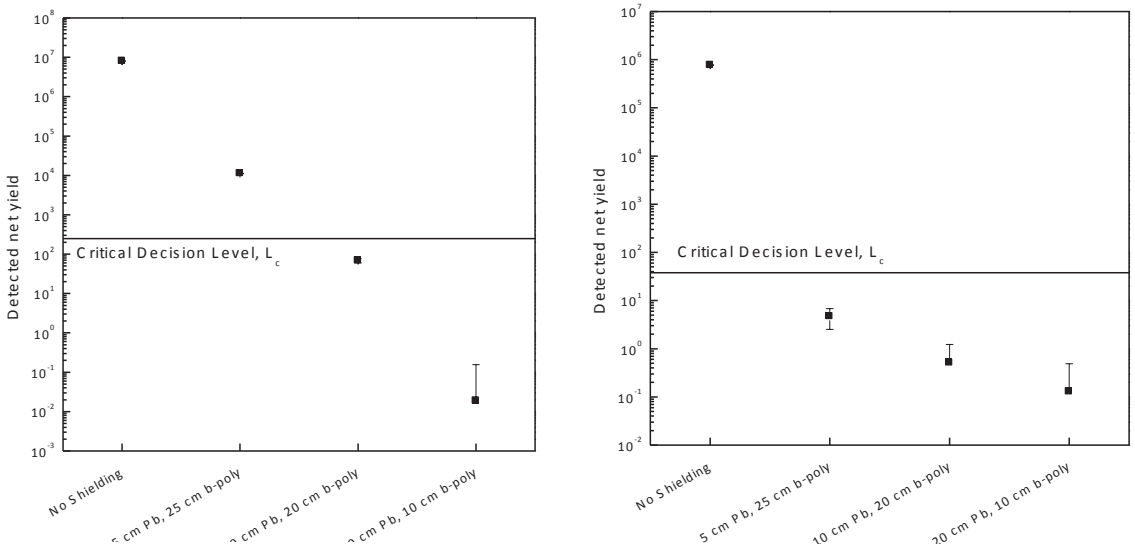

Figure 31a. Detected net yield for the delayed gamma-ray signal (left), and delayed neutron signal (right) with target configuration A, as a function of composite shielding thickness.

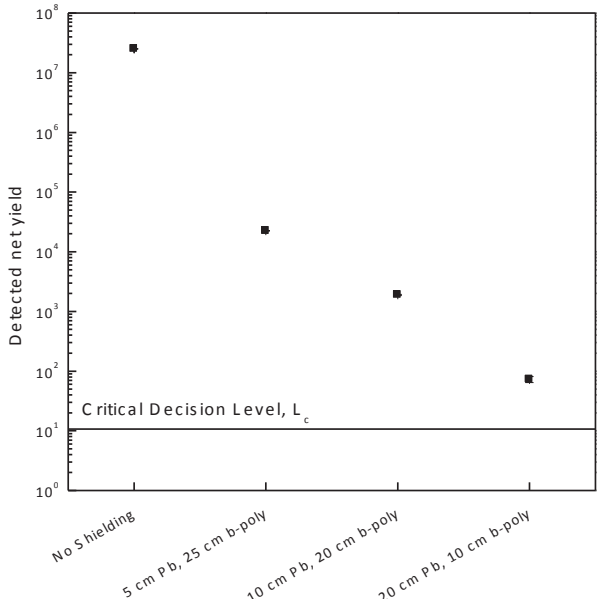

Figure 31b. Detected net yield for the prompt neutron signal with target configuration A, as a function of composite shielding thickness.

For the low Z material, water, the delayed gamma signal is strong, being ~4 orders of magnitude above the critical decision level at the maximum simulated 30 cm thickness. However, for higher Z shielding (steel or the Pb in the composite shielding) the delayed gamma signal gets strongly attenuated and drops quickly under the threshold. The prompt neutron signal is also ~4 orders of magnitude above the critical decision threshold for the water shielding but, in contrast to the gamma signal, also stays above the critical decision threshold for all simulated thicknesses of the steel and the composite shielding. This is due to the penetrating capabilities of higher energy neutrons and, importantly, also due to the low critical decision threshold. The neutron background determining the threshold for the prompt signal is low because only neutron events that happen

during the prompt counting periods contribute. The prompt neutrons are collected within ~1 microsecond of each beam pulse so that at a repetition rate of 1 kHz only the number of background neutrons arriving in the detector in 1/1000 of the 300 second total measurement time contribute. The delayed neutron signal is in general weaker than the prompt neutron signal, but still produces usable signatures in the water and steel cases simulated, and in the thin composite cases.

Table 9, 10, and 11 present the results of the simulations for Configuration A, B, and C, respectively. With Configuration A, each of the three signatures would correctly indicate the presence of fissionable material through at least 30 cm of water shielding. Although the delayed gamma ray would produce false negatives for steel shielding thickness near 30 cm, the net yields for delayed and prompt neutrons remain above the critical decision level for at least 30 cm of steel shielding. For the composite shielding cases, only the prompt neutron signature remained above the decision level for all three lead + borated polyethylene cases, also up to 30 cm thick. Because the primary goal of this study was to indicate what thickness of an unknown material could be penetrated, thicker water or other shielding was not simulated even in cases where the signal levels at 30cm were substantially above the decision level.

For Configuration B, each of the three signatures would correctly indicate the presence of fissionable material through at least 20 cm of water shielding, with the lone false negative occurring with the delayed neutron signature and 30 cm of water shielding. Each of the delayed signatures produced a false negative for 30 cm of steel shielding, although the delayed neutrons were successful for at least 20 cm of steel shielding. The prompt neutron signature stayed above the decision level for all steel shielding cases correctly indicating the presence of fissionable material. Due to the relatively small target area subtended by the beam with Configuration B, as well as the substantial beam attenuation through the lead shielding, only the delayed gamma-ray and prompt neutron signatures resulted in net yields above the critical decision level for composite shielding with 5 cm of lead and 25 cm borated polyethylene. The prompt neutron signature was the only successful one for composite shielding with 10 cm of lead and 20 cm borated polyethylene. All other cases resulted in false negatives.

With Configuration C, all three signatures had net yields greater than the respective decision levels for all water shielding thickness and at least 20 cm of steel shielding. Only the prompt neutron signature was successful for the 30 cm of steel shielding. Similarly, both delayed signatures were unsuccessful when at least 20 cm of lead shielding was present. The delayed neutron signature produced false negatives for all thicknesses of composite shielding, while the delayed gamma-ray signature was successful for only the 5 cm lead + 25 cm borated polyethylene case. The prompt neutron signature was the only one successful for all composite shieldings.

Table 9. Configuration A, 1 Hz macropulse repetition rate, 300 s total measurement time.

Shield Material	Thickness (cm)	Delayed γ-rays > L_c	Delayed Neutrons > L_c	Prompt Neutrons > L_c
No Shielding	N/A	Yes	Yes	Yes
Water	5	Yes	Yes	Yes
	10	Yes	Yes	Yes
	20	Yes	Yes	Yes
	30	Yes	Yes	Yes
Steel	5	Yes	Yes	Yes
	10	Yes	Yes	Yes
	20	Yes	Yes	Yes
	30	No	Yes	Yes
Composite (Lead/Borated Poly)	5/25	Yes	Yes	Yes
	10/20	No	No	Yes
	20/10	No	No	Yes

Table 10. Configuration B, 1 Hz macropulse repetition rate, 300 s total measurement time.

Shield Material	Thickness (cm)	Delayed γ-rays > L_c	Delayed Neutrons > L_c	Prompt Neutrons > L_c
No Shielding	N/A	Yes	Yes	Yes
Water	5	Yes	Yes	Yes
	10	Yes	Yes	Yes
	20	Yes	Yes	Yes
	30	Yes	No	Yes
Steel	5	Yes	Yes	Yes
	10	Yes	Yes	Yes
	20	No	Yes	Yes
	30	No	No	No
Composite (Lead/Borated Poly)	5/25	Yes	No	Yes
	10/20	No	No	Yes
	20/10	No	No	No

Table 11. Configuration C, 1 Hz macropulse repetition rate, 300 s total measurement time.

Shield Material	Thickness (cm)	Delayed γ-rays > L_c	Delayed Neutrons > L_c	Prompt Neutrons > L_c
No Shielding	N/A	Yes	Yes	Yes
Water	5	Yes	Yes	Yes
	10	Yes	Yes	Yes
	20	Yes	Yes	Yes
	30	Yes	Yes	Yes
Steel	5	Yes	Yes	Yes
	10	Yes	Yes	Yes
	20	Yes	Yes	Yes
	30	No	No	Yes
Composite (Lead/Borated Poly)	5/25	Yes	No	Yes
	10/20	No	No	Yes
	20/10	No	No	Yes

II.2.5 Impact on Detection Application and MPS Requirements

The requirements for use of an MPS-based system for an SNM search application may not be as stringently defined as it would be for other applications. For instance, the acceptable measurement time is likely to be scenario-dependent based on the environment, location, and/or operational considerations. If dose at the target location, or on the environment surrounding the target, is not of primary concern, then producing the highest rate of source photons within a limited energy range would minimizes the time required to detect a material of interest. It is to be expected, however, that dose down-stream of the source location is likely to be an important consideration.

Positively identifying the presence of fissionable material was shown to be realistic at distances of ~20m, through shielding thickness up to 30 cm using an MPS delivering in the range of 10^{12} photons/second into a narrow divergence beam (few-mrad opening angle). Operating an MPS at 13.1 ± 25% MeV (8.5×10^8 photons per source pulse) for delayed signatures and 6.7 ± 20.5% MeV (6.9×10^8 photons per source pulse) for prompt neutrons maximizes fission production without generating problematic levels of source-induced background or signature interferences. For the shielding materials considered, prompt neutrons provide the most sensitive fission signature using an MPS. The simulations were performed for a specific set of beam parameters, geometry and shielding configurations.

A wider parameter range can be evaluated by appropriate scaling. The detected gamma and neutron rates scale linearly with the source intensity, i.e., with the repetition rate and the number of photons per pulse. For example operating the source at 10 kHz instead of the assumed 1 kHz would increase gamma and neutron signal rates by a factor of 10. This may allow penetration of an additional ~10 cm of steel, or equivalent attenuation depth of other materials. Furthermore, the detected yields scale with the detector size and inversely with the square of the detector to SNM distance, and this could offer another factor of 10 in signal for distances at the 6 m scale (vs. the assessed 20 m). Again, this may allow penetration of an additional ~10 cm of steel, or equivalent attenuation depth of other materials. To first order the source to object distance does not impact the signal rate as long as the photon beam is sufficiently narrow that the full beam hits the nuclear

material. As the simulation results indicate, narrow beam divergence and high photon flux provide limited standoff capability with the decrease in signal rate with detector to target distance being the limiting factor. The object of interest also plays a role, but this is not anticipated to change the fundamental conclusions.

The results inform the size of a shielded object within which absence could be determined, and indicate that such a measurement could be realistic in objects at the $\sim 1 m^3$ size range using the source identified. A narrow-angle MPS consistent with parameters anticipated from Thomson source development is evaluated as important to enable this measurement. Even with such a source, localization and coarse size determination of a shielded object of interest is crucial to allow determination of absence. An appropriate backscatter measurement may expedite measurements by identifying high-Z or high-density areas, consequently localizing a region of interest. Such an inclusion would potentially allow the inspected volume to be increased for the same maximum inspection time, and further allow an inspection system to verify the absence of material, rather than simply detect the presence of material. An in-depth analysis regarding integrating Compton backscatter imaging, or similar techniques, was outside the scope of the current project, but backscatter work has been conducted previously and appears to be a workable solution. Further work to understand its potential with pulsed, narrow angle MPSs would appear warranted. In some application areas, other techniques such as building radar, or even visual identification, may also be of use for localization though these would not provide the Z information available from backscatter.

II.3. Treaty/Dismantlement Verification

II.3.1 Introduction

Verification of nuclear warheads and their dismantlement is a high priority for treaty verification. Photofission, NRF, and radiography were identified in an earlier report as techniques for which MPSs could provide significant performance improvements compared to bremsstrahlung photon sources [1]. A full discussion of the state of the art, including references, is presented in [1], and is summarized here. This report presents higher-fidelity calculations and modeling results to evaluate each technique for treaty verification. Techniques for treaty verification may be developed and verified first in support of stockpile stewardship, which was therefore included in the assessment as a separate section, II.4. This section begins with a high-level summary of each of the techniques. The subsequent subsections present detailed simulations quantifying benefit for several potential usage scenarios. Required intensities are derived, and scalings of performance versus source energy spread are discussed. The nominal MPS simulated is assumed to be operating at 10 kHz with a 2% FWHM energy distribution unless otherwise noted.

Photofission measurements are sensitive to fissile material in the test object. Measurement of photofission signal ratios at two or more MPS energies may make it possible to distinguish ^{235}U and ^{239}Pu from ^{238}U [1]. Such measurements would be very challenging, if not impossible, with a bremsstrahlung source because of averaging over a wide range of photon energies, effectively smearing out the isotopic differences. Photofission does not provide a direct signal for identification of high explosives (HE). It can be used to confirm presence of fissile materials for warhead confirmation and presence or absence of fissile material for dismantlement verification.

NRF measurements provide isotope-specific information, and could play a significant role in warhead confirmation and dismantlement confirmation. It is possible to identify and characterize individual isotopes, enabling NRF techniques to be used for measurements related to both fissile materials and HE. The principal advantages of an MPS source compared to a bremsstrahlung source are lower dose and faster measurements. NRF transmission measurements using MPSs can further be designed to limit the sensitivity to specific isotopes, providing a physical information barrier. For instance, a measurement can be designed to be sensitive to ^{239}Pu but not ^{240}Pu (important because the ^{240}Pu/^{239}Pu ratio is sensitive to a likely treaty partner), thereby reducing the need for an electronic information barrier to protect sensitive information. In addition, the narrow energy response of MPSs restricts the potential observables that are available, providing additional information protection.

An MPS may provide multiple advantages for conducting radiography or tomography measurements. Monoenergetic photons, the resulting reduction in scattering, and beams with narrow angle and/or small emission spot size may be combined to significantly improve on bremsstrahlung-based approaches currently deployed. However, the intrusive nature of the measurement in terms of the potential sensitive information that it could reveal present an initial handicap for acceptance radiography in treaty verification. One potential development pathway is to initially develop an MPS-based imaging system in support of stockpile stewardship, and then once the nuclear enterprise has experience with the approach to consider adaptations in support of treaty verification applications. For this reason, a detailed discussion of radiography is presented in the stockpile stewardship section.

A potential application using radiographic imaging in treaty verification is warhead and component “fingerprinting.” In this application, an MPS driven measurement provides unique identifiers of individual devices using a combination of high-resolution radiography / tomography, possibly in combination with Z discrimination and NRF. This approach may require management of

classified information but would provide very specific information needed for fingerprinting and is also applicable to stockpile management.

The potential impact of MPS-enabled techniques for treaty verification measurements could be very significant. Possible scenarios include enabling warhead confirmation, for which there is currently no known solution, as well as enabling a unique identifier for warheads and components through high-resolution radiography. In addition, a system suitable for warhead confirmation could likely be used for dismantlement confirmation, which would reduce the number of instruments required for treaty verification. Detailed results that quantify each of these scenarios are presented in the following sections.

II.3.2 Treaty/Dismantlement Verification Problem Definition and Signatures

Existing treaties verify delivery systems or count warheads on a delivery system, but do not involve measurements on individual nuclear warheads. As nuclear stockpiles reduce, it is anticipated that the need to verify nuclear warheads will increase to maintain confidence in the dismantlement process. The Office of Nuclear Verification is funding research and development efforts to prepare for this eventuality

Treaty verification involving nuclear warheads presents unique challenges to any measurement approach. The technique should not damage the warhead nor reveal any sensitive information, must be safe for personnel, be verified to function exactly as designed, and perform the intended measurements. Conventional wisdom assumes that the equipment is controlled by the host, who will likely have unmonitored access to the equipment. This latter constraint places a significant burden on the ability to authenticate the equipment. These requirements drive the development toward simple technologies, which may present a challenge for deployment of a MPS in a treaty regime.

Verification of monitored dismantlement can be divided into three distinct objectives:

1. Warhead confirmation: confirming that an item presented for inspection is a warhead.
2. Dismantlement confirmation: confirming that the warhead has been dismantled. The conventional definition of dismantlement is the separation of fissile material (FM) from high explosives (HE).
3. Detection of material diversion: the detection of small amounts of HE or FM in containers that are not supposed to hold those materials.

Our approach to each of these objectives is to determine the time-to-detection for specific scenarios. The details of the scenario depend on the objective. To evaluate material characteristics, which may be of interest for warhead confirmation, the scenarios utilized observation of specific materials for different Idaho National Laboratory (INL) Inspection Objects (IOs). [24] The INL IOs offer a range of material characteristics to test the capability of our experimental setup. If we can successfully determine the challenging characteristics of the INL inspection objects we have a greater confidence that the system will also work for actual or purported weapons and/or weapon components. For dismantlement confirmation, the challenge is the detection of small amounts of FM with larger amounts of HE and smaller amounts of HE with larger amounts of FM. For diversion detection, we additionally consider the possibility of additional shielding that would make the observation of the clandestine material more challenging. In all cases, we assumed a probability of detection of 99% and a probability of false alarms of 1% in determining the time-to-detection.

We initially considered three different physics process that could be observed using an MPS for treaty verification: radiography/imaging, photofission and nuclear resonance fluorescence (NRF). Radiography in the context of treaty verification is often viewed as too intrusive of a measurement,

requiring significant certification and authentication efforts to deploy. However, MPS-based radiography for stockpile stewardship has the potential to provide micron-scale spatial resolution, which is discussed later. As noted above, this capability may also have eventual utility for weapons fingerprinting in the treaty/dismantlement context. For the present analysis of treaty verification, we assume that only crude transmission radiography measurements are performed to isolate regions of interest for more detailed interrogation using photofission or NRF. The concept behind photofission was to use the different energy dependence of the photofission cross sections for ^{235}U, ^{238}U and ^{239}Pu to differentiate these materials. We show shortly that this approach is not apparently viable for treaty verification. The final physics process considered was NRF, which provides an isotope-specific signature for many isotopes. Beyond the discussion below on photofission, the remainder of this section is focused on evaluating the potential of MPS-based NRF measurements, as well as a comparison to current capabilities using bremsstrahlung-based photon sources.

Photofission measurements are sensitive to fissile material in the test object, but do not provide a direct signal for identification of high explosives (HE). The original concept for utilizing photofission in treaty verification was to use the differences in photofission cross section between ^{235}U, ^{238}U and ^{239}Pu at multiple energies to differentiate between these materials. Each of these materials has a significant photofission cross section, so that the observation of fission neutrons alone is not adequate to separate the FM from ^{238}U. The energy dependence of the observable neutron yields from these materials is shown in Figure 32, which suggests that measurements over different energy regions might be combined in a manner to provide sensitivity to the three different isotopes.

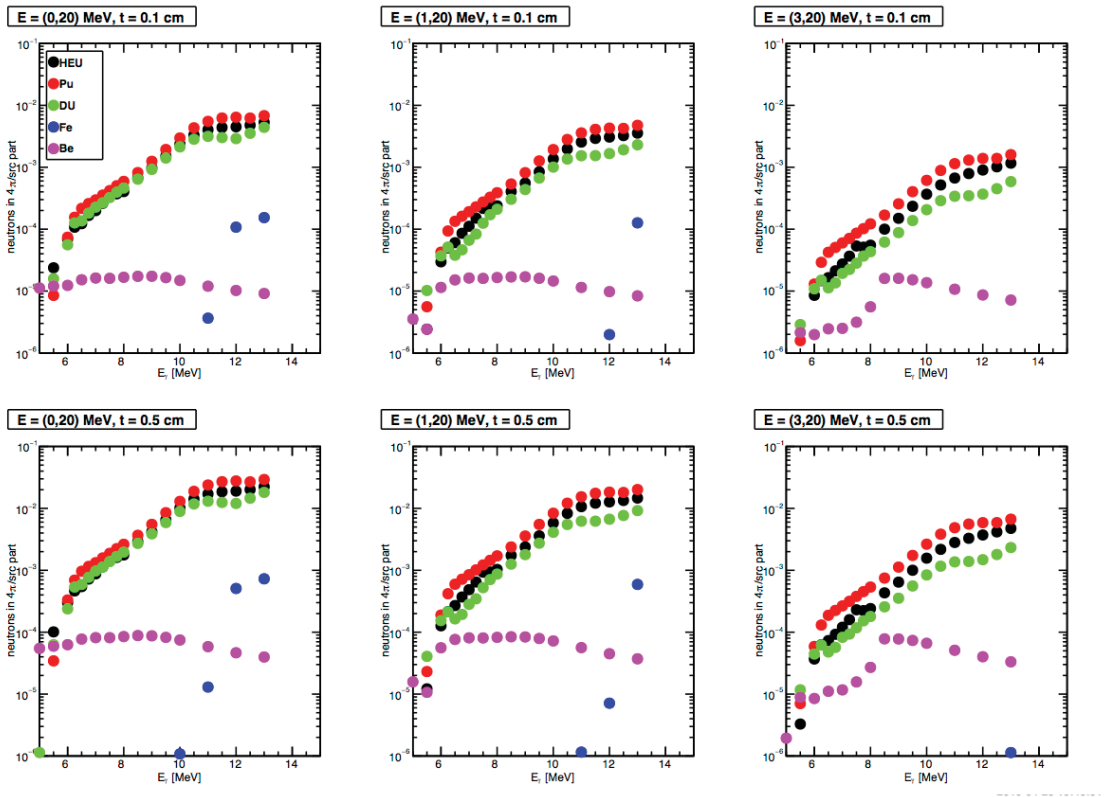

Figure 32. Neutron yields for various target materials as a function of interrogating photon beam energy from an MCNP simulation. The top row is for materials 1 mm thick, while the bottom row is for materials 5 mm thick. The left column is for all energy neutrons. The center column is for neutrons with energy greater than 1 MeV, which will be sensitive to fission neutrons and photo-neutrons for some materials. The left column is for neutrons with energy greater than 3 MeV, which is sensitive mostly to fission neutrons.

The challenge with this approach for material verification is that the order of materials is unknown. Suppose that the treaty accountable item (TAI) contains both depleted uranium (DU) and weapon's grade plutonium (WGPu), but with unknown amounts and in unknown order with respect to the beam. Since the order of the materials is unknown, the approach could be viable if the neutron yield for both orientations, Pu first-DU second and DU first-Pu second, is the same. Table 12 shows the neutron yield over all solid angles for various configurations, which differ for different material orders. For instance, the neutron yield for 1-mm Pu upstream of 1-mm of DU downstream is roughly 4 times the neutron yield for the material in the opposite order. The differences observed in neutron yields for different material ordering are due to the attenuation of the photon beam by the first material when it reaches the second material. Furthermore, the neutron yield 1-mm Pu upstream of 1-mm of DU downstream is very similar to 5-mm DU upstream and 5-mm Pu downstream. One possible means for energy-dependent photofission to still be viable is if the angular distribution differs for the ordering of the materials; however, the angular distribution was found to be the same within 1-3% statistical uncertainties of the simulations. The final possible approach for energy-dependent photofission to be viable for treaty verification is to conduct more than three measurements as a means to provide more information to help separate the thickness of types of material (i.e. to trace out the curves shown in Figures 33, 34 with high energy resolution). The propagation of uncertainty for three or more different energy measurements presented a challenging scenario to resolve material thicknesses, so that adding more measurements is likely to only increase that challenge. For these reasons, photofission was viewed as not a feasible approach at this time for treaty verification because of the difficulty to separate DU from FM. Photofission may still be a viable approach for detection and or characterization of a single material, or if the order of the materials is known.

Table 12. Neutron yields from 6.5 MeV photons incident on different target configurations from MCNP simulations.

	Neutron Yield (neutrons/src particle)	
	1 mm	5 mm
Pu First, Du Second	$4.3 \cdot 10^{-5}$	$1.9 \cdot 10^{-4}$
DU Second, Pu First	$1.1 \cdot 10^{-5}$	$4.7 \cdot 10^{-5}$

Further simulations were performed with MCNPX to examine isotopic discrimination of ^{235}U, ^{238}U and ^{239}Pu single materials using multi-energy MPS probing of photofission cross sections over a wider energy range up to 19 MeV. Total fission rates were calculated for 1 kg spheres of either HEU, DU or ^{239}Pu at 14 different monoenergetic beam energies of photons. [25] The fission rate values are plotted as function of the photon beam energy in Figure 33. The shape of the curve between 10.5 and 13.5 MeV, and the magnitude of the curve above 13.5 MeV show discrepancies between fissile and non-fissile materials that, in principle, could be used to distinguish between the isotopes of interest. Several shielded cases were tested along with the bare case to include problems of beam suppression and neutron reflection. Even in the most challenging case, shown in Figure 34, similar features in the fission rate curve were observed to those seen in the unshielded case. However, experimental observables are fission neutron and photon rates and not the fission rates shown in Figures 33 and 34. In the energy range considered here the (γ,n) cross sections are comparable to the fission cross sections thus impacting the observed signature. Furthermore, at energies around 12 MeV and above the $(\gamma,2n)$ channel is open further diluting the observable differences in fission cross sections. Therefore, while these calculations illustrate differences in the energy dependence of the photofission rates of these three materials that could be exploited for single materials,

application-specific simulations that include all contributions to observable signatures would be needed to assess this method if a desired use case were identified.

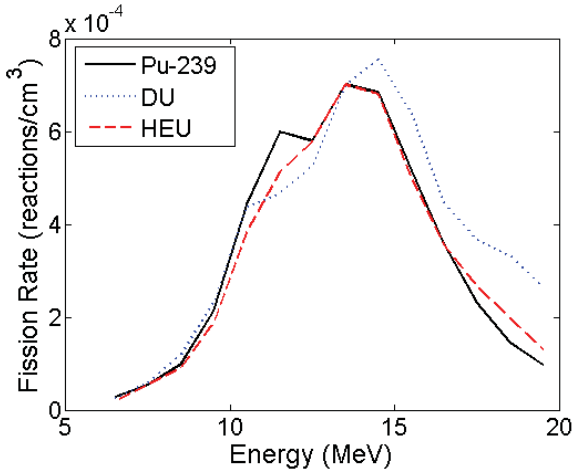

Figure 33. Scaled fission rates in bare 1kg spheres of material.

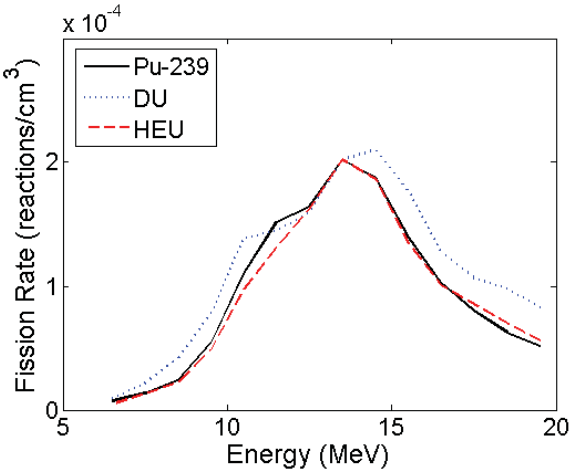

Figure 34. Scaled fission rates in 3 cm lead and 5 cm polyethylene shielded 1kg spheres of material.

NRF techniques provide isotope-specific information, but present two measurement challenges. First, the rates from NRF processes are generally low, requiring either many detectors or a high beam flux to provide an adequate counting rate for making measurements in a reasonable period of time. For comparison, a bremsstrahlung photon source designed for detecting the 1733-keV line of ^{235}U using a 2.1 MeV end-point energy can provide on the order of 20 photons/eV/μC/mSr, where the typical beam current can range from 1 to 100 μA. The second challenge is that NRF measurements can be limited by the maximum instantaneous detector rate; this concern is particularly true for bremsstrahlung-based measurements, which typically address this challenge by using a continuous-wave beam[1]. The detector rate issue will be less problematic for a MPS, since there is less low energy background dominating the detector rate.

The primary differences between the evaluations of the different treaty objectives are the geometries modeled. To examine the effect on measurement response to the presence of different materials, INL IO#5, IO#8 and IO#10, were evaluated as the contain both high density and low density materials in the form of HEU, WGPu, and polyethylene. To examine potential capabilities in the context of dismantlement confirmation, separate geometries were evaluated for confirmation of presence and absence measurements. For presence, no additional shielding of the inspected material was added to the model. For absence measurement additional high-Z material was added to provide a worst-case analysis, specifically 1.6 cm of lead shielding on all sides was added. HMX was not included in the model for absence of SNM because it would have little impact on the results, i.e. the HE would only modestly attenuate the signal and the background would be heavily dominated by the Pb shielding. The thickness of 1.6 cm was chosen to attenuate the passive gamma-ray signature of ^{239}Pu down to 1%. In the case for absence of HE, the HE was placed next to 0.375 cm of PuAl, which is the material and thickness of Pu-bearing shell in the IO#8. For diversion detection, the models for absence of SNM were used to detect diversion of SNM, whereas for HE

[1] A continuous-wave, or CW, beam is one in which the beam of particles is always on, as opposed to being pulsed, possibly with a long time between relative short pulses.

diversion, a 1.6 cm Pb shield was placed around the HE to provide a worst-case analysis for detection of diversion of HE.

For a treaty verification measurement, one hour is the maximum measurement time that could be considered reasonable, although shorter times would be better. There will be a strong preference to have only one detector, but it is not unreasonable to consider up to four detectors. All of the results shown below are for a single detector.

II.3.3 Simulation Study Setup

Radiation transport modeling was conducting using the GEANT4 framework [26,27]. Both scattering (detecting photons directly scattered from the target) and transmission (detecting photons scattered from a witness foil after passing through the target) geometries [28] were considered for all treaty verification modeling. A single 80% relative efficiency high-purity germanium (HPGe) detector was used. For scattering, the detector was placed 100 cm away from the center of the target. For transmission, the detector was placed at 25 cm away from the center of a witness foil placed downstream of the target and separated from the target by a collimating tungsten shield that allowed the primary beam to pass through the shield but eliminated scattered photons generated in the target. The witness foil was always 1 cm thick, which provides a best-case evaluation for transmission geometries because of the large efficiency for scattering resonant photons off the witness foil. The MPS was assumed to be operating with a repetition rate of 10 kHz and a 2% FWHM energy distribution. For MPS beams, a 1 cm thick lead filter was also placed in front of the detector. A 2.5 cm thick filter was used for bremsstrahlung beams; the bremsstrahlung beam produces considerably more low energy background events than a MPS beam, so that the thicker filter is advantageous.

For transmission measurements, comparisons are made between materials with and without the isotope of interest in the target but maintaining the same overall radiographic transmission. In a transmission measurement, the ratio of the rate of the observed resonant photons from the witness foil with respect to the transmitted beam current will be observed. In this modeling, the transmitted beam through the witness foil was not recorded. To provide a directly comparable normalization, the radiographic thickness of the target was held constant while the presence of the resonant isotopes was turned off and on. For instance, transmission measurements on HEU looking for the 1733 keV resonance of ^{235}U were compared against similar geometry but substituting DU for HEU in the target. This issue does not impact scattering measurements.

The modeling was handled in two stages to improve computational efficiency. First, the scattered photons of interest, either off the target or off the witness foil depending on the geometry, were recorded after passing through the lead filter for all azimuthal angles and polar angles between 120 and 140 degrees. The number of photons recorded was then scaled to account for the solid angle and intrinsic detector efficiency at the resonant energy to determine the observed signal rate.

The intrinsic detector efficiency was determined through a separate GEANT4-based simulation of the detector. An intrinsic total efficiency of 70% was used to estimate the detector rate. This value was estimated by weighing the total efficiency as a function of energy; the total efficiency was roughly constant for all energies.

In addition to the NRF signal rate, the total detector rate was estimated in the simulations. The number of photons per shot for the MPS measurements was limited so that the probability of pileup was 10%. Pileup occurs when two photons from uncorrelated scattering events are observed by the detector at the same time. When pileup occurs, the information from an NRF event is lost because

the event is shifted above the NRF peak. Following Poisson statistics, this requirement limits the mean total detector rate to 0.53 events per shot. The photons per shot was determined based on this mean total detector rate.

The maximum beam current of bremsstrahlung measurements is critical for setting the detector rate. While the photons per energy per solid angle per micro-Coulomb of beam current were determined through radiation transport modeling using Geant4, the amount of beam current was set by empirical experience from measurements on approximately 1 mm of HEU. The empirical observations on maximum beam current were scaled to account for differences in detector size and detector distance from the target. Maximum electron beam currents for bremsstrahlung measurements of 40 μA and 160 μA were selected for scattering and transmission measurements, respectively. These currents will provide a 10-20% pileup probability.

The criterion for detection was determined following Hypothesis Testing approach. A similar but different approach was used for the scattering and transmission geometries. For scattering, the required number of counts was determined by

$$n_{scat} = \left(\frac{\gamma}{\gamma - 1}\right)\left[A_D + \frac{1}{\sqrt{\gamma}}A_{FA}\right]^2,$$

where $\gamma = \frac{S}{N} + 1$, S/N is the signal-to-noise (SNR) of the NRF signature, and A_D and A_{FA} are the number of sigma required to achieve the desired probability of detection and probability of false alarm, respectively. The number of counts required for a transmission measurement when the material of interest is in the target is given by

$$n_{tran} = \beta\left(\frac{1}{1-\beta}\right)^2\left[\sqrt{1+\alpha}A_{FA} + \sqrt{\alpha+\beta}A_D\right]^2,$$

where $\alpha = N_0/S_0$ is the inverse of the SNR when the material of interest is not in the target and $\beta = S_1/S_0$ is the ratio of the resonance signals when the material of interest is in the target and is not in the target.

It was necessary to estimate the signal-to-noise ratio for a variety of measurements. The estimates were based on three empirical observations. First, that the signal-to-noise ratio (SNR) of the 1733-keV resonance had a SNR of 1 for bremsstrahlung measurements of 2 mm of HEU [29]. Second, that measurements at HIGS suggest that a 4.3% FWHM quasi-monoenergetic photon beam gave a SNR ratio roughly 2.7 times larger on DU than a similar measurement using a bremsstrahlung photon beam, see Figure 35. Correcting for a 2% FWHM MPS beam under evaluation, the SNR for ^{235}U was then assumed to be 5.8. Third, the strength of the background, as measured in Counts per mole per cm^2 per source intensity, scales as the cube of the atomic charge number, i.e. Z^3 [30]. The SNR for a specific geometry was then determined based on these observations, coupled with a calculation of C_{thick}, which is a measure of the NRF signal strength as described in [29]. One of the consequences of the Z scaling of the continuum background is that the addition of low-Z material, such as HE, has minimal impact on the SNR when SNM is present.

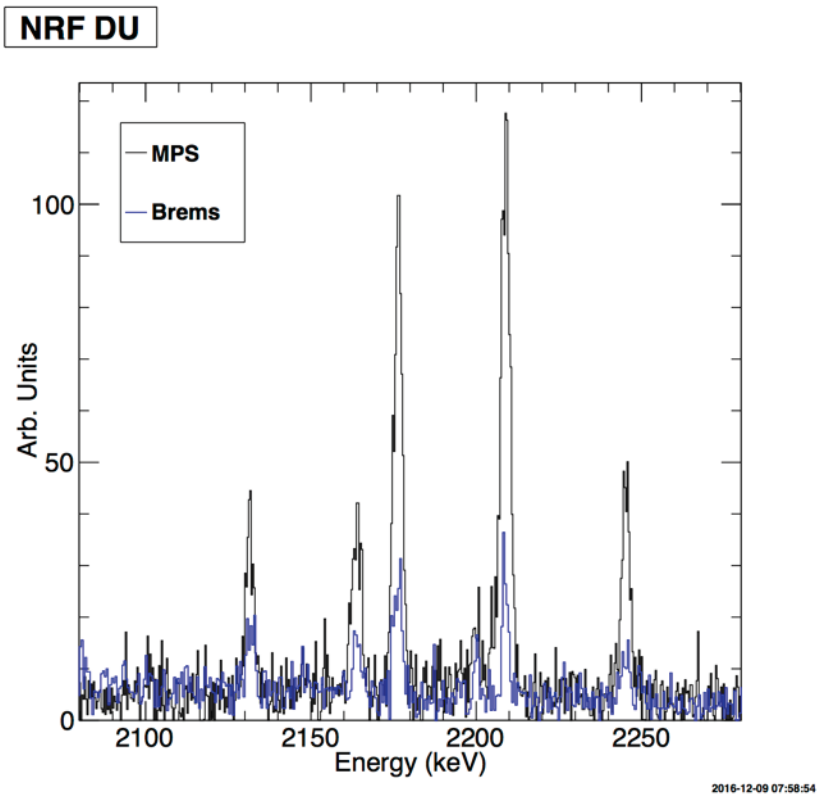

Figure 35. Comparison of NRF response from ^{238}U for 4.3% FWHM monoenergetic beam at HIGS (MPS) and 2.8 MeV end-point energy bremsstrahlung source (Brems).

The SNR impacts the number of photons required to declare detection, and the impact decreases significantly once the SNR is greater than 1. For instance, for an NRF scattering measurement with 99% probability of detection and 1% probability of false alarm, a SNR of 0.1 requires 228 events to declare detection, SNR of 1 requires 31 events and a SNR of 10 requires only 11 events. As a result, the time-to-detection is not too sensitive to the SNR so long as the SNR > 1.

A summary of the relevant NRF resonance properties is shown in Table 13. The table includes the resonant energy, the integrated cross section, and the bremsstrahlung end-point energy used in the simulations for that resonance. The maximum photons/shot required for scattering measurements is $3 \cdot 10^5$, for IO# 8.

There are two other critical assumptions made for these calculations. First, it was assumed that the material of interest had been localized, so that the photon beam was always hitting the material of interest in the target. This localization could be accomplished a number of ways, for instance through a fast series of transmission measurements. Second, that the beam scanned over the area of interest. This second assumption is not critical from a time-to-detection perspective since it is assumed that the material geometry is the same over the scanned area, but rather from a system design perspective in that rastering or scanning the beam over the appropriate area is required.

Table 13. Properties of NRF resonances. I_0 is the integrated NRF cross section.

	^{235}U	^{239}Pu	^{12}C	^{14}N
E_{res} [MeV]	1.733	2.143	4.485	4.915
I_0 [eV b]	29.8	13	10.5	4.4
E_{brems} [MeV]	2.1	2.5	5.1	N/A

II.3.4 Warhead Confirmation

One of the most challenging issues in Treaty Verification is the confirmation that an item presented to inspectors is a nuclear weapon. The detailed definition of the warhead will likely vary with the treaty, as specifics are likely to depend on the type of warheads. A possible definition for a warhead might be:

- Contains at least some threshold of high explosives (HE).
- Contains at least some threshold of fissile material (FM).
- The HE surrounds the FM.

The mass thresholds are likely to be set well below the mass of the actual item to ensure a very high probability of detection, which avoids the determination of the actual mass through a statistical sampling of many warheads. For this study, only the presence of HE and FM were evaluated. The determination of geometric properties of a TAI, which may significantly improve confidence, are often viewed as too intrusive leading to the risk of releasing classified design information. For that reason, they were not evaluated here.

Our approach to evaluate the feasibility of MPS-based sources to confirm that a TAI is a warhead is to conduct radiation transport modeling studies examining the Idaho National Laboratory Inspection Objects (INL IOs). [24] The INL Inspection Objects offer a range of material characteristics to test the capabilities of our measurement setup. If we can successfully determine the challenging characteristics of the INL inspection objects we may have a greater confidence that the system will also work for actual or purported weapons and/or weapon components. Three different IOs were studied, IO #5, IO# 8 and IO# 10. A summary of the geometries for these IOs is shown in Table 14 only one material was studied for each geometry: IO #5 Pu, IO #8 HEU, IO #10 polyethylene. The carbon in the polyethylene was used as a surrogate for nitrogen in HE for warhead confirmation. The NRF response from carbon will be approximately twice as strong as that for nitrogen. However, given the short detection times determined this factor of two is of little practical importance.

Table 14. Summary of geometries for INL IOs used in this study. The layers are numbered in increasing order going from the outside to the inside of the IO. All thicknesses are in cm.

Layer	IO# 8		IO #5		IO #10	
	Material	Thickness	Material	Thickness	Material	Thickness
1	Al	0.500	Al	0.500	Al	0.500
2	Air	2.500	LiH	2.000	Air	0.625
3	DU	0.250	Air	0.500	Poly	2.125
4	Air	0.250	DU	0.375	DU	0.250
5	PuAl	0.375	Air	0.125	PuAl	0.375
6	Air	0.625	HEU	1.000	Air	0.625

Simulation Results

A summary of the results for the time-to-detection in warhead confirmation for MPS and bremsstrahlung-based measurements, using both scattering and transmission techniques, is shown in Table 15. All times are for use of a single detector. All of the MPS-based scattering measurements require less than one hour, the maximum time considered for a treaty verification measurement. The MPS-based transmission measurements for HEU and HE require less than an hour, but the

measurement for WGPu requires almost three hours because of the relatively small amount of WGPu in the beam. The bremsstrahlung measurements for SNM require considerably more time, however the bremsstrahlung measurements for HE require only a few minutes. Furthermore, scattering measurements are faster than transmission measurements for Pu and HE, but not for HEU. That is because there is significantly more HEU in the IO#5 than Pu in IO#8, so that the attenuation of the resonant photons in the target is significant enough to quickly distinguish whether the HEU is present. Provided the appropriate measurement is selected, the advantage of MPS-based techniques is roughly two orders of magnitude faster detection for FM, while there is not a significant advantage for Carbon.

Table 15. Time-to-detection for warhead confirmation, and critical parameters.

IO	#5	#8	#10
Isotope	^{235}U	^{239}Pu	^{12}C
E_R [MeV]	1.733	2.143	4.438
SNR_{MPS}	5.8	2.5	3.6
β	0.099	0.84	0.48
Time-to-Detection [min]			
MPS-scattering	8	13	1
MPS-transmission	3	160	2
Brems-scattering	640	940	3
Brems-transmission	690	530	2

II.3.5 Dismantlement Confirmation

The objective for dismantlement confirmation is to confirm that the SNM and HE have been separated. To support this objective, it is necessary to determine that for containers that are declared to contain dismantled SNM no HE is present, while for containers that contain HE no SNM is present. As a result, for each container it is necessary to perform both a presence confirmation measurement and an absence confirmation measurement.

Several different geometries were modeled to evaluate the sensitive to confirming presence and absence of materials. For presence measurements, bare plates of the declared material are evaluated; there is no additional shielding or other material present. The thickness of the plates is varied to understand the time-to-detection as a function of material thickness. For absence measurement additional high-Z material was added. For the absence of SNM, 1.6 cm of lead shielding on all sides was added. HMX was not included in the model for absence of SNM because it would have little impact on the results, i.e. the HE would only modestly attenuate the signal and the background would be heavily dominated by the Pb shielding. In the case of absence of HE, the HE was placed next to 0.375 cm of PuAl, which is the material and thickness of Pu-bearing shell in the IO#8. The criterion for absence measurements is defined in terms of the time to detect a small amount of shielded material.

Simulation Results

The time to confirm the presence of SNM for the dismantlement confirmation objective is shown in Figure 36. Results for both NRF scattering and transmission approaches are shown, as well a result for HEU scattering using a bremsstrahlung beam for comparison. NRF scattering using an MPS can confirm the presence of SNM down to 0.1 mm thickness in less than 4 minutes. Transmission measurements take considerably longer. Even at 10 mm thick, the time to confirm the presence of WGPu using transmission is longer than 90 minutes, so that these points are not visible in the selected vertical scale. Thus, scattering measurements prove to be more sensitive. The time

to confirmation of HEU using NRF scattering for a bremsstrahlung beam is also shown. This result is fairly typical, with the time to confirm being an order of magnitude larger than an MPS-based approach. The maximum MPS photons/shot required for scattering is $1 \cdot 10^6$, for 0.1 cm WGPu. The results for scattering off SNM using an MPS show the curious result of reduced times to detection as the materials get thinner. The behavior is created by the limitation on photons/shot to limit the detector rates. The thinner the material, the higher the photons/shot that can be used to maintain the same level of pileup, which reduces the time to detection.

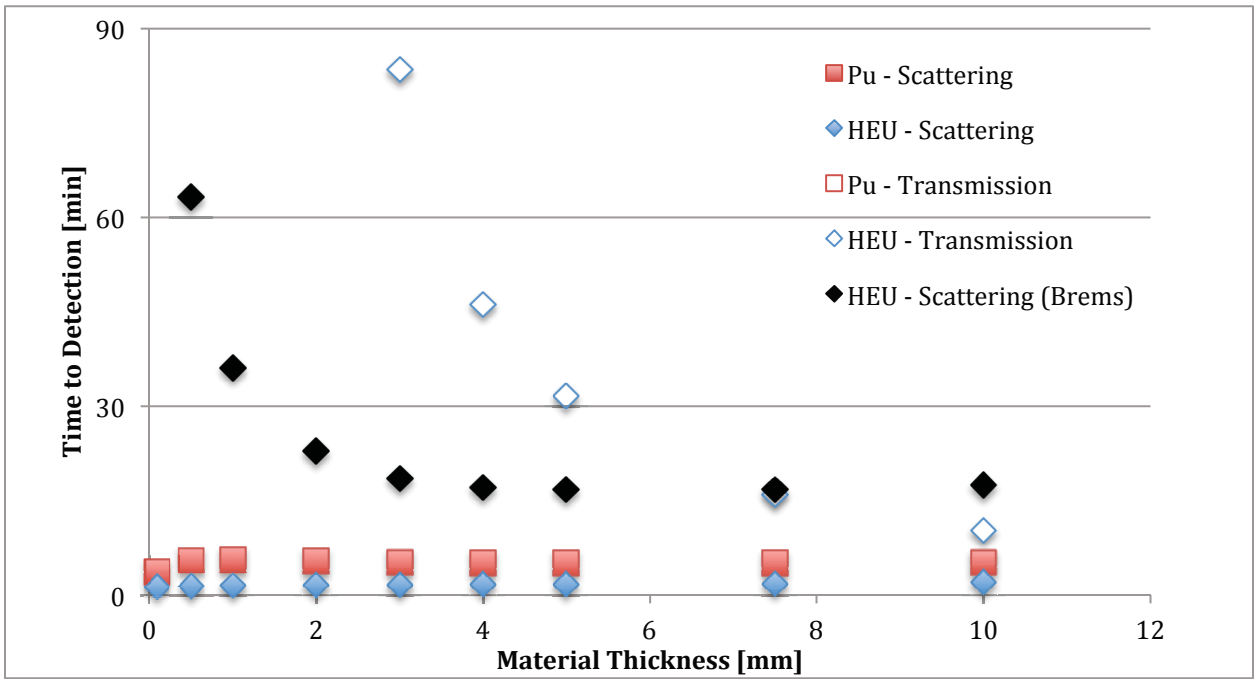

Figure 36. Time to confirm presence of SNM for dismantlement confirmation. None of the Pu transmission time-to-detection confirmations were less than 90 minutes.

The times to confirm the presence of HMX for the dismantlement confirmation objective are shown in Figure 37. Only results for scattering are shown; the sensitivity in the transmission measurements was very poor, leading to time-to-detects greater than 1,000 minutes. Again, scattering outperforms transmission, and provides the ability to confirm the presence of HMX down to 0.5 cm thick in less than 10 minutes. The maximum MPS photons/shot required for scattering is $1 \cdot 10^6$, for 0.5 cm HMX.

The time to detect hidden SNM during confirmation of absence measurements in this challenging geometry is shown in Figure 38. Again, scattering measurements outperform transmission measurements. Interpolating the curves, 1.3 mm of HEU and 3.4 mm of WGPu can be detected in an hour. Transmission measurements begin to outperform scattering measurements for HEU measurement for HEU thicknesses of 7 mm or greater. The time-to-detection for Pu using transmission was greater than ~90 minutes for all thicknesses studied; at 10 mm WGPu, the time-to-detection was 140 minutes. The maximum photons/shot required is $1 \cdot 10^5$, for 0.1 cm HEU. The differences between Figure 36 and Figure 38 indicate the impact of the lead shielding; without the lead shielding, the ability to detect smaller amounts of SNM would follow the results from Figure 36.

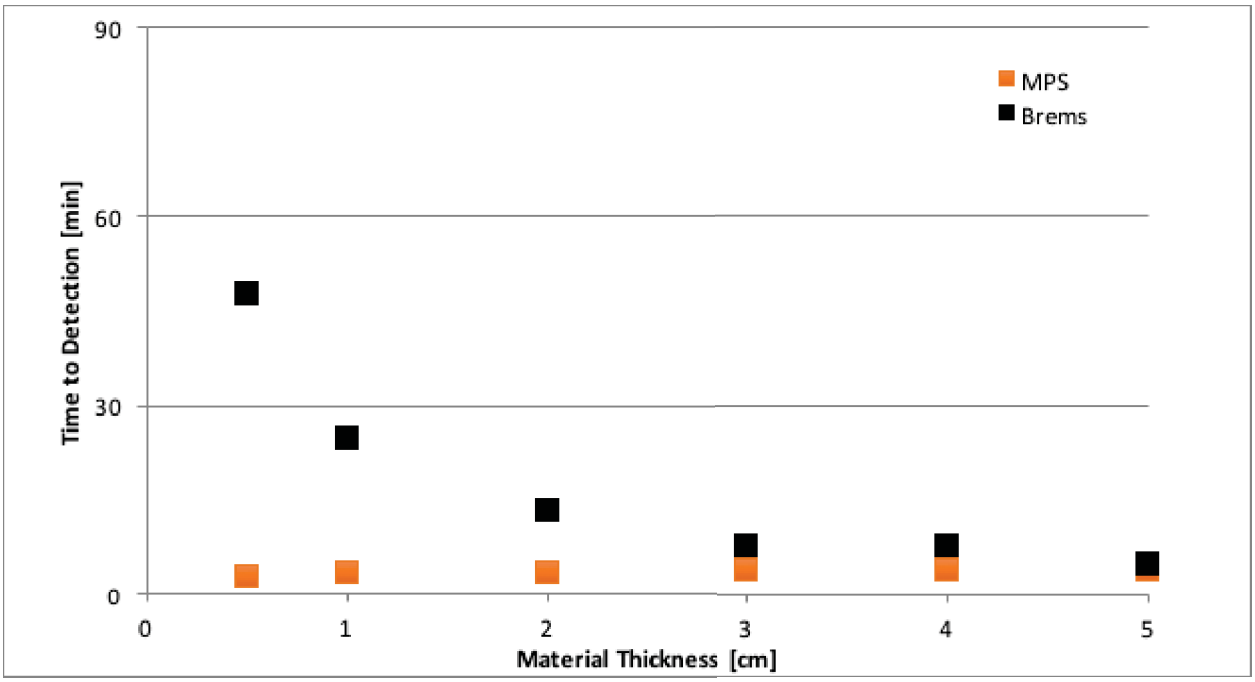

Figure 37. Time to confirm presence of HMX using NRF scattering for dismantlement confirmation. Note that the transmission response was very poor, leading to large (greater than 1000 minutes) times to detect.

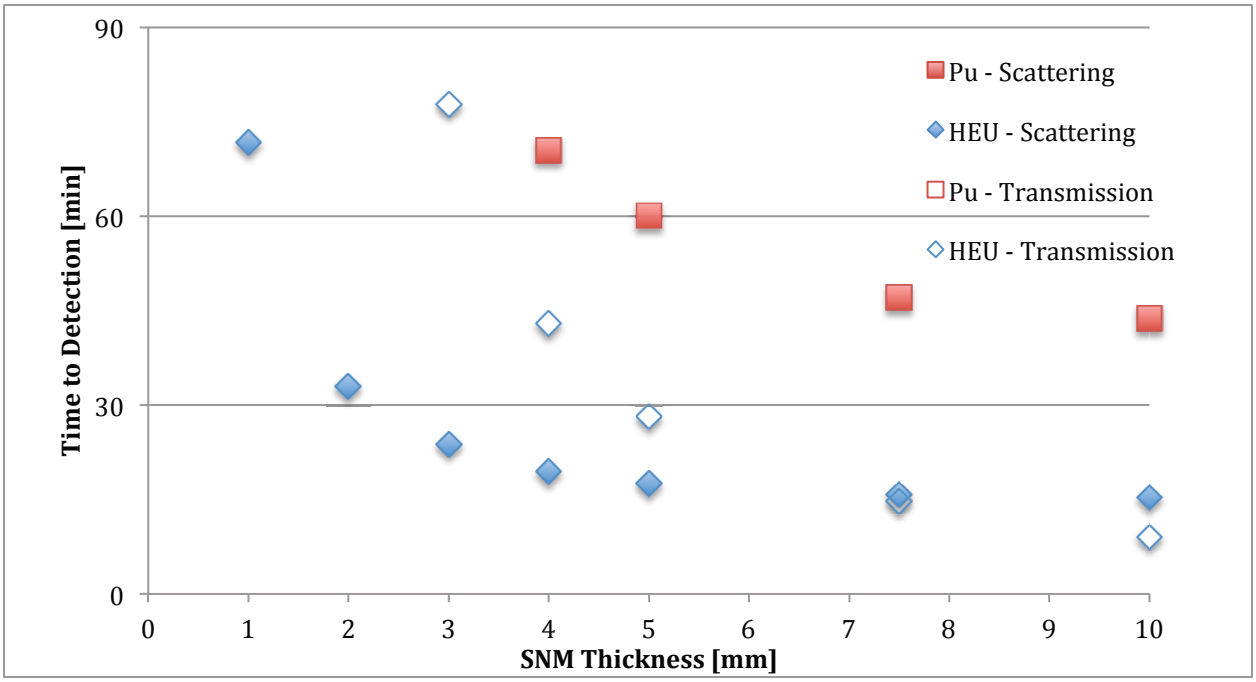

Figure 38. Time to detect SNM for absence measurements. Pu transmission measurements up to 10 mm Pu take more than 90 minutes.

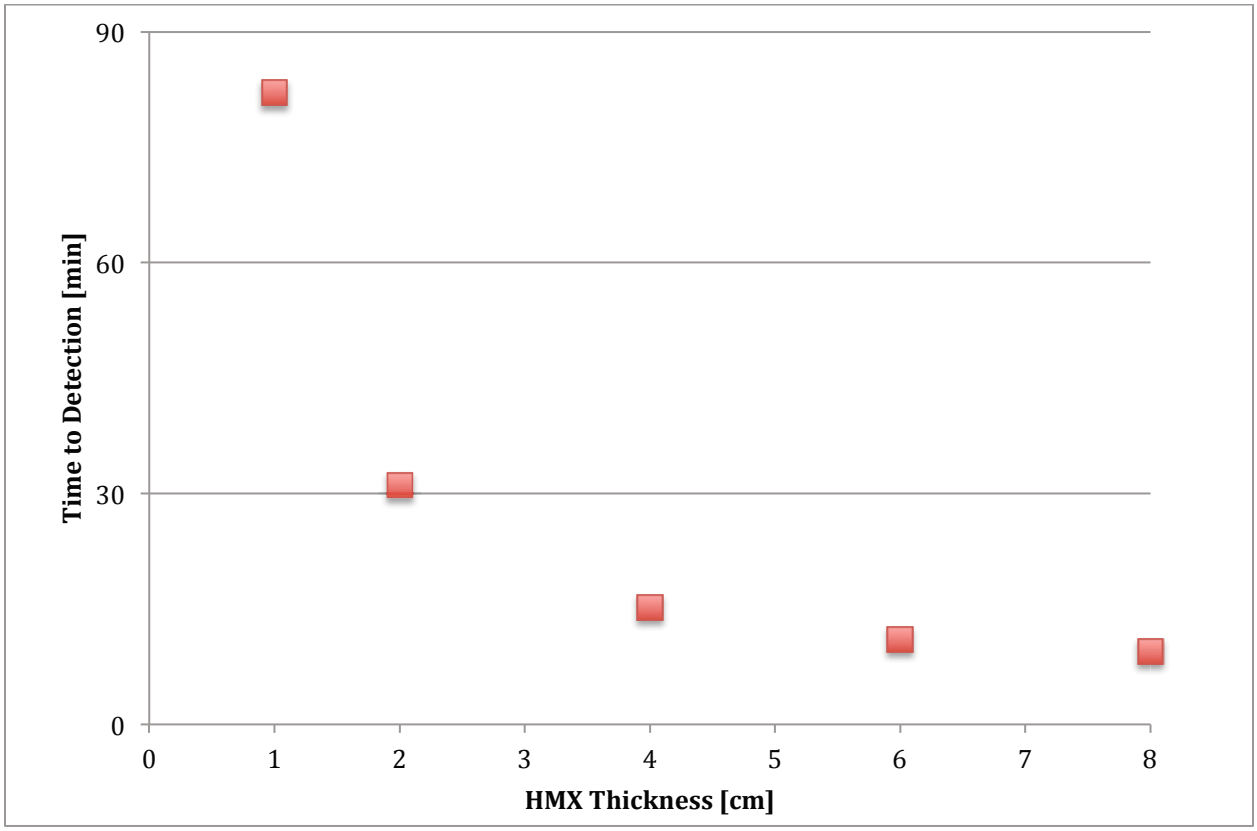

Figure 39. Time to detect HMX for absence measurements using NRF scattering. The time to detect for transmission measurements is not shown because all results exceeded 1000 minutes.

The time to detect hidden HMX during confirmation of absence measurements is shown in Figure 39. Only results for scattering are shown, as the transmission results were greater than 1000 minutes. Note that the observation of ^{14}N in HMX is used as the indicator for HE detection. If other nitrogen-bearing materials are present in the warhead, additional measurements looking at other isotopes (carbon, oxygen) might help to reduce the probability of false positives. The maximum MPS photons/shot required is 6×104, for 1-cm HMX.

II.3.6 Diversion Detection

The geometries considered for diversion detection consisted of 1.6 cm of Pb shielding surrounding the material of interest. This geometry has already been evaluated for SNM detection (see Figure 38). The geometry for HE detection in a diversion scenario has not been previously evaluated.

Simulation Results

Figure 38 shows the equivalent results for SNM detection in the diversion detection scenario. NRF scattering can confirm the presence of SNM down to 0.5 mm thickness in a little more than an hour using a single detector. Transmission measurements take considerably longer; even at 10 mm thick, the time to detect WGPu is longer than 90 minutes. Thus, scattering measurements prove to be more sensitive.

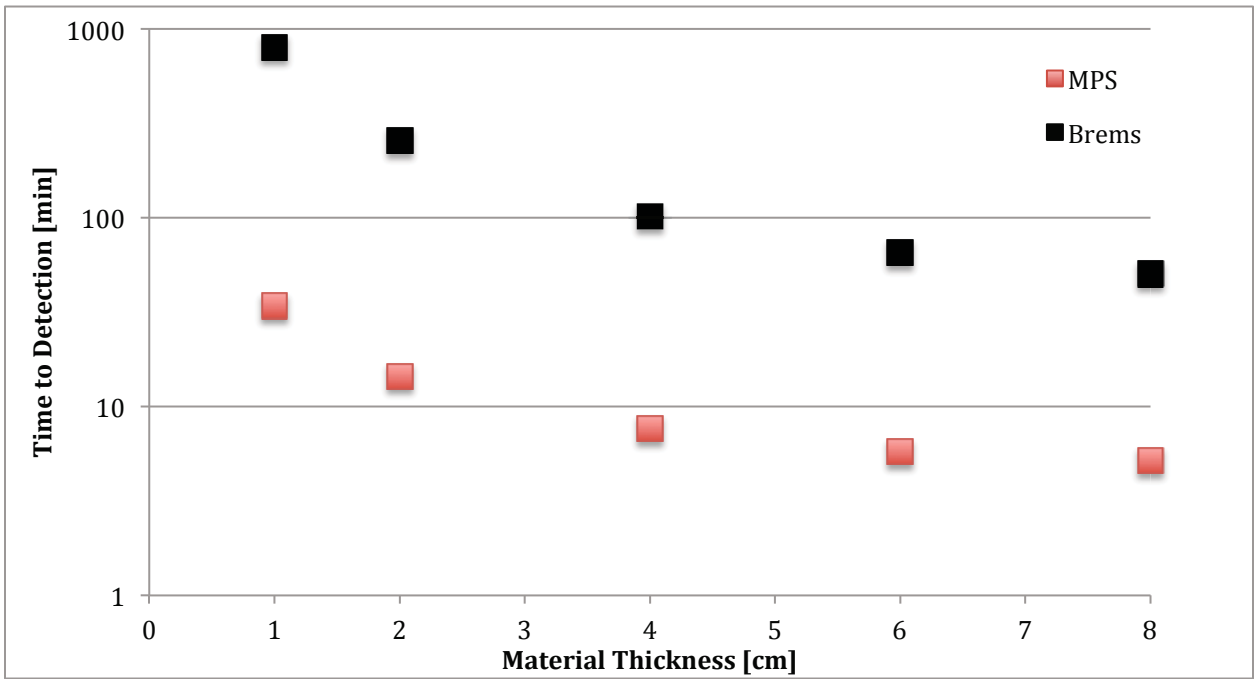

Figure 40. Time to detect HE in diversion detection scenario. Only results for scattering, both MPS and bremsstrahlung, are shown.

The time to detect HE in the diversion detection case is shown in Figure 40. HMX was used for the HE. Only results for NRF scattering are shown, because based on experience with dismantlement confirmation, the transmission approach is not sensitive enough to warrant consideration. Results for both MPS-based and bremsstrahlung-based photon sources are considered. Thicknesses down to 1 cm can be detected in less than 35 minutes using NRF scattering techniques with an MPS-based source; a bremsstrahlung-based source would require approximately an order-of-magnitude longer. The maximum MPS photons/shot required is $1 \cdot 10^5$, for 1 cm HMX thickness.

II.3.7 Impact on Treaty/Dismantlement Applications and MPS Requirements

Material characteristics and their effect on measurement setup in the context of treaty verification objectives of warhead confirmation, dismantlement confirmation and diversion detection have been evaluated considering both NRF scattering and transmission techniques using both MPS-based and bremsstrahlung-based photon sources. A summary of the results is presented in Table 16. Several high-level conclusions can be made. MPS-based photon sources provide an order-of-magnitude or more higher performance than bremsstrahlung-based photon sources. Measurements relevant to warhead confirmation would take minutes. In an hour, detection of mm-scale HE or sum-mm scale FM thicknesses could be accomplished, relevant to dismantlement. In shielded cases for diversion detection, verification of the absence of few-mm-scale thicknesses of FM, or cm-scale HE, is achievable. NRF scattering generally performs better than NRF transmission; the one exception is the test case for the confirmation of HEU in IO#5 which has relatively thick HEU. The shielding in the absence measurements makes these measurements more demanding; the assumed shielding is likely a worst-case scenario. It is important to note that the time-to-detection/confirmation are based on a single 80% relative efficiency HPGe; times could be reduced using additional detectors. The primary limitation to reducing the time-to-detection/confirmation

is the total rate on the detector; if the total rate is too high, pileup will occur obscuring the signal. Evaluation of different filtering options in front of the detector may improve that situation. Alternatively, if one could develop a fast threshold counting detector, it may be possible to significantly reduce the times-to-detection/confirmation. The photon source is assumed to be operating at 10 kHz with a 2% FWHM energy distribution and the photons intensity is relatively modest at less than $2 \cdot 10^6$ γ/shot. Because of the limitation on photon intensity to limit detector rate, the time to detection will be approximately proportional to the width of the energy distribution. For example, a 1% FWHM would reduce the times to detection by a factor of 2.

Table 16. Summary of Treaty Verification results. For Warhead Confirmation, the time to detect the material is listed, whereas for the other tests the minimum thickness of material that can be detected with a single 80% relative efficiency HPGe detector in one hour is shown. Thicknesses denoted with an "*" are the smallest thicknesses evaluated and are not limited by the measurement time.

Objective	Test	Geometry	Time/ Thickness	NRF Technique	γ/shot
Warhead Confirmation	HEU Detection	IO#5	3 min	Transmission	$2 \cdot 10^6$
	Pu Detection	IO#8	13 min	Scattering	$3 \cdot 10^5$
	HE Detection	IO#10	1 min	Scattering	$3 \cdot 10^4$
Dismantlement Confirmation	Presence HEU	Bare	0.1 mm*	Scattering	$1 \cdot 10^6$
	Presence Pu	Bare	0.1 mm*	Scattering	$1 \cdot 10^6$
	Presence HE	Bare	0.5 cm*	Scattering	$1 \cdot 10^6$
	Absence HEU	1.6 cm Pb Shield	1.4 mm	Scattering	$9 \cdot 10^4$
	Absence Pu	1.6 cm Pb Shield	5 mm	Scattering	$5 \cdot 10^4$
	Absence HE	3.75 cm PuAl	1.5 cm	Scattering	$6 \cdot 10^4$
Diversion Detection	Absence HEU	1.6 cm Pb Shield	1.5 mm	Scattering	$9 \cdot 10^4$
	Absence WGPu	1.6 cm Pb Shield	5.0 mm	Scattering	$5 \cdot 10^4$
	Absence HE	1.6 cm Pb Shield	1 cm*	Scattering	$1 \cdot 10^5$

II.4. High Resolution Imaging for Stockpile Stewardship

II.4.1 Introduction

The U.S. has an existing capability for conducting 3D imaging of its nuclear warheads. The Confined Large Optical Scintillator Screen and Imaging System (CoLOSSIS), located at Pantex, was designed to conduct 3D computed tomography on warhead and components with the goal of observing features on the scale of 50 to 75 μm [31]. In practice, it takes a week to collect the 1500 views that are then combined to form the 3D image. An MPS may be able to improve on this existing system in three ways: 1) achieve higher spatial resolution, 2) reduce measurement time which could increase throughput of inspections, and 3) reduce dose to the warhead. The first two improvements are significant drivers for investigating how an MPS-based system may improve on the existing bremsstrahlung-based capability. Two critical issues must be addressed in this evaluation: the relative intensities of the two systems and the differences in imaging.

An MPS-based photon source for stockpile stewardship may have a few advantages over the existing capability beyond the total photon flux. First, the narrow beam aspect of a Thomson MPS-based photon source may enable the reduction of scattering contributions in the image. For thick materials, scattering can be a significant contribution to the exposure for imaging. While bremsstrahlung beams are sometimes collimated to mimic a narrow angle source, this severely restricts flux. For a 0.56 mm^2 beam matching the MPS discussed here the flux of the bremsstrahlung system would be reduced more than 1000-fold (increasing scan time). Another potential advantage is the elimination of sagging correction for thick materials. The continuous energy spectrum of the bremsstrahlung beam requires a correction to properly reconstruct the 3D image due to the difference in attenuation for the different energies. A nearly monoenergetic photon beam would significantly reduce, if not eliminate, the need for that correction. Third, the small emission spot size of Thomson MPSs may enable higher spatial resolution. These possible enhancements motivate a more detailed evaluation of the potential benefit of MPS-based photon sources for stockpile stewardship.

II.4.2 Problem Definition: Imaging Intensity Requirements

For imaging measurements, the first challenge is achieving an adequate number of photons in order to achieve the necessary performance. Flux in excess of the current capability can be used to improve performance, for instance either reducing measurement time or increasing spatial resolution.

The major components of CoLOSSIS [31] are the linear accelerator, collimators, the imaging system, and the hardware and software to calculate the image. The linear accelerator provides a 9-MeV endpoint energy bremsstrahlung photon beam, which is collimated and directed onto the target 6.5 m away. The collimated beam delivers about 50 rads per minute at the target with a square cross sectional area of about 24 cm per side. The x-rays passing through the target strike a scintillator, which appears to be about 50 cm downstream of the target, and which converts the x-rays to green light. While the engineering of the imaging system is critical to the performance of CoLOSSIS, for the purpose of this evaluation we will assume similar detector performance for an MPS-based system so that it is not necessary to discuss the existing imaging system.

A comparison to current CoLOSSIS capabilities [31] indicates where a Thomson-based MPS [32] could offer performance advantages. With the given information on CoLOSSIS, we can estimate the photon flux at the target. If one assumes that the average energy of the 9-MeV bremsstrahlung beam is 3 MeV, then the fluence-to-dose scale for photons is approximately 10^{-11} Sv cm^2 [33]. This implies that 50 rad per minute, which is equivalent to 0.5 Sv for photons, corresponds to

$8.3 \cdot 10^8$ photons/cm^2/sec. If the imaging camera covers the full 24-cm-per-side square of the beam at the target and the average exposure time is 60 seconds, then the flux is $5.0 \cdot 10^{10}$ photons/cm^2/minute.

A high-repetition rate, high yield Thomson MPS-based photon source may provide similar photon flux density. The narrow-beam nature of the MPS-based source requires a slightly different approach to evaluating the time to achieve the same flux as CoLOSSIS. With a Thomson-based MPS there is a trade-off between energy spread and angle. For example a 4 MeV MPS photon beam with a 2% energy spread, 2 μm beam emission spot, 0.42 mrad divergence at 100 cm will cover an area of 0.56 mm^2. For 10^7 photons/shot, at 200 kHz repetition rate, it will take 28 shots to achieve the same exposure per area as a bremsstrahlung beam. As a result, it will take 21 seconds to achieve the same exposure across the entire 24-cm square area allowing for a 30% overlap in views. In other words, the described MPS photon source can provide three times the photon fluence at 4 MeV in the same amount of time as the current CoLOSSIS system. Note that the energy spread used here is very narrow, and hence the number of photons per shot is conservative relative to what is likely required for radiographic measurements. Other pairs of yield and rep rate could also be considered at similar performance (e.g. 10^8 photons/shot at 20kHz). And, even for a lower repetition rate MPS that does not deliver such high flux, the other advantages discussed below may be compelling.

II.4.3 Simulation Study Setup

A monoenergetic photon source may have favorable properties for imaging, and in particular for quantitative imaging techniques such as tomography, which is used for stockpile stewardship. The comparison above indicated that the MPS should be capable of equivalent or even greater usable flux than a 9MV LINAC system currently available. Here, we describe models in MCNP of both a 9MV linac system with a bremsstrahlung spectrum, and a potential laser-plasma based Thomson monoenergetic photon source (MPS). We performed a resolution test to determine whether the smaller emission spot of the MPS is likely to offer the enhanced image resolution predicted by geometric optics. A penetration test is also conducted to estimate relative amounts of beam hardening and scatter between the two sources. These effects interfere with quantitative measurements such as tomographic reconstructions. We find that the MPS offers greatly enhanced spatial resolution compared to the LINAC, that it eliminates beam hardening, and that it significantly reduced scatter (due to the small opening angle). All these results indicate that the MPS should offer higher resolution tomography measurements with reduced artifacts.

Radiation transport modeling was conducted to evaluate the emission spot and penetration tests. An MCNP model was developed to represent high resolution imaging with a LINAC source, see Figure 41. For the purpose of comparing the potential advantage of bremsstrahlung-based sources and MPSs for high-resolution imaging, a perfect detector has been assumed; the focus is on the nature of the photons reaching the detector. Although developing an efficient high-resolution detector is a large topic in itself, here we focus on limitations to imaging due to the source only. We model flux using a radiography tally with a length scale chosen to easily represent the object of interest.

The LINAC system is modeled on a Varian 9 MV Linatron. The LINAC has a variable focal spot size; for high-resolution imaging we assume 1 mm focal spot, although this would require a reduction in the overall flux from the peak rate. This is represented by an area source 1 mm in diameter from which particles are thrown. A large standoff distance based on approximate CoLOSSIS geometry, 6.5 m from source to test object, is needed to reduce the geometric blurring from the mm-scale LINAC spot size. Three tungsten collimators along the beam path limit the contributions due to scatter. A nominal detector is placed 90 cm behind the test object.

The MPS source has a distinctive energy-angle dependence, as shown in Figure 42, and a 1 μm sized emission spot [32]. Note that while much smaller than that of the linac, this emission spot size

is conservatively large for laser-plasma based Thomson sources. Plasma based beam sizes down to 0.1μm have been measured. The MPS properties were represented in the MCNP model by using a custom SDEF card. No cutoff was used in either energy or radius, although only the central portion of the beam was used in testing. In order to compare the effects of source characteristics on imaging, the MPS was modeled using the same geometry as the LINAC. The angular divergence of the MPS beam is very small, such that only a few mm are illuminated even at a distance of 6.5 m. In order to image a large field of view, the beam must be rastered. For the purposes of this investigation, we assume that this could be done.

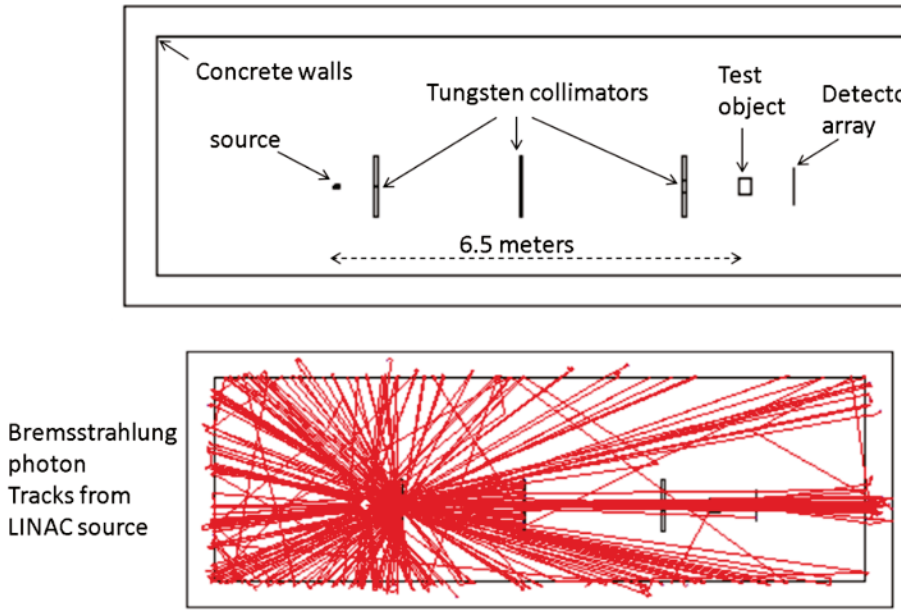

Figure 41. Modeled geometry (top) and example of bremsstrahlung photon tracks from the LINAC source (bottom).

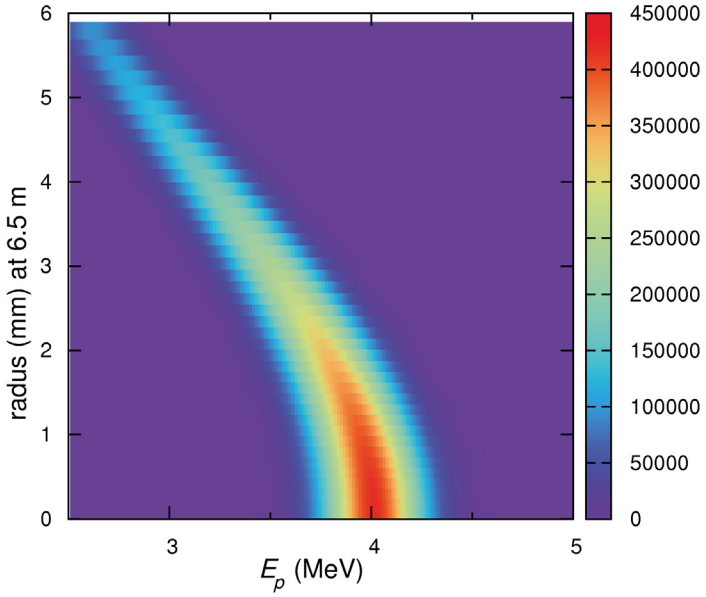

Figure 42. Energy-radius distribution of the Thomson scattered source 6.5m downstream, showing the angular dependence of the spectrum.

II.4.4 Simulation Results: Resolution Test

According to geometric optics, the 1 μm effective spot size of the MPS should offer the possibility of greatly enhanced spatial resolution as compared to a LINAC, which typically has a focal spot size of a few mm (as little as 1 mm, but with decreased flux). However, given the extreme geometry, it is unclear whether this can be expected to hold in the presence of scattering in a real measurement. In a typical imaging setup, resolution can be limited by either the source or the detector. We assume that the detector resolution is arbitrarily fine, and focus on the limitations posed by the source alone.

ANSI N42.46 offers a set of standards for cargo radiography, which is an example of a high-energy imaging application [34]. In this standard, spatial resolution is measured using a set of three steel bars, of width *d*, spacing *d*, and thickness *d*, where *d* is varied from several cm's to mm's. For this application, we are interested in resolution well below 1 mm. For bar thicknesses below 1mm, the attenuation is negligible, so we fix thickness at 1 mm and use tungsten as the material. As seen in Figure 43, 200 μm features are clearly resolved with a 1 mm focal spot on the 9 MV LINAC, but 100 μm is more challenging. Anything below about 60 μm is not resolved. Using the same geometry with the MPS as shown in Figure 44, a 1 μm feature size is clearly resolved. In this case the 6.5 m standoff distance is unnecessary, but was used for consistency. By reducing standoff, a MPS source in this case could enable a more compact setup in addition to higher resolution.

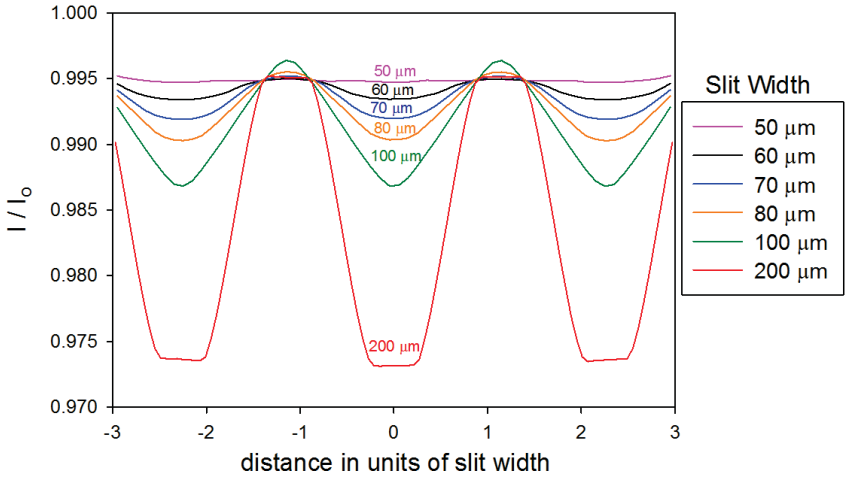

Figure 43. Normalized intensity profile for the LINAC system across a 3-bar resolution test object with varying dimension d. Bar depth is 1 mm in all cases.

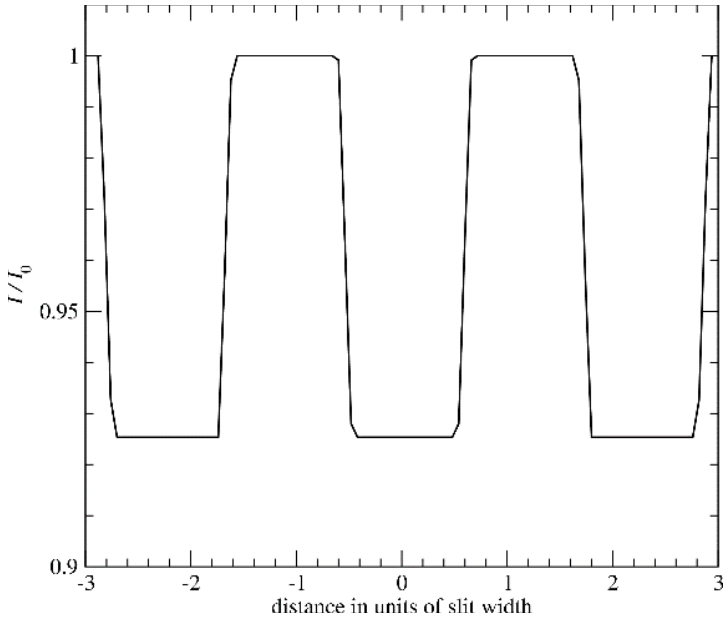

Figure 44. Normalized intensity profile for the MPS system across a 3-bar resolution test object with slit width 1 μm and depth 1 mm.

II.4.5 Simulation Results: Penetration test

For the penetration test, we examined the relative intensity as a function of thickness behind a solid tungsten block that covers approximately half the field of view. This is an imperfect measure of scatter as the amount of scatter depends on the details of the environment. However, by holding the environment constant while varying the source definition, we are able to compare the performance of the two sources. In medical imaging, scatter of a system is typically defined as the limiting value as the radius of a thick object is reduced to zero [35].

Figure 45 shows relative intensity as a function of thickness under several conditions. For reference, the solid line indicates $e^{-\mu x}$ for tungsten at 4 MeV. The bremsstrahlung beam, shown in blue circles, initially drops off faster in intensity and then flattens out at around 4 cm. Two different effects contribute to the nonlinear behavior: beam hardening, as lower energy portions of the spectrum are preferentially attenuated, and scatter, which contributes additional intensity. To distinguish these two effects, we also plot the transmitted intensity for the primary beam only, shown as red circles. The initial faster falloff persists, as the softer components of the spectrum are more heavily attenuated. It should be noted that for qualitative imaging, this effect can be beneficial: small, less attenuating features are more easily observed, while still maintaining penetration for larger objects. However, this effect interferes with quantitative techniques, such as tomography. The nonlinearity in the primary-only results is much less than in the total, indicating that scatter plays a large role in the nonlinear behavior as the tungsten thickness increases.

For comparison, we also plot the transmitted intensity for the MPS, in green circles. The MPS is highly linear down to approximately 10 cm of tungsten, and then begins to flatten out, presumably due to scatter. The MPS does not suffer from beam hardening due to its much narrower spectrum, and because of the small beam divergence illuminating very little outside the object, scatter effects are considerably reduced. Note that no collimator or cutoff is assumed on the MPS beam at large angles/lower energies. Such a collimator might further improve performance.

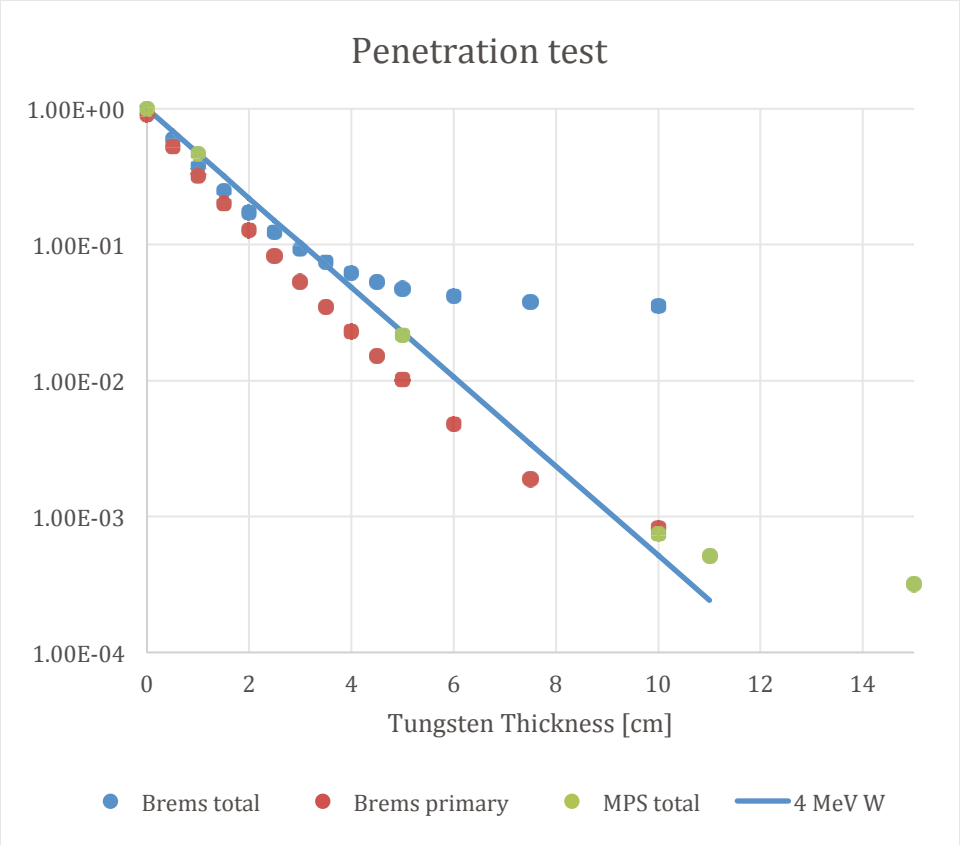

Figure 45. Transmitted intensity as a function of tungsten thickness in cm.

II.4.6 Impact on Application and MPS Requirements

We have seen that with the current geometry, the MPS would readily support micron-scale resolution. There is no indication that factors other than geometric spot size overwhelms the benefits of the small spot size, although very thin objects may suffer due to low contrast in the high-energy beam. A 6.5-m standoff is not needed for the MPS from the viewpoint of spatial resolution.

Both beam hardening and scatter produce artifacts in tomography, which relies on an assumption of logarithmic attenuation. In the case of beam hardening, artifacts known as "cupping" are produced, where the attenuation in the middle of an object appears to be lower than the outer regions [36]. This can be corrected via dual-energy imaging, or if the object material is already known, but in general will interfere with high quality quantitative tomography reconstructions.

Artifacts due to scatter are similar to beam hardening – inner and outer regions of an object appear to have different attenuation due to the relative contribution of scatter to the projections. Without correction, scatter-to-primary ratios (SPRs) as low as 0.05 to 0.10 can impair reconstruction [35]. This is a serious issue at high energies, and in fact the SPR for the LINAC system is around 0.10 even before an object is present. Various methods are possible to reduce or mitigate scatter, either by physically reducing it or by estimating its magnitude via modeling, but it is notable that the low-divergence beam geometry of the MPS is advantageous in reducing these artifacts.

The small spot size of the MPS might be most efficiently used for high-resolution imaging in a magnified geometry, where the object is near the source and the detector further away. A steered

beam with low divergence may be used for a magnified geometry, although some oversampling may be necessary at the front of the object in order to ensure coverage at the back. A diverging beam could be beneficial for magnified imaging, at the expense of increased scatter and increased spectral bandwidth. This would require further study to evaluate.

While the resolution tests suggest that an MPS can achieve 1 μm resolution, there are other constraints that will limit the spatial resolution. The resolution evaluation was done with an ideal detector, so detector resolution is one such constraint. This concern could be relaxed if a magnified geometry is used.

Another constraint is the transmitted flux delivered to the detector. Assuming the same number of photons per pixel is required for an MPS-based imaging system as the current CoLOSSIS, the improvement in resolution may be limited by the relative intensities of the two systems. For instance, the 2% energy width 200 kHz MPS-based system, which could provide roughly 3 times the photons per unit area per unit of time as CoLOSSIS, would enable the reduction of the spatial resolution by a factor of almost 2 compared to CoLOSSIS for equal exposure time. This estimate is conservative, as the reduced scatter and hardening effects may enable the resolution of even smaller features in equal time. Use of longer exposure time to increase flux delivered per pixel would allow the MPS based source to reach its full potential resolution.

The initial calculations and modeling for imaging of nuclear warheads as part of stockpile stewardship program using MPS-based system suggest that there could be significant improvements compared to the existing bremsstrahlung-based solution. These improvements could be leveraged to improve some combination of spatial resolution and measurement throughput, depending on what would be most beneficial. If the focus is on resolving smaller spatial features, an MPS-based system has the potential to reduce the size of observable features by a factor of 2 or more in equal exposure time, and potentially to achieve micron-scale resolution with longer exposure time compared to CoLOSSIS. The primary conclusion from this effort is that it would be worthwhile exploring the feasibility of this approach with higher fidelity modeling.

High resolution imaging for stockpile stewardship may provide a valuable tool for treaty and dismantlement verification involving nuclear warheads. Discussions with stakeholders in these communities identified a strong interest to ‘fingerprint’ individual weapons by deriving an intrinsic unique identifier (I-UID). High-resolution imaging may provide that I-UID. For instance, the rotation of various screw/bolt heads may serve as the non-sensitive fingerprint to form an I-UID. It would be necessary to demonstrate that imaging can be performed on non-sensitive components of a warhead without revealing any sensitive information. If an MPS-based system were already used in stockpile stewardship efforts, familiarity with the technique and experience using it on the stockpile would ease the transition for use in treaty verification. The driver for using an MPS-based system for this application is the higher flux, better imaging resolution, and lower imaging artifacts, which could enable shorter measurements, typically an hour at most, required by treaty verification.

II.5. Spent Nuclear Fuel Dry-Storage Cask Content Verification

II.5.1 Introduction

Dry cask storage has proven to be effective for safely storing spent nuclear fuel (SNF) for relatively long periods of time, until a permanent solution is available, and many countries have adopted dry storage systems as an option to store their SNF. The IAEA is actively pursuing a method that allows re-verification of LWR spent fuel stored in dry casks without the need for a reference baseline measurement or fingerprinting [1]. Here we understand "re-verification" to mean the verification that all SNF assemblies are present. This is a challenging problem because dry storage casks are large cylinders that can hold 24 or more pressurized water reactor (PWR) or 68 boiling water reactor (BWR) assemblies, and have walls and lids made of thick steel and additional neutron shielding or of thinner steel and a thick concrete overpack. Two examples of dry storage casks are shown in Figure 46. A full discussion of the state of the art, including references, is presented in [1], and is summarized here.

The canisters are often stored upright in rows with several meters in between casks. In other storage facilities dry casks are stored horizontally in above-ground concrete bunkers and would likely need to be pulled out to gain access for measurements. Re-verification is expected to be performed infrequently, so rather long measurement times – hours or possibly longer – are likely acceptable.

The thick walls of dry storage casks and the additional attenuation and scatter in the stored assemblies make radiographic measurements for the verification of the canister content very challenging. Conventional radiography with a broad-beam bremsstrahlung source cannot be used because the very large scatter contribution makes it impossible to achieve sufficient contrast. The scatter contribution can be greatly reduced or to first order eliminated, and thus the contrast drastically improved, in transmission measurements with a small-diameter ('pencil') photon beam. This offers the possibility to scan the cask with a high-flux 'pencil' beam, measuring the transmitted photon flux. Along a line through an unoccupied storage position the transmission would be significantly increased and the absence of an assembly detected.

Scanning a spent fuel cask by measuring the transmission lengthwise through the cask, i.e. with the beam parallel to the fuel rods, is the simplest approach for determining if an assembly position is filled or empty. Transmission through an empty slot would be significantly higher than through an assembly as the fuel rods absorb and scatter the beam. With a fill factor on the order of 50% for an intact fuel assembly, the transmitted photon flux averaged over the assembly cross section would be two times higher for the empty slot. With a beam diameter close to that of a fuel pin, i.e., 1 cm or smaller, individual pins could be resolved with very high contrast and scanning across a target position could not only reveal the presence or absence of an assembly but also detect missing pins.

A lengthwise transmission measurement is a good match for horizontal casks, but for upright casks the detector would need to be placed underneath and the MPS moved across the top for performing transmission measurements. Because the casks can weigh ~100 tons and are hard to move, a lengthwise measurement on upright casks may not be practical and transverse measurements have to be considered. The presence of fuel bundles in the cask can in principle be verified by a limited number of transmission measurements that probe all assembly positions. Because the pins in an assembly are arranged on a lattice and the assemblies in the cask are typically lined up in rows and columns, with narrow gaps in between, a more detailed assessment of transverse scanning is required to find best scanning techniques and determine capabilities.

Bremsstrahlung beams can be tightly collimated but the photon flux generated with available electron linacs is insufficient for penetrating a cask filled with fuel bundles. A high power (9 MeV, 10 mA) Rhodotron accelerator could produce a time-averaged bremsstrahlung photon flux in a few mrad divergence beam that is comparable to the flux of a Thomson source but discrimination against the radioactive background would likely not be possible. The typical cw operation of a Rhodotron would preclude detector gating such as could be used with a Thomson source and the broad energy spectrum with the highest photon flux at background energies would make energy discrimination very challenging. In addition, a Rhodotron is a large and heavy accelerator that would make transport to and positioning next to a dry-storage cask impractical.

A Thomson MPS offers several advantages that could enable transmission measurements for detecting and locating empty vs. full assembly storage positions in a dry storage cask. Most importantly, such sources produce low divergence photon beams and are expected to deliver a high flux on target, suitable cm-scale photon beam spot sizes, and high repetition rates. Our preliminary analysis [1] indicated that photon transmission measurements with high intensity beams of 6-8 MeV photons and with a small divergence of several mrad could verify the content of a spent fuel dry-storage cask. Based on analytical calculations, unscattered photon transmission probabilities lengthwise through a cask of 10^{-7} to 10^{-10} were estimated for a range of lid and bottom thicknesses. This indicates that longitudinal measurements could be performed with beam intensities on the order of $1 \cdot 10^{11}$ ph/s.

The simulation study section below presents higher-fidelity calculations and modeling results to evaluate "re-verification", i.e., to verify that all SNF assemblies are present. The section begins with a high-level summary of the decision criteria and observable signals. Subsections quantify capability for various cask orientations, types and scan possibilities.

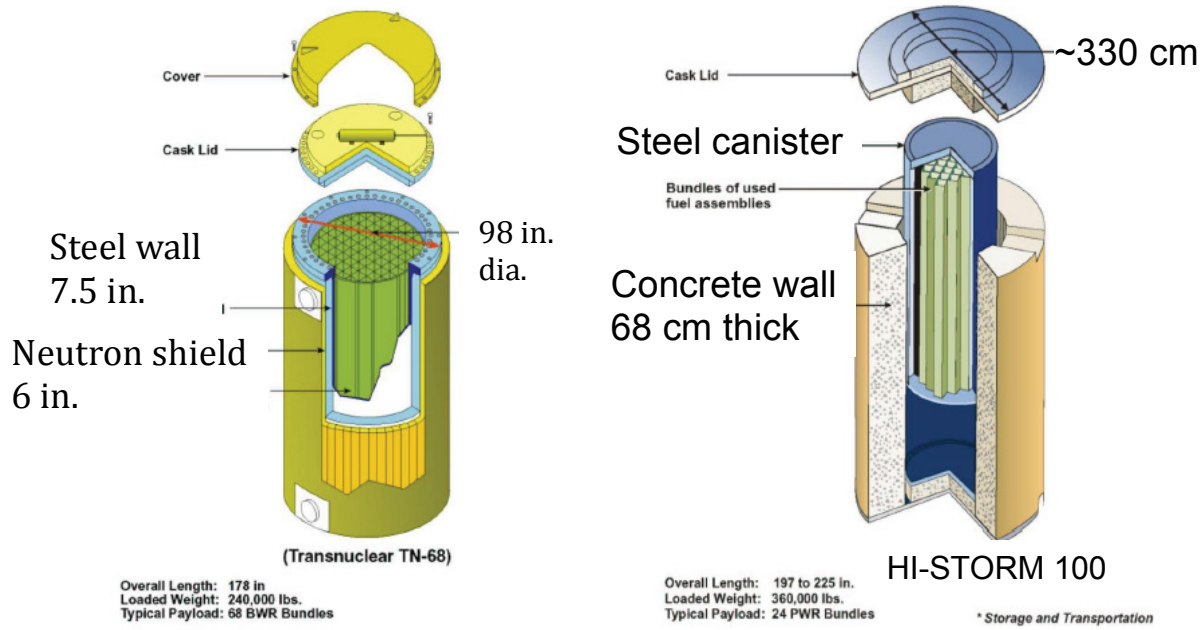

Figure 46. Two dry storage cask types. On the left is a Transnuclear TN 68 cask with a thick steel wall and a neutron shield; on the right is a HI-STORM 100 cask consisting of a steel cylinder in a concrete overpack.

II.5.2 Simulation Study Setup

Detailed transmission calculations and radiation transport simulations were conducted to establish feasibility of performing scans through casks of different designs that would reveal partial loading or a missing assembly. Backgrounds, which constrain detection performance, were first analyzed. Calculations were then conducted for transverse and longitudinal scanning. The calculations were more extensive for analyzing the transverse transmission approach because of the strong beam attenuation by the assemblies and the inhomogeneity and structure of the spent fuel assemblies. In order to more accurately estimate transmission probabilities for various beam positions through cask and assemblies and to include scattering effects, detailed MCNP simulations were performed.

The spent nuclear fuel gamma-ray background seen on the outside of the cask by the transmission detector could impact measurement sensitivity and photon flux requirements. The background was estimated using the codes ORIGEN [37] for calculating fuel depletion and MCNP [38] for modeling the radiation transport. The simulation was done for PWR fuel bundles from the Diablo Canyon Power Plant with a cooling time of 3 years. [39] Because 3 years is the earliest spent fuel can be placed in a dry storage cask, this is the worst-case background intensity. In practice, the loss of continuity of knowledge and need for re-verification is more likely to occur for older casks that have stored fuel for many years and due to the longer spent fuel cooling times the background is greatly reduced. For the background simulation the cask was assumed to be filled with a homogenized mixture of 24 assemblies. Photons with energies from 0.25 MeV to 3.5 MeV (the highest energy photons emitted from spent fuel) were transported through the cask and the flux on the 5 cm x 5 cm face of the detector, located at the 22.86 cm steel bottom of the MC-10 cask as shown in Figure 48, calculated. Figure 47 shows the simulated energy spectrum at the detector. The energy-integrated background rate is ~2,400 counts per second. The pulse structure of a Thomson source with its sub-picosecond duration beam pulses at repetition rates in the kHz range enables rejection of the passive spent fuel background by gating the photon transmission detector with the beam, i.e., by rejecting counts between beam pulses. Assuming a gate width of 4 ns, conservative for a fast scintillation detector, and a 10 kHz pulse repetition rate, the gated background rate is ~0.1 counts per second. Because this rate is well below the lowest transmission signal one would expect for either longitudinal or transverse scans (see estimates below), the radioactive background from the spent fuel is not expected to impede transmission measurements.

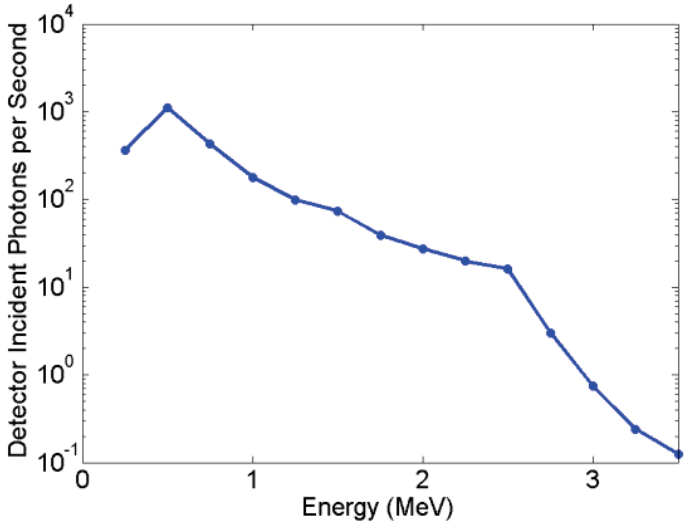

Figure 47. Simulated spent fuel background spectrum outside cask.

In addition to detector gating an energy threshold could be applied at low transmission rates, for which single photon counting is possible. An energy threshold of 3 MeV would eliminate the background since almost all gammas from the radioactive decay of the spent fuel have energies below that threshold as seen in Figure 47. However, operating in single photon counting mode and applying an energy threshold does not seem necessary. Cask background does not appear to be a significant restriction on measurements for pulsed, narrow emission angle MPSs such as Thomson sources.

I.5.3 Simulation Results: Longitudinal Transmission Scan

MCNP simulations were performed to evaluate longitudinal cask measurements. The simulations take into account beam divergence and assembly geometry, and include photon scattering. In a lengthwise transmission measurement the beam needs to penetrate the lid and bottom of the cask, and the beam attenuation depends on their combined thickness. The lid thickness varies significantly across different cask types, and the combined lid and bottom thickness ranges from ~60 cm to ~100 cm of steel. Un-scattered photon transmission probabilities for an empty storage position range accordingly from $\sim 1 \cdot 10^{-6}$ to $1 \cdot 10^{-10}$. Transmission values for casks with a concrete overpack also fall within this range. Calculations established that transmission is maximized for ~8 MeV photons. The simulations were performed for a simplified MC-10 cask and a 17x17 PWR assembly but results can be extrapolated to casks with different lids and bottom plates by simply taking the change in attenuation into account.

An 8 MeV, 30% FWHM photon beam with a spatial divergence of 3.5 mrad, representative of candidate Thomson photon sources (tuned for high photon yield instead of narrow energy spread), was transported through the simplified MC-10 cask [40], which had a combined thickness of ~60 cm of steel in the lid and base attenuating the beam. The transmission was simulated for a beam through an empty slot (no assembly) and through a 17x17 PWR assembly [41] with representative pins [39]. The transmission through the assembly was calculated for three different beam locations corresponding to the beam being centered in the gap between pins, in a guide tube, and on a pin as indicated in Figure 48. For the chosen divergence of 3.5 mrad, the beam diameter of ~ 2 cm at the far end of the assembly is smaller than the assembly width but larger than a single pin. In the simulated geometry (Figure 48) the transmitted photons are detected by a 5 cm cube detector that is positioned in line with the beam underneath the cask. Tallied was the number of photons on the front surface of the detector. The detector response was not simulated.

Figure 49 shows the energy spectra of the photons reaching the detector for the four simulated cases. The spectra are dominated by the broad peak around the beam energy, i.e., by the unscattered photons. The spectrum for the beam centered on a pin is not visible in this figure because the transmission probability is three orders of magnitude less than in the other cases. The probabilities for a photon being transmitted are listed in Table 17. Without an assembly in the beam's path the transmission probability is simply determined by the thickness of lid and bottom. With an assembly in place and the beam centered on a gap or a guide tube the transmission is reduced by about a factor of two. If the beam is centered on a pin, the transmission is more than 1000x lower because the beam photons cannot transmit lengthwise through the pin. For beams centered in between these positions the transmission probabilities are in between the extreme values. Because the transmission differs by at least a factor of two, empty assembly slots can easily be identified. If the beam were scanned across an assembly in sufficiently small steps, a single missing pin could be detected.

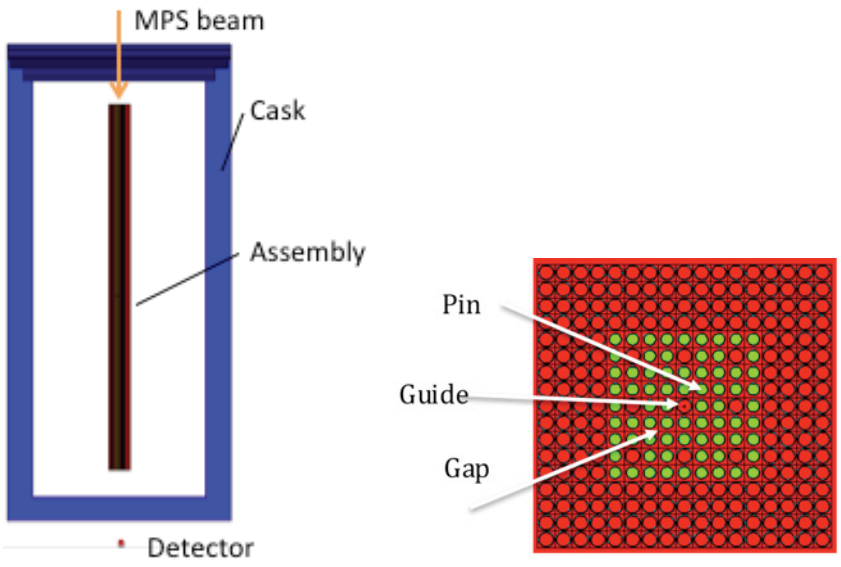

Figure 48. Geometry for MCNP simulation of the photon beam transport through cask with steel lid and bottom (MC-10). The beams enter from the top and are positioned on the assembly as shown on the right. The green dots indicate the pins included in the simulation. The 5 cm cube detector is positioned underneath the cask.

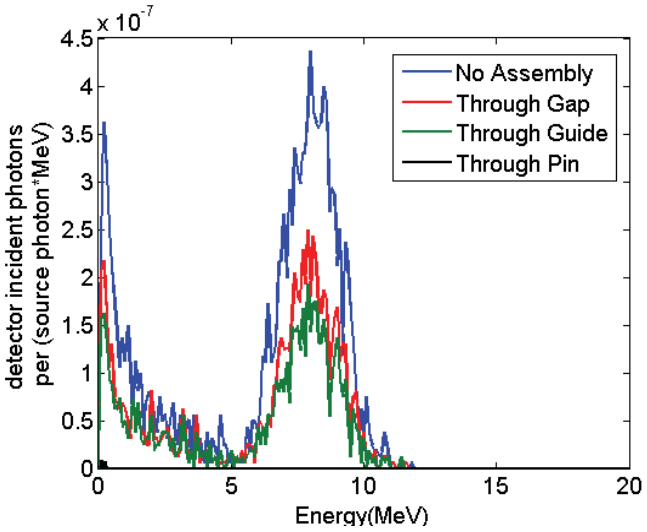

Figure 49. Transmitted photon spectra for the four simulated cases. The dashed black line, which represents the photon spectra for the beam centered on a pin, is not distinguishable from the x-axis because the transmission probability is three orders of magnitude less than in the other cases.

Table 17. Number of photons per source photon entering the detector for longitudinal measurements through an MC-10 cask.

No assembly	Through gap	Through guide	Through pin
1.4×10^{-6}	7.6×10^{-7}	5.7×10^{-7}	4.5×10^{-10}

I.5.4 Simulation Results: Transverse Transmission Scan

While probing the assembly occupancy of a cask with longitudinal beams is the simplest approach, it may not always be practical. Most casks are standing upright making it difficult to place source and detector above or underneath the cask. Moving the cask to an orientation where longitudinal scanning can be accomplished may be undesirable. In these cases scanning with a transverse beam would be necessary. Various methods for accomplishing this with a near-monoenergetic, narrow-divergence beam were modeled using analytic calculations. The attenuation along lines through cask and assemblies was calculated based on mass attenuation coefficients [42] for the given geometry and materials. These analytical calculations did not include scattering or the effects of beam divergence. The analytical results were then validated against MCNP simulations, which do include scattering, for representative cases. This allowed analysis of a broad range of cases, while mitigating the required computation time.

Various scanning configurations and methods were investigated using analytic calculations for a simplified MC-10 all-steel cask and for HI-STORM casks (Figure 46) that have a concrete overpack. Figure 50 shows the cross section of the MC-10 cask with a steel wall of 25.4 cm and loaded with 24 17x17 PWR assemblies. The labeled assemblies were removed individually for different scans, so that discrepancies in the transmission map could be observed. Calculated was the attenuation through the cask for 55 beam chords to build up a transmission profile. The beams were scanned across the cask in several different patterns. Either the cask was scanned with parallel beams at a fixed angle in respect to the assemblies or with beams that originated from one spot (fixed source location) and traversed the cask at changing angles. Note that the later is more straightforward for MPS operations. Two examples are illustrated in Figure 51, corresponding to source translation or rotation. The calculated transmission probability profiles are shown in Figure 52.

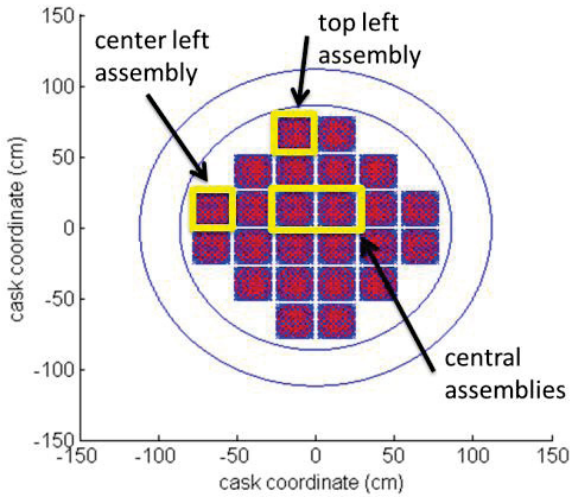

Figure 50. Simplified MC-10 steel cask model (blue outline) with 24 PWR assemblies, each 17×17 pins. The labeled assemblies (outlined in yellow) were removed individually to determine differences in attenuation for a missing assembly.

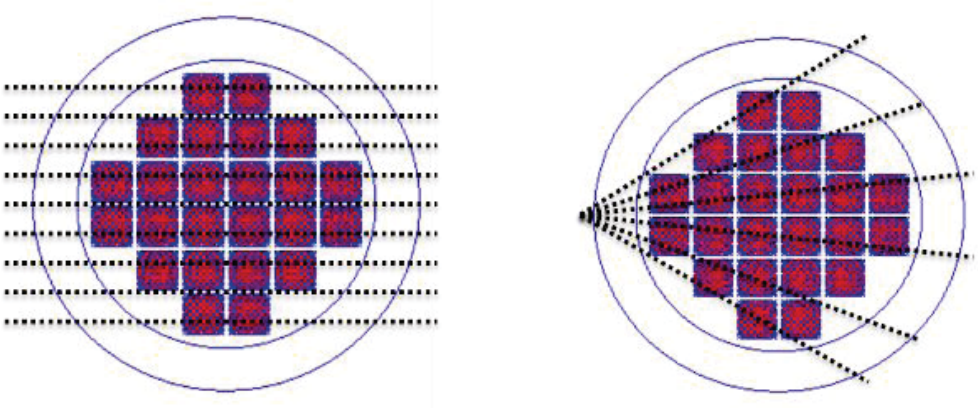

Figure 51. “Parallel” scan (left) and “fan” scan (right); the number of illustrated beams is reduced for clarity.

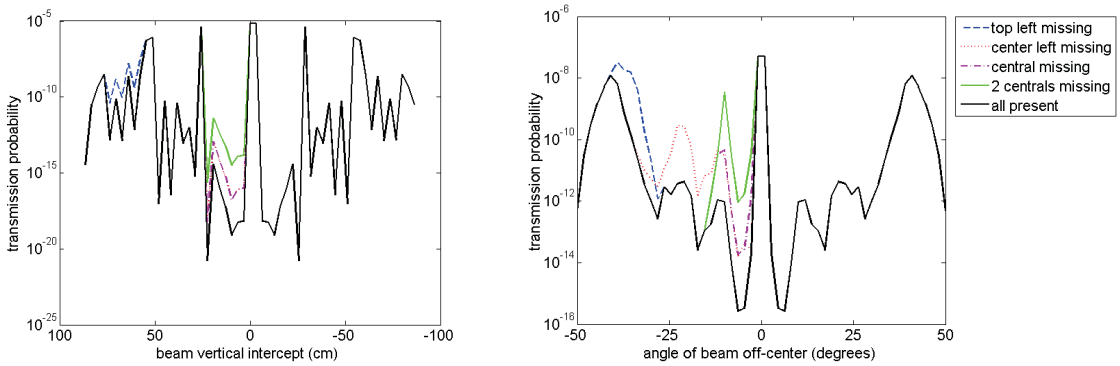

Figure 52. “Parallel” (left) and “Fan” (right) scan transmission probability maps. The black lines show the transmission probabilities with all assemblies in place. The colored lines give the transmission values with specific assemblies removed as indicated in the legend.

For the “parallel” scan the transmission varies over many orders of magnitude depending on how the beam lines up with the rows of pins in the assemblies. With removal of an assembly the transmission increases roughly an order of magnitude but stays well below $1x10^{-12}$, which is considered the lower limit for transmission measurement as explained below, for the central part of the cask. A rotated parallel scan for which the beams do not align with the rows of assemblies and pins gives better results, but for certain configurations the transmission through the center of a cask can still be very low.

Generally, better results are achieved with a “fan” scan such as illustrated in Figure 52. Over a range of source positions and “fan” beam orientations beams that align with rows of fuel pins can be avoided and the transmission through cask and assemblies measured. In order to determine source positions and fan beam orientations that give the best results, calculations were performed for “fan” scan orientations in 5 degree increments up to a 45 degrees as illustrated in Figure 53. Transmission probabilities were calculated for the fully loaded cask and for cases with some assemblies removed as indicated in Figure 54. Figures 55 through 58 show the transmission profiles for several source orientations. For source positions between 225 and 205 degrees the transmission probability increases by an order of magnitude in the case of a missing assembly to above the measurable probability of 10^{-12}. This indicates that the measurement would be sensitive to a missing single assembly in any location.

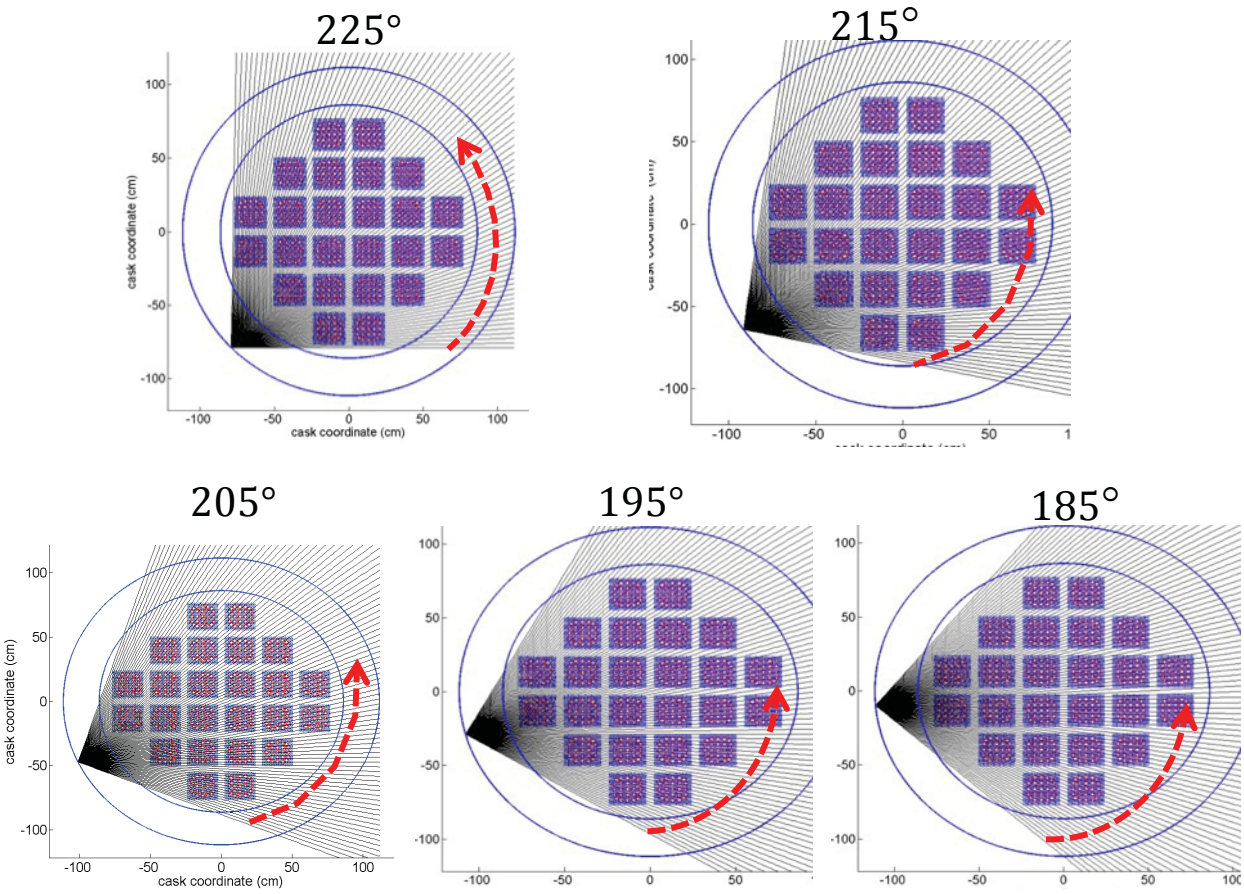

Figure 53. Analyzed source orientations for "fan" scans of an MC-10 cask.

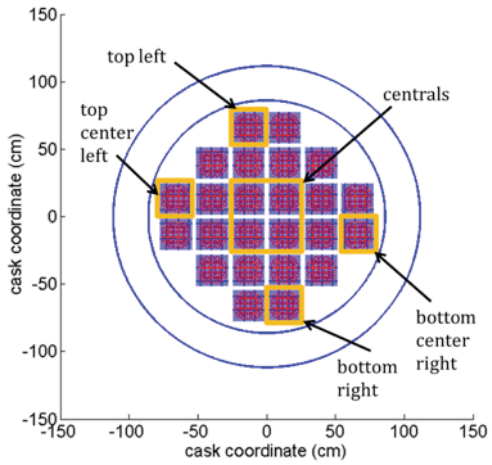

Figure 54. Assemblies marked in yellow were removed as indicated in the transmission profile graphs below.

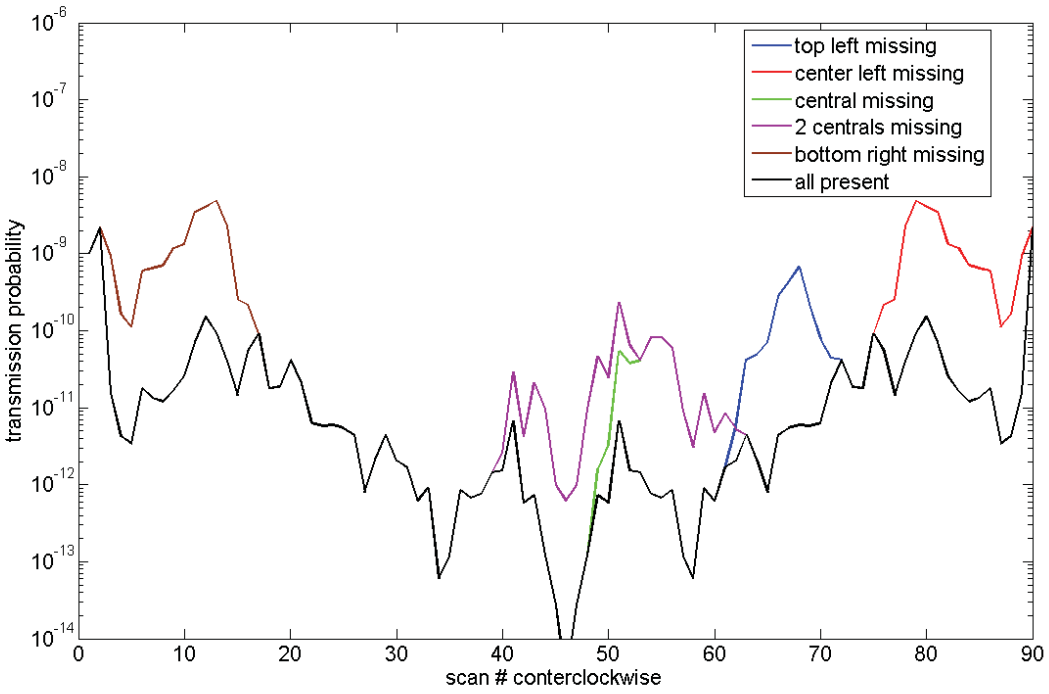

Figure 55. Transmission profiles for "fan" scans of a MC-10 cask with the source at 225 deg. The black lines show the transmission probabilities with all assemblies in place. The colored lines give the transmission values with specific assemblies removed as indicated in the legend.

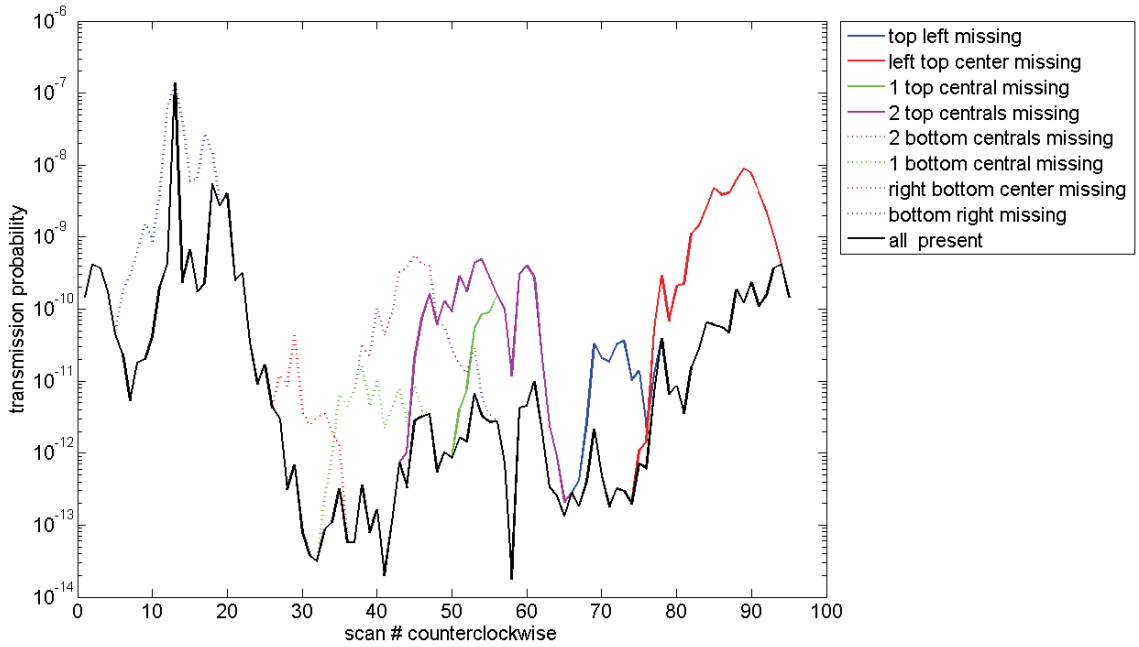

Figure 56. Transmission profiles for "fan" scans of a MC-10 cask with the source at 215 deg. The black lines show the transmission probabilities with all assemblies in place. The colored lines give the transmission values with specific assemblies removed as indicated in the legend.

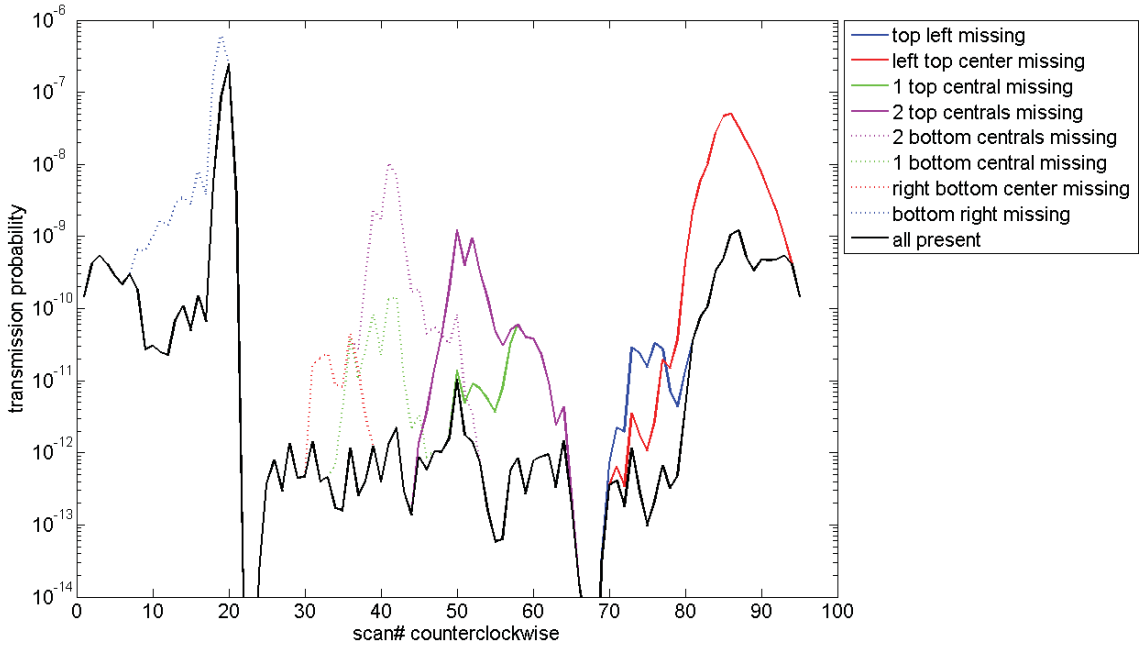

Figure 57. Transmission profiles for "fan" scans of a MC-10 cask with the source at 205 deg. The black lines show the transmission probabilities with all assemblies in place. The colored lines give the transmission values with specific assemblies removed as indicated in the legend.

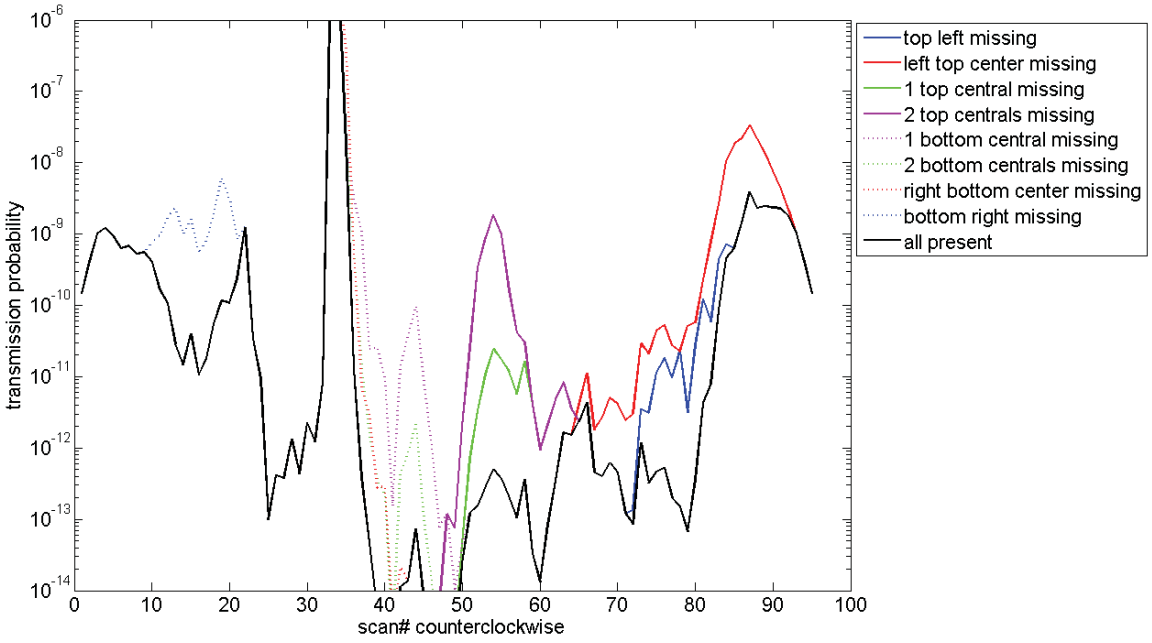

Figure 58. Transmission profiles for a "fan" scans of a MC-10 cask with the source at 195 deg. The black lines show the transmission probabilities with all assemblies in place. The colored lines give the transmission values with specific assemblies removed as indicated in the legend.

In addition to the analysis of transverse scans of a MC-10 cask, calculations were performed for a model HI-STORM 100 cask with two different loadings of 32 PWR assemblies and 68 BWR assemblies as shown in Figure 59. This is a different type of cask in which the assemblies are stored in a steel cylinder with relatively thin walls that is then placed into a concrete overpack. The transmission profiles for 205 deg. "fan" scans (Figures 60 and 61) indicate, similarly to the transmission profiles for the MC-10 cask, that the transmission probabilities increase by more than an order of magnitude for the MPC-32 loading and by a factor of a few for the MPC-68 loading if an assembly is missing. In both cases the transmission probability is higher than 10^{-12} when an assembly is missing and measurements could be performed in acceptable times as discussed below. As in the case of the MC-10 cask, the measurement would be sensitive to a missing single assembly in any location.

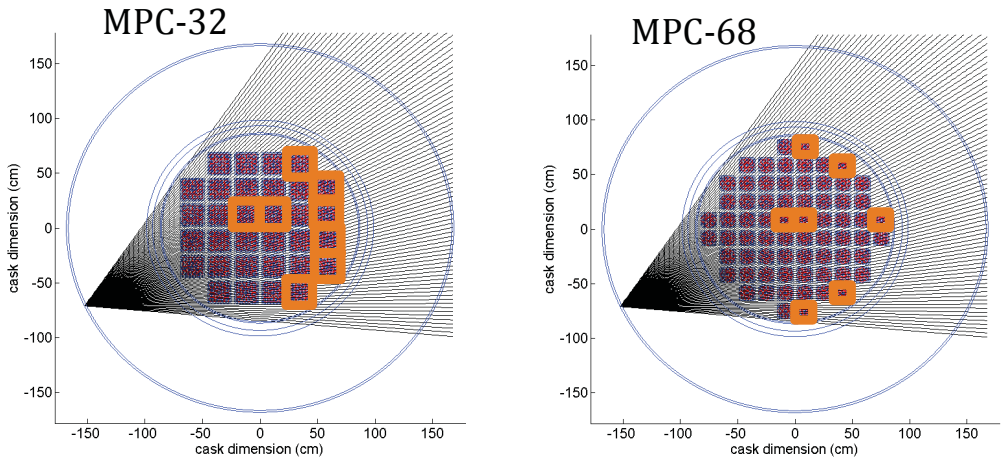

Figure 59. Geometry of transmission profile calculations for HI-STORM MCP-32 (left) and HI-STORM MCP-68 (right) casks with the source for the "fan" scan at 205 deg.

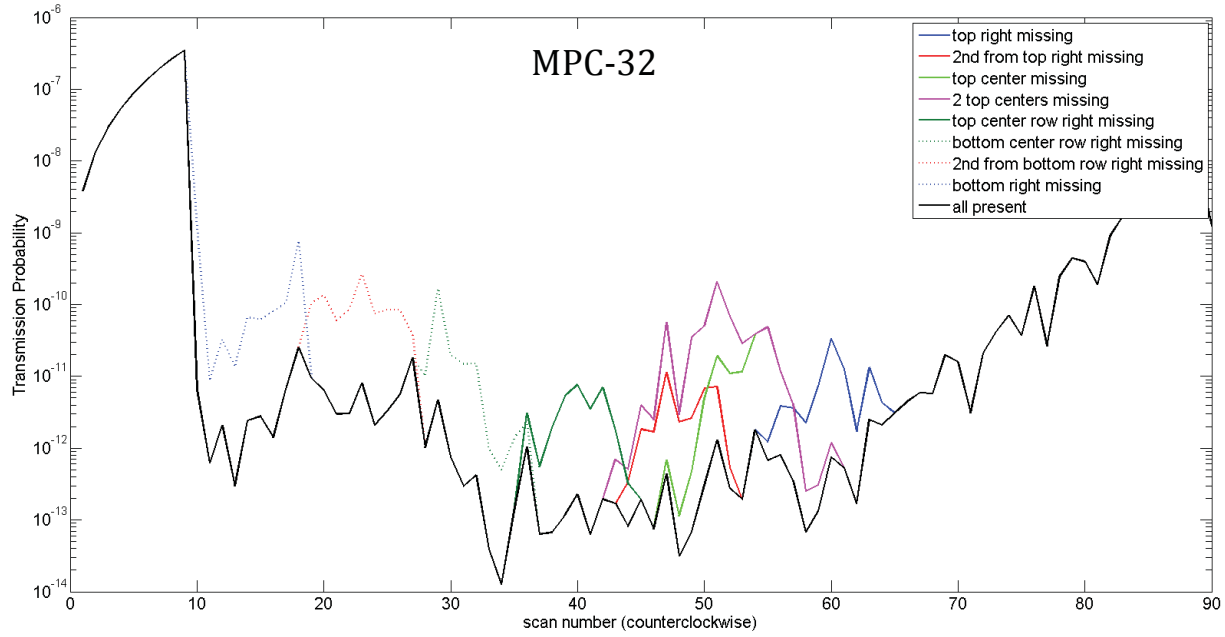

Figure 60. Transmission profiles for 205 deg. "fan" scans of a HI-STORM MPC-32 cask. The black lines show the transmission probabilities with all assemblies in place. The colored lines give the transmission values with specific assemblies removed as indicated in the legend.

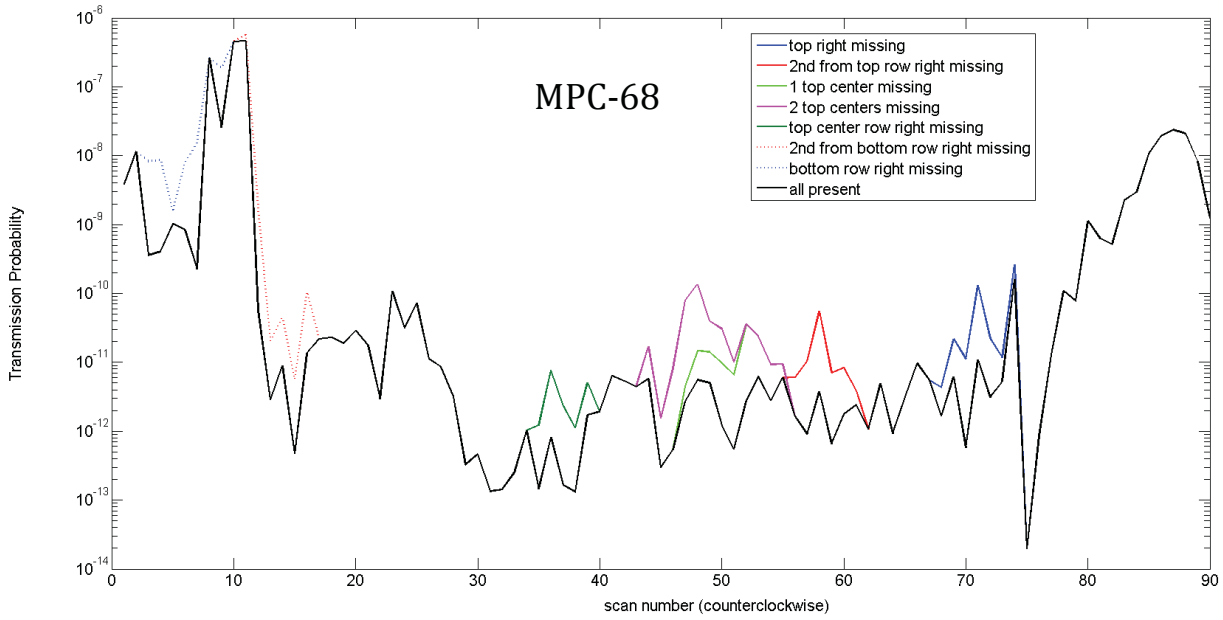

Figure 61. Transmission profiles for 205 deg. "fan" scans of a HI-STORM MPC-68 cask. The black lines show the transmission probabilities with all assemblies in place. The colored lines give the transmission values with specific assemblies removed as indicated in the legend.

The analytical results shown in the figures above were validated by MCNP radiation transport calculations for the representative "fan" scan of a HI-STORM MPC-24 cask show in Figure 62. In the MCNP calculation an 8 MeV beam with 30% energy spread and 1.75 mrad half-angle was transported through the locations shown. A flux estimating point detector was placed in the

beamline about 5 cm outside the wall of the cask. This type of detector, along with use of particle splitting and limiting the geometry of the cask to only 60 cm in height, allows for reasonable computation time for such a highly attenuating model. The reduction in cask height is justified by the very low probability that a photon would scatter far into the cask and then scatter back to the detector. Signal photons are of primary interest. For most lines through the cask the analytical values agree well with the MCNP calculated ones. Several analytical data points are slightly above the MCNP simulations, i.e., the transmission is slightly underestimated in the analytical calculation, and only for one beam is the analytical transmission probability larger than the MCNP value. For the purpose of the analysis presented here the analytical estimates are therefore sufficiently accurate.

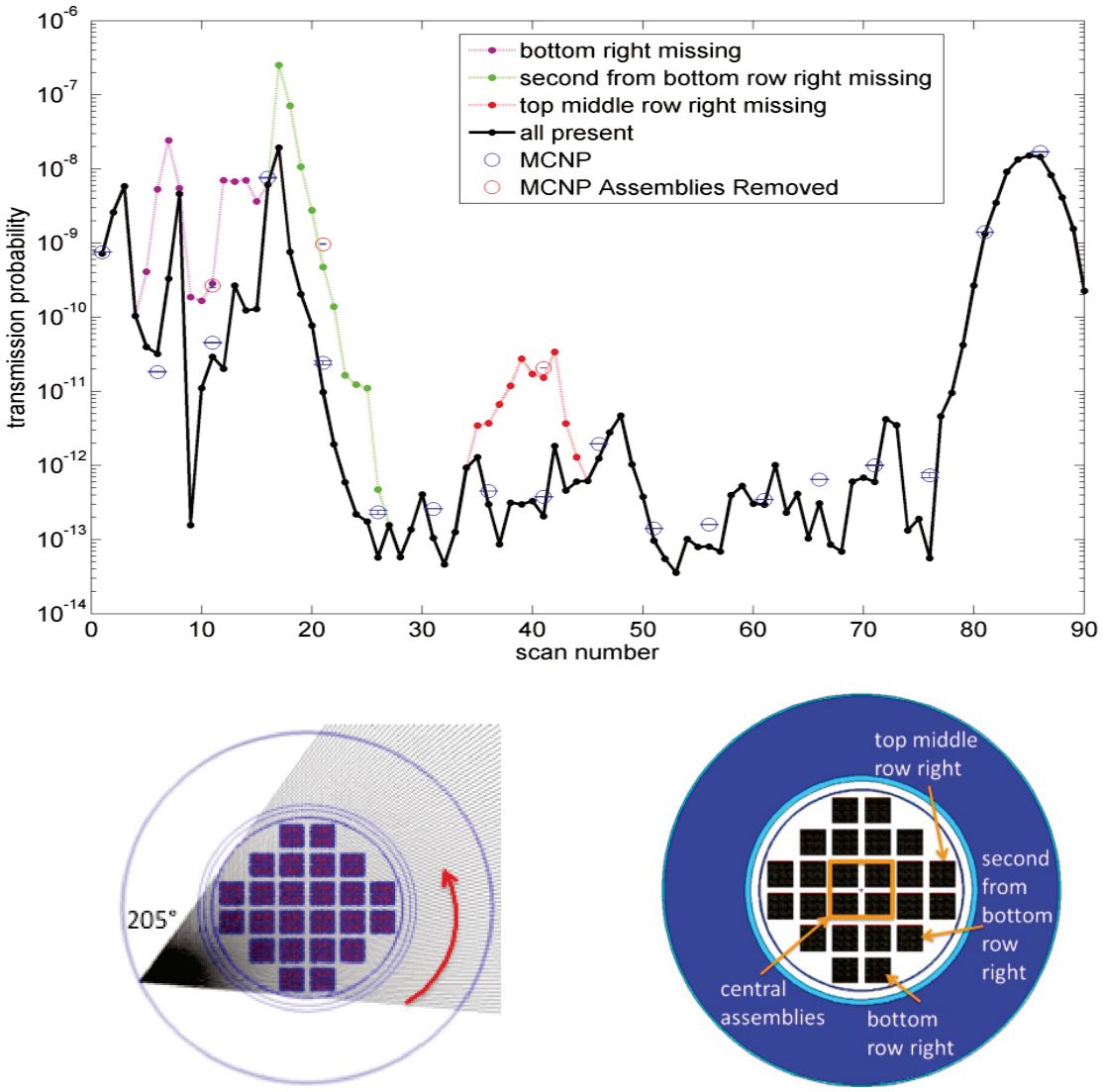

Figure 62. Validation of analytical calculations with MCNP simulations. Analytical calculations for transverse "fan" scan of a HI-STORM MPC 24 cask are shown as black (all assemblies in place) and colored data points. The MCNP results are indicated by the open blue circles (all assemblies in place) and by open red circles for beams through an unoccupied assembly location.

I.5.5 Impact on Cask Verification Application and MPS Requirements

Re-verification of a spent fuel dry-storage cask by measuring the transmission profile is a prime example of how an intense pencil beam of MeV photons can be used to penetrate very thick objects. Verification of the presence of assemblies or even single pins can be done in a straightforward way by measuring the longitudinal transmission through the cask while scanning a narrow-divergence beam across it. Such a scan could be conducted with photon beam fluxes of $1x10^{11}$ ph/s in measurement times on the order of hours even for casks with very thick lids and bottom plates.

In a transverse scan the transmission probabilities vary greatly across the cask. The transmission is lowest through the center but does not fall much below $1x10^{-12}$ for either of the two types of casks considered here when an optimized source orientation in respect to the assembly pattern is used. A missing assembly increases the transmission by roughly an order of magnitude as can be seen for the transmission profile in Figure 63. Such an increase is easily detectable and the measured transmission profile enables the determination of unoccupied assembly positions by comparison with the expected profile for a fully loaded cask. A beam flux of $5x10^{12}$ ph/s ($5x10^{8}$ ph/pulse, 10 kHz rep rate) would result in at least 1 count/s. Assuming a minimum of 100 counts per beam chord, a full cask scan consisting of 90 beam chords could be performed in an acceptable measurement time of less than three hours.

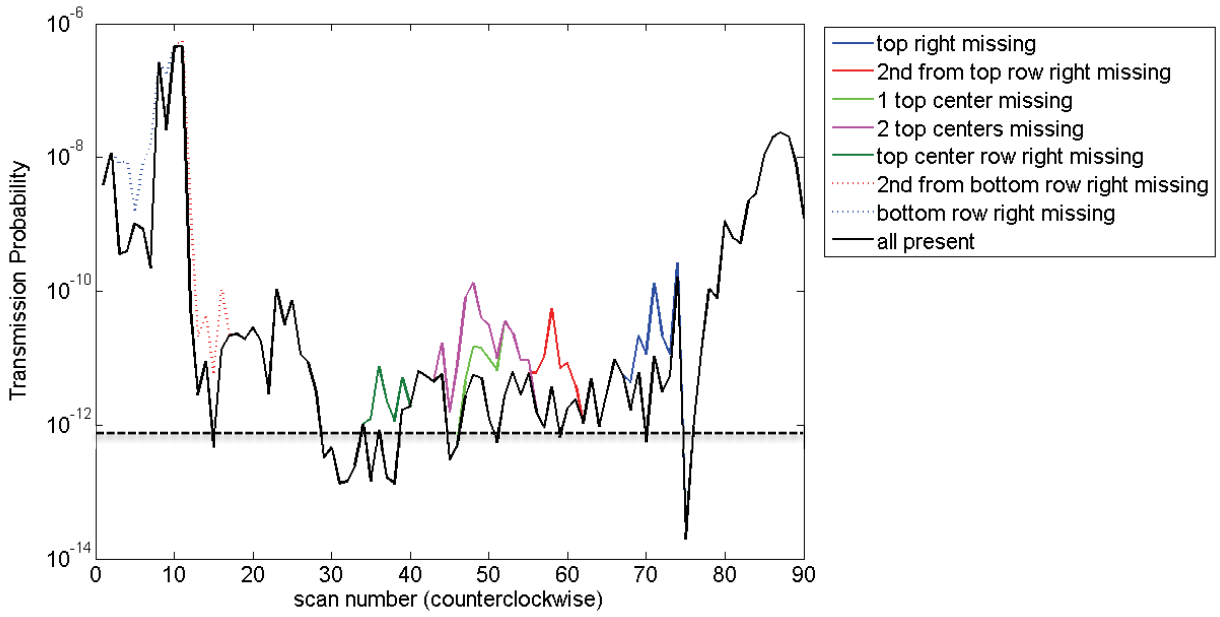

Figure 63. Analytically calculated scan with 90 beams of a HI-STORM MPC 68 cask. The black data points show the transmission probabilities for the 90 lines with all assemblies in place. The colored data points give the transmission values with specific assemblies removed as indicated in the legend. The lines connect the data points. The source position is at 205 degree.

This application requires a photon source that produces an intense, low divergence photon beam in the 6 to 8 MeV energy range. A fairly large energy spread (20-30% FWHM) that maximizes the number of photons/pulse is acceptable. The beam diameter should be significantly smaller than the assembly width, which suggests an angular divergence of several mrad. A lower divergence of ~2 mrad is required for resolving individual fuel pins in lengthwise measurements through the cask. For transverse transmission measurements a high yield of $>1 \cdot 10^{12}$ ph/s is required to

overcome the main challenge which is low transmission through the massive cask. The source should be pulsed with nanosecond or shorter pulse length to enable efficient detector gating for discriminating against the passive background from the spent fuel in the cask. These requirements could be met by a Thomson source operating at >10 kHz and $5 \cdot 10^8$ ph/shot. Importantly, the MPS needs to be transportable and sufficiently compact to be set up next to a dry-storage cask and to be moved as needed.

The dry-storage cask verification capability provided by a Thomson source with the above characteristics could fill a gap, as currently no satisfying method for verifying assembly occupancy exists. Two potential alternative techniques are being explored. The ability of the Compton Dry-Cask Imaging Scanner (CDCIS) [43] developed at INL to detect empty vs. full storage positions was demonstrated for a Westinghouse MC-10 cask. However, the scanner was not able to distinguish empty vs. full positions for casks in Doel (Belgium), which was likely due to the presence of a thick steel shield over the lid of the cask that introduced too much scattering. Preliminary results from first tests of a cosmic-ray muon imaging system [44] that is currently under development have indicated that missing fuel bundles can be detected after 100 hours of exposure. It is not yet clear how much the performance of that system can be improved, and capabilities will need to be compared as both systems develop. Furthermore, scanning a cask from a few different directions (multiple views) using a photon source may allow additional evaluation of loading structure and material distribution inside the cask which may provide advantages over other methods.

III. Summary of Applications Impact and MPS Requirements

Simulations have been presented that evaluate MPS benefit and parameter requirements for a set of nonproliferation and related applications identified and prioritized through discussions with laboratory subject matter experts, DNN R&D, and its stakeholders. The applications analyzed were: screening, detection, warhead verification, and nuclear fuel cask scanning. The simulations reported herein are summarized for each application area in the Executive Summary and are cumulative to the preliminary analysis reported in [1]. A separate final report combines this report with the previous report and includes the broader initial assessment and also a high-level sequence for the potential MPS development path, including application performance verification measurements. The simulations detail the performance achievable for each application and the required MPS parameters including source tradeoffs and constraints (e.g. bandwidth, intensity, pulse structure, beam angular spread). Simulations focused on the conventional signatures of radiography, photofission, and NRF to enable comparison with present methods and evaluation of benefit. Full system performance was considered to evaluate the impact that monoenergetic sources would have. This included natural and induced background radiation, beam propagation to a target, penetration, signature generation and detection, penetration limits, and radiation dose to target and operators.

Significant potential benefit was indicated for each prioritized application. Common source requirements include production of monoenergetic photon beams at energies ranging from 1.5-15 MeV, and with typical fluxes in the range of 10^{10} photons per second for initial capabilities to 10^{12} photons per second for high performance applications. Pulsed sources should have repetition rates in the kHz range to enable initial capabilities (corresponding to 10^{7} to 10^{8} photons per shot), while repetition rates in the 20-50kHz range would enable high performance. Replacing bremsstrahlung with a monoenergetic source having similar emission angle and pulse structure enables reductions in radiography dose by factors of 3-4x due to the narrow energy spread alone, for the configurations evaluated. Photofission dose is also reduced, with the reduction depending on the energy used: ~4x at 14 MeV where photofission is peaked, but more than 50x for energies used in cargo screening (i.e., <10 MeV). Radiography and photofission require only modest energy spread at the 20% level. In some photofission cases where gross number of fissions is a higher priority than dose reduction (i.e. single sided detection), even larger energy spreads may be desirable if that increases MPS flux (as is the case for Thomson sources). Exploiting NRF signatures strongly motivates MPSs with energy spreads at or below 2%, with detection times and doses improving rapidly for lower energy spreads. Dose reduction compared to a bremsstrahlung source for NRF can exceed two orders of magnitude. Radiography and photofission will be possible before NRF applications, because the later require finer control of the MPS. Use of multiple energies allows Z-discrimination in radiography, energy-resolved photofission, and NRF measurements. Application advantages are available from both pulsed beams (e.g. prompt neutron signatures) and continuous beams (e.g. easier use of counting detectors).

For many applications, intense narrowly collimated photon beams of controllable energy are a key MPS parameter. In many cases the benefits from narrow-angle emission equal or outweigh those from monoenergetic beams alone. In radiography a narrow-angle beam scanned across the target mitigates scattering contributions to image degradation. This effect was found to be dominant over control of photon spectrum in mitigating scattering, indicating that MPSs with narrower angle emission cones than bremsstrahlung sources will provide strongest advantage (and correspondingly, that MPSs with broader emission angles than bremsstrahlung systems may not be advantageous where scattering is significant). Scanning also enables flux to be adapted to local attenuation at each pixel. The dose reduction obtained depends sensitively on object structure. However, realistic structures often have severe scattering and have small objects with high

attenuation surrounded by large low-density areas. In many such cases, a scanned pencil beam can save between factors of a few and a hundred-fold in dose relative to conventional fan beams while also improving contrast. While a pencil beam would be very intense if held stationary on one position, its use reduces the number of photons required to extract signal from each area of the target, hence reducing dose required. Adapting flux as such a beam is scanned across a target can allow extraction of signal using the physics-limited minimum of dose (typically much less than used in a conventional fan beam). Similarly, for photofission and NRF interrogation, in all application areas, use of a beam whose opening angle matches the object of interest improves signal per unit dose dramatically and in many cases is required to obtain a signal. For applications considered, appropriate beam opening angles are in the few mrad range. Use of such narrow angle beams requires that suitable rastering systems be developed once MPS technologies are sufficiently mature.

Additional applications were identified which were addressed to the extent practical by leveraging overlap with the main topics. In particular, emergency response capabilities are indicated by the cargo, treaty and stockpile stewardship sections. The results indicate that a MPS could provide important capabilities for lower-dose radiography, for very high-resolution radiography to identify components (with potential resolution as fine as micron-scale), and for secondary identification of material using NRF or photofission. As identified above, any monoenergetic source can reduce radiography dose by a factor of a few and can increase Z contrast (e.g. nuclear reaction sources). Realizing further dose reduction as well as high resolution and secondary identification prioritizes MPSs with adjustable energy, with narrow-angle beams and with small emission spot size (e.g. Thomson sources). Repetition rate and flux could be relaxed relative to cargo applications due to lesser need for throughput. Small MPS size is a priority, which may make this a later application to be addressed. However, vehicle-mobile instruments have been mentioned in which case a near-term capability is realistic. Similarly, the potential of MPSs with small photon emission spot size (e.g. Thomson sources) for high-resolution radiography with reduced dose indicates strong potential impact on medical imaging, and industrial nondestructive analysis. Detailed analysis was not within scope for photonuclear data, spent fuel assembly assay, materials characterization in accident scenarios, waste drum content, fuel quality control, or pyroprocessing monitoring. These are possible topics for future work.

Photon source requirements appear to be within range of realistic MPS candidates. Two candidate technologies are under development: sources based on Thomson (also known as Compton or inverse Compton) scattering of a laser from a high energy (GeV-class) electron beam, and sources based on nuclear reactions induced in a target by a modest energy (MeV-class) ion beam. The Final Report of this project includes an assessment of the development requirements for MPS technologies to meet application needs.

In summary, simulations showed that MPSs can offer significant benefit to cargo screening, detection, warhead verification, and nuclear fuel cask scanning. They indicate that these benefits are also likely to impact emergency response and many other application areas both within and outside nonproliferation work. Full benefit is realized with an MPS having adjustable energy in the 1.5-15 MeV range, narrow (mrad) emission angle, energy spreads from 20% for radiography and photofission down to <2% for NRF, and with photon fluxes of 10^{10}-10^{12} photons/second delivered to the target. These parameters match with the development outlook for Thomson/Compton based photon sources, provided that such systems can be made sufficiently compact and can operate at the required repetition rates (≥kHz). New signatures enabled by such sources may offer additional benefit.

References

[1] C. Geddes, B. Ludewigt, J. Valentine, M.-A. Desalle, G. Warren, M. Kinlaw*, et al.*, "Impact of Monoenergetic Photon Sources on Nonproliferation Applications: Initial Assessment and Prioritization Report," Idaho National Laboratory, Idaho Falls, Idaho INL/LTD-15-35872, 2015.

[2] R. Richardson, H. Martz, S. Korbly, W. Ledoux, W. Bertozzi, private communication.

[3] http://physics.nist.gov/PhysRefData/Xcom/html/xcom1.html

[4] Martz H. et al., Radiography techniques to detect shielded SNM overview, presentation SORMA West (2016).

[5] S. Korbly, R. Richardson, private communications.

[6] R. Richardson, private communication.

[7] O'Day B. et al. 'Initial results from a multiple monoenergetic gamma radiography system for nuclear security' NIMA (2016) 832, 68–76 dx.doi.org/10.1016/j.nima.2016.05.117

[9] Aufderheide M. et al., HADES a code for simulating a variety of radiographic techniques, UCRL-PROC-207617. DOI: 10.1109/NSSMIC.2004.1462780.

[10] www.passportsystems.com

[11] J. Pruet, D. P. McNabb, C. A. Hagmann, F. V. Hartemann, and C. P. J. Barty, "Detecting clandestine material with nuclear resonance fluorescence," Journal Of Applied Physics 99, 123102 (2006).

[12] W. Bertozzi, J.A. Caggiano, W.K. Hensley, MS Johnson, SE Korbly, RJ Ledoux, DP McNabb, EB Norman, WH Park and GA Warren, Nuclear Resonance Fluorescence Excitations Near 2 MeV in 235U and 239Pu, Phys. Rev. C 78, 041601-5 (2008).

[13] E. Kwan et al., Discrete deexitations in 235U below 3 MeV from nuclear resonance fluorescence, Phys. Rev. C 83, 041601 (2011).

[14] B. J. Quiter, T. Laplace, and B. A. Ludewigt, "Examining Pu-239 and Pu-240 Nuclear Resonance Measurements on Spent Fuel for Nuclear Safeguards," in Proc. of the Annual Meeting of the Institute for Nuclear Material Management, Orlanda, Florida, 2012.

[15] M.S. Johnson, et al., Searching for illicit materials using nuclear resonance fluorescence stimulated by narrow-band photon sources, Nuclear Instruments and Methods in Physics Research Section B: Beam Interactions with Materials and Atoms, Volume 285, 15 August 2012, Pages 72-85.

[16] Currie, L. A., Limits for qualitative detection and quantitative determination. Application to radiochemistry, Analytical Chemistry 40 (1968).

[17] Cardenas, E. S., et al., Comparison of fission signatures from β^- delayed -ray and neutron emissions, Nuclear Instruments and Methods A **792** (2015).

[18] Reedy, E. T. E., et al., The detection of delayed -rays between intense bremsstrahlung pulses for discriminating fissionable from non-fissionable materials, Nuclear Instruments and Methods A **606** (2009).

[19] Slaughter, D. R., et al., Preliminary results utilizing high-energy fission product -rays to detect fissionable material in cargo, Nuclear Instruments and Methods B **241** (2005).

[20] Thompson, S. J., et al., Utilization of high-energy neutrons for the detection of fissionable materials, Applied Physics Letters **90** (2007).

[21] Mihalczo, J. T., et al., Subcriticality Measurements with HEU (93.2) Metal Annular Storage Castings, Oak Ridge National Laboratory Report ORNL/TM-2007/134 (2007).

[22] S G Rykovanov1, C G R Geddes, J-L Vay, C B Schroeder, E Esarey and W P Leeman, Quasi-monoenergetic femtosecond photon sources from Thomson Scattering using laser plasma accelerators and plasma channels, Journal of Physics B: Atomic, Molecular and Optical Physics, Volume 47, Number 23.

[23] Verbeke, J. M., et al., Simulation of Neutron and Gamma Ray Emission from Fission and Photofission, Lawrence Livermore National Laboratory Report UCRL-AR-228518 (2010).

[24] R. Neibert, J. Zabriskie, C. Knight, and J. L. Jones, "Passive and Actice Radiation Measurements Capability at the INL Zero Power Physics Reactor (ZPPR) Facility," Idaho National Laboratory2010.

[25] C. A. Miller, B. Ludewigt, B. J. Quiter, S. A. Pozzi, and C. G. R. Geddes, "Assessing Impact of Monoenergetic Photon Sources on Nonproliferation Applications," in *American Nuclear Society Advances in Nuclear Nonproliferation Technology and Policy Conference*, Sante Fe, New Mexico, 2016.

[26] J. Allison, K. Amako, J. Apostolakis, H. Araujo, P. A. Dubois, M. Asai*, et al.*, "Geant4 developments and applications," *Nuclear Science, IEEE Transactions on,* vol. 53, pp. 270-278, 2006.

[27] S. Agostinelli, J. Allison, K. Amako, J. Apostolakis, H. Araujo, P. Arce*, et al.*, "GEANT4-a simulation toolkit," *Nucl Instrum Meth A,* vol. 506, pp. 250-303, Jul 2003.
[28] W. Bertozzi and R. J. Ledoux, "Nuclear resonance fluorescence imaging in non-intrusive cargo inspection," *Nuclear Instruments and Methods in Physics Research Section B: Beam Interactions with Materials and Atoms,* vol. 241, pp. 820-825, 12// 2005.
[29] W. Bertozzi, J. A. Caggiano, W. K. Hensley, M. S. Johnson, S. E. Korbly, R. J. Ledoux*, et al.*, "Nuclear resonance fluorescence excitations near 2 MeV in (235)U and (239)Pu," *Phys Rev C,* vol. 78, Oct 2008.
[30] G. A. Warren, J. Caggiano, P. Peplowski, W. Bertozzi, R. D. Hasty, A. V. Klimenko*, et al.*, "Experimental Observations of the Background in Nuclear Resonance Fluorescence," ed. Orlando, Florida, 2009.
[31] "A CAT Scanner for Nuclear Weapons Components," Science and Technology Review, pp. 12-17, July/August 2009.
[32] C. G. R. Geddes, S. Rykovanov, N. H. Matlis, S. Steinke, J. L. Vay, E. H. Esarey, et al., "Compact quasi-monoenergetic photon sources from laser-plasma accelerators for nuclear detection and characterization," Nucl Instrum Meth B, vol. 350, pp. 116-121, May 1 2015.
[33] G. F. Knoll, Radiation Detection and Measurements, 4th ed. New York: John Wiley, 2010.
[34] "American National Standard for Determination of the Imaging Performance of X-Ray and Gamma-Ray Systems for Cargo and Vehicle Security Screening," American National Standard Institute, N42.46-2008, 2008.
[35] P. C. Johns and M. Yaffe, "Scattered radiation in fan beam imaging systems," Med Phys, vol. 9, pp. 231-239, 1982.
[36] T. M. Buzug, Computed Tomography: From Photon Statistics to Modern Cone-Beam CT. Berlin, Germany: Springer-Verlag, 2008.
[37] O.W. Hermann, R.M. Westfall, "Origen-S: Scale System Module to Calculate Fuel Depletion…," ORNL/NUREG/CSD-2/V2/R6. Oak Ridge National Laboratory, Sep. 1998.
[38] D.B. Pelowitz, ed. *MCNPX Manual, Version 2.7.0.* LA-CP-11-00438. Los Alamos National Laboratory, April 2011.
[39] J. Buongiorno, "PWR Description," 22.06: Engineering of Nuclear Systems. Massachusetts Institute of Technology, 2010.
[40] E.R. Johnson, K.J. Notz, "Shipping and Storage Cask Data for Spent Nuclear Fuel," ORNL/TM-11008. Oak Ridge National Laboratory, Nov. 1988.
[41] J.A. McClure, "Estimation of the Westinghouse 17x17 MOX SNF Assembly Weight", A00000000-0 I7 17-02 IO-0000 1 REV 00, CRWMS/M&O.
[42] NIST Standard Reference Database 8 (XGAM) M.J. Berger, et. al. NIST, PML, Radiation Physics Division, 1998.
[43] Wharton, C. J., et al., Summary Report: INLCDCIS Cask Scanner Testing at Doel, Belgium, INL/EXT-13-28809, 2013.
[44] M. Durham, et al., Muon monitoring of a fuel cask at the Idaho National Laboratory, LA-UR-15-23710, 2015.